APPLYING GE/SI RATIOS TO TRACE WEATHERING REACTIONS, HYDROLOGIC PATHWAYS AND COAL FLY ASH CONTAMINATION IN WATERSHEDS ACROSS THE UNITED STATES

A Dissertation

Presented to the Faculty of the Graduate School

of Cornell University

In Partial Fulfillment of the Requirements for the Degree of

Doctor of Philosophy

by

Arnulfo A Aguirre

August 2019

APPLYING GE/SI RATIOS TO TRACE WEATHERING REACTIONS, HYDROLOGIC PATHWAYS AND COAL FLY ASH CONTAMINATION IN WATERSHEDS ACROSS THE UNITED STATES

Arnulfo A Aguirre, Ph. D.

Cornell University 2019

The generation of solutes in the critical zone (CZ), the region from the top of the canopy to groundwater, is an essential process that sustains ecosystems. The chemical and physical mechanisms that weather rock are fundamental for nutrient cycling and the generation of reactive surfaces. These processes define the evolution and function of the CZ. In the following dissertation, topics of silicate weathering and solute transport are explored in multiple landscapes. Additionally, the application of Ge/Si as a geochemical and hydrologic tracer will be demonstrated in order to understand sources of solutes in streams, hydrologic pathways and as a tool to fingerprint coal ash contamination. Concentration-discharge (C-Q) patterns in streams are governed by solute generation mechanisms and transport processes. In the Kings River Experimental Watershed of California, we explored how C-Q relationships varied between two watersheds on a climate sequence. Using the Ge/Si, we observed that the mid-elevation catchment of Providence Creek was dominated by groundwater inputs even during periods of increased discharge resulting in chemostatic Si-Q relationships. In the higher elevation catchment of Bull Creek, significant leaching conditions due to snowmelt runoff resulted in dilution of Si-Q relationships. The sources of silicon to streams was further

investigated in the Gordon Gulch catchment of Boulder Creek, CO. In this upper montane landscape with chemostatic Si-Q patterns, colloidal transport is a major contributor to the Si flux. By analyzing bulk chemistry and Ge/Si of a colloidal suspension, we identified periods of active colloidal mobilization during high stream discharge. Since average stream Ge/Si has a narrow range of 0.4-0.5 μmol mol^{-1}, the potential of Ge/Si as a tracer for coal ash was explored during the Dan River coal ash spill of 2014. By monitoring Ge/Si and Sb levels 10-months after the spill, hotspots of elevated ratios and Sb were identified as a result of post depositional processes of coal ash. Lastly, Ge/Si was applied to understand hydrologic pathways in the Bisley 1 catchment of the Luquillo Critical Zone Observatory. Our results describe a three end-member mixing system dominated by groundwater and followed by saprolite hydrologic pathways.

BIOGRAPHICAL SKETCH

Arnulfo Andrés Aguirre was born in Monterrey, Mexico in May 31st, 1989. At the age of 10, his family relocated to Houston, Texas in 1999. He began his undergraduate degree in environmental science in August 2008 at Texas State University-San Marcos. A Bachelor of Science in Geography-Environmental studies with a minor in chemistry was completed with honors in 2012. After finishing the undergraduate degree, an opportunity arose to participate in a geothermal database management project with the Cornell Energy Institute led by Professor Jefferson Tester. This experience was very influential in the pursuit of a geology PhD program at Cornell University. After completion of the project in December of 2012, Andrés returned to Houston to complete graduate school applications and to start a new opportunity in elementary education for the spring semester. The PhD program began in August of 2013 with support from the Colman Fellowship awarded by Diversity Programs in Engineering. Additionally, a traineeship began the following year in the Cross-scale Biogeochemistry and Climate Integrative Graduate Education and Research Traineeship (IGERT) program. Throughout graduate school, Andrés became involved in leadership positions such as president of Snee Graduate Organization and co-president of Enviro-Mentors. Additionally, teaching assistantships were conducted for the mineralogy and environmental physics courses in EAS. In August 2019, Andrés will begin a career in natural resource damage assessment at IEc Inc. in Cambridge, MA.

To Mom and Dad

ACKNOWLEDGMENTS

I would like to thank first and foremost my principal advisor Dr. Louis Derry for all of the support and patience throughout these six years. Additionally, thank you to my minor committee members Dr. Bill White and Dr. M. Todd Walter for their help throughout the PhD program and being excellent teachers in geochemistry and hydrology. I owe a lot to the members of the Derry lab that welcomed me during my first year in the graduate program and taught me so much about the responsibilities of working in a research lab. Special thanks to Gregg McElwee who showed me the ropes with germanium analysis and sample preparation. Most of my PhD project has relied on analyzing samples that other people collected. This would seem like a major challenge, yet I am so thankful to have worked with scientists who always offered to share samples and data with me. Special thanks to Cliff Riebe, Suzanne Anderson, T. Joe Mills, Madeline Schreiber, Jon Chorover and Andy Kurtz for collaborating with me on so many interesting projects. Lastly, I would like to thank my Mom, Dad, Andrea, Victor and Anita for always supporting me.

TABLE OF CONTENTS

LIST OF FIGURES

LIST OF TABLES

LIST OF ABBREVIATIONS

(CZ) Critical zone

(CZO) Critical Zone Observatory

(C-Q) Concentration-discharge

(LOI) Loss on ignition

(MCL) Maximum contaminant level

LIST OF SYMBOLS

(μM) micro molar

(pmol mol^{-1}) pico-moles per mole

(μmol mol^{-1}) micro-moles per mole

(μg L^{-1}) micro-grams per liter

(m) meter

(cm) centimeter

(mm) millimeter

PREFACE

The weathering of silicate minerals in the surface of the Earth is a fundamental process of pedogenesis that generates solutes that are essential nutrients for ecosystems. By generating alkalinity, solutes like Ca^{2+} are transported by rivers into the oceans forming carbonates that are subsequently deposited on the ocean floor. Thus, sequestering atmospheric CO_2 and regulating climate. Planetary processes like climate change and tectonic uplift have been linked to changes in the marine Ge/Si_{opal} record. Marine diatoms incorporate Si and Ge in the same proportion without fractionation of Ge/Si ratios. Weathering intensity is strongly coupled to these planetary processes. Therefore, Ge/Si ratios have been used as paleo-recorders of past weathering environments. Germanium is a trace element in the crust with an average concentration of 1.4 mg kg^{-1}. Both Ge and Si are group 14 elements on the periodic table sharing similar chemical behavior and bond lengths permitting Ge to readily substitute for Si in the tetrahedral sites of silicate minerals. Germanium substitution for Si is dependent on the linkages of crystallographic structures and the degree of polymerization of Si tetrahedrons. Framework silicates like quartz and feldspars have the least substitution with Ge/Si ratios ranging between 0.5 to 2.1 μmol mol^{-1}. Incongruent weathering of feldspars will fractionate Ge/Si ratios with the precipitation of secondary aluminosilicates. Germanium is preferentially incorporated into secondary phyllosilicates, leaving solutes depleted in Ge. Therefore, secondary minerals formed during weathering will have higher Ge/Si ratios ranging between 4.8 to 6.1 μmol mol^{-1}. Congruent dissolution of secondary minerals will not lead to further Ge/Si fractionation

and solute ratios will reflect the elevated Ge/Si signature of secondary minerals. Consequently, stream Ge/Si displays an integration of congruent to incongruent weathering reactions.

In the following dissertation, the Ge/Si tracer will be applied to understand contemporary weathering and hydrologic processes. A major focus of this work will be to understand the sources of silicon to streams and to obtain a greater understanding of hydrologic flow paths and fluid residence times (Chapters 1,2 and 4). The chosen field sites for this research are small headwater catchments in protected areas where anthropogenic perturbations are minimal or have occurred decades ago. This gives us the ability to understand how natural systems generate and transport silicon and other solutes.

The natural weathering Ge/Si signal can be affected by other processes in unique settings. Systems with hydrothermal activity can have elevated Ge/Si ratios as a result of the precipitation of quartz in hydrothermal waters. Additionally, weathering of sulfide ore deposits can lead to elevated Ge/Si ratios because Ge is a chalcophile element that can be enriched in pyrite and sphalerite. Coals can also have elevated Ge concentrations as a result of organo-metallic associations during coal bed formation. Consequently, coal fly ash is another major source of Ge into river systems impacted by coal burning industries. The narrow range in stream water Ge/Si from natural weathering processes (generally 0.5 to 1.4 $\mu mol\ mol^{-1}$), provides a unique opportunity to apply this tracer as a fingerprint tool for coal fly ash contamination (Chapter 3).

The following applications of Ge/Si can highlight the unique information that can be extracted from this tool. Additionally, the compilation of analytical techniques

and innovation of those techniques can serve future researchers to apply this knowledge to un-explored settings.

CHAPTER ONE:
SEASONAL PATTERNS IN SURFACE WATER CHEMISTRY AND GE/SI DYNAMICS IN THE KINGS RIVER EXPERIMENTAL WATERSHED

Abstract

Understanding the weathering processes that generate dissolved solutes can provide important insights into concentration-discharge (C-Q) mechanisms. Ge/Si ratios were applied in this study to compare weathering processes and transport mechanisms in two catchments of California. The Kings River Experimental Watershed is located in the Sierra Nevada mountains in central California. The site is a climate sequence with Providence Creek at 1479-2113 m and Bull Creek at 2055-2490 m. Both sites share similar bedrock composition, vegetation cover and mean annual precipitation. Due to the climate gradient, Providence Creek receives a mixture of rain and snow while Bull Creek receives mostly snow. Additionally, Pleistocene glaciation has resulted in less developed soils in Bull than Providence Creek. This slight temperature variation, precipitation distribution and geologic history has had significant effects on long-term critical zone evolution. Providence Creek Si-Q relationships are near constant with varying discharge (power law exponent of -0.08 to -0.12). This C-Q pattern will be referred to as chemostatic. Ge/Si ratios in Providence Creek ranged between 0.03-0.12 pmol μmol^{-1} for water year 2009. The Ge/Si signature suggests one of the most weathering limited regimes with near complete Ge partitioning into secondary minerals. We interpret this to reflect long fluid residence times and significant groundwater contribution to stream flow. In the snow dominated catchment of Bull Creek, Si-Q

relationships are closer to perfect dilution (power law exponent of -0.16 to -0.46) and have higher Ge/Si ratios during increased discharge (0.1 to 0.9 pmol μmol^{-1}). The greater leaching from dilute infiltrating snowmelt and shorter fluid residence time has resulted in unsaturated conditions for Si that promote secondary mineral weathering. This has resulted in drastically different Si dynamics from a catchment just a few hundred meters above Providence Creek. Our study demonstrates the variability in C-Q behavior from sites with slight elevation differences. This shows that precipitation distribution and geologic history are significant variables that can dramatically affect critical zone evolution.

1.1 Introduction

The generation of solutes by chemical weathering and the hydrologic transport of those solutes are integral mechanisms of concentration-discharge relationships (C-Q). Godsey et al. (2009) described how most catchments throughout the U.S. have near-constant concentrations of weathering solutes with increasing discharge. This behavior was termed chemostatic. On the other hand, systems where a constant source of solutes are diluted by higher discharge would be characterized as displaying perfect dilution behavior. These observations have led to many questions regarding the dominant mechanisms that give C-Q patterns their chemostatic to dilution character. Concentration-discharge patterns can be described using a power law function of the form;

$$C = aQ^b \quad (1)$$

where C is solute concentration, a is the y-intercept, Q is discharge and b is the exponent

of the relationship. The exponent has a physical interpretation in which a range between 0 and -0.2 indicates chemostasis (Herndon et al., 2015). The perfect dilution case would have a power law exponent of -1. Solutes like Al, Fe and DOC are characterized with flushing behavior or colloidal mobilization that result in positive power law exponents (Hunsaker and Johnson, 2017; Trostle et al., 2016). Chemostatic behavior has been interpreted to result from significant contribution from pre-event water like groundwater (Clow and Mast, 2010). Most importantly, conditions must allow weathering not to be limited by rates of weathering reactions, mineral surface area and short fluid residence times (Maher, 2011). For catchments with dilution behavior, short fluid residence times and an increased contribution from dilute event water have been shown to be significant in these situations (Shanley et al., 2011; Torres et al., 2015). Tools like end-member mixing analysis (EMMA) have been applied to describe fractional mixing patterns from multiple water reservoirs (Liu et al., 2017). EMMA is powerful tool to identify, 1) number of end-members in a system, 2) mixing proportions of end-members that can combine to yield stream water chemistry (Hooper, 2003). Silicon in most landscapes behaves conservatively when derived primarily from mineral weathering. Silicon concentrations alone or coupled with $\delta^{18}O$ as a tracer pair have been applied in end-member mixing studies to understand these hydrologic processes (Hooper and Shoemaker, 1986). One of the underlying limitations of EMMA is the assumption of constant concentrations for the selected end-members and the disregard for the chemical reactions that are giving end-members their chemistry. This missing information can be instrumental in understanding the mineralogical environment encountered through a hydrologic pathway.

In the following study, we present an application of Ge/Si as a geochemical and hydrologic tracer to understand the sources of silicon to streams in the Providence and Bull Creek catchments of the Kings River Experimental Watershed (KREW) of California. Our objective is to apply Ge/Si in the context of C-Q relationships. We seek to understand how Ge/Si ratios in stream water can help constrain weathering mechanisms, transport processes and fluid residence times. Exploration of these mechanisms is important for the understanding of the architecture and function of the critical zone (CZ). C-Q patterns are an integration of water partitioning processes, geochemical reactions and transport mechanisms that have implications on the sustainability of ecosystems in the CZ.

1.2 Site Description

The Kings River Experimental Watershed consist of eight sub-catchments that are within the Sierra National forest located approximately 40 miles northeast of Fresno, CA (Figure 1.1). Providence Creek is a mid-elevation watershed ranging between 1479 and 2113 m and is co-located with the Southern Sierra Critical Zone Observatory (SSCZO) (Table 1.1).

Table 1.1: Kings River Experimental Watershed Catchment Characteristics

Sub-catchment	Area (km^2)	Elevation (m)		Mean Slope Percent Rise
		Minimum	Maximum	
Providence Creek				
P301	0.99	1803	2113	19.9
P303	1.32	1727	2017	22.9
P304	0.49	1755	1979	23.0
D102	1.21	1479	1981	32.8
Bull Creek				
B201	0.53	2150	2382	21.3
B203	1.38	2195	2488	20.2
B204	1.67	2192	2490	19.8
T003	2.28	2055	2465	26.7

Data obtained from Liu et al. (2013).

Providence Creek is within the rain-snow transition at 2000 m where snow can make up between 35 and 60% of precipitation (Bales et al., 2018; Hunsaker and Johnson, 2017). Bull Creek is the upper-elevation paired watershed ranging between 2055 and 2382 m; elevations receiving up to 90% precipitation as snow (Johnson et al., 2011). The climate is montane Mediterranean with cool wet winters and dry summers that last from May through October. The water balance in the Sierra Nevada is strongly affected by precipitation patterns. Nearly 90% percent of precipitation occurs between October and April as a mix of rain and snow depending on elevation (Safeeq and Hunsaker, 2016) (Figure 1.2a). Summers are very dry with sporadic precipitation events. In the summertime during the peak growing season, evapotranspiration has a strong effect on stream discharge (Bales et al., 2011; Hunsaker et al., 2012). As indicated by the proportion of stream discharge to precipitation (runoff ratio), discharge in all KREW catchments lag behind evapotranspiration (Safeeq and Hunsaker, 2016).

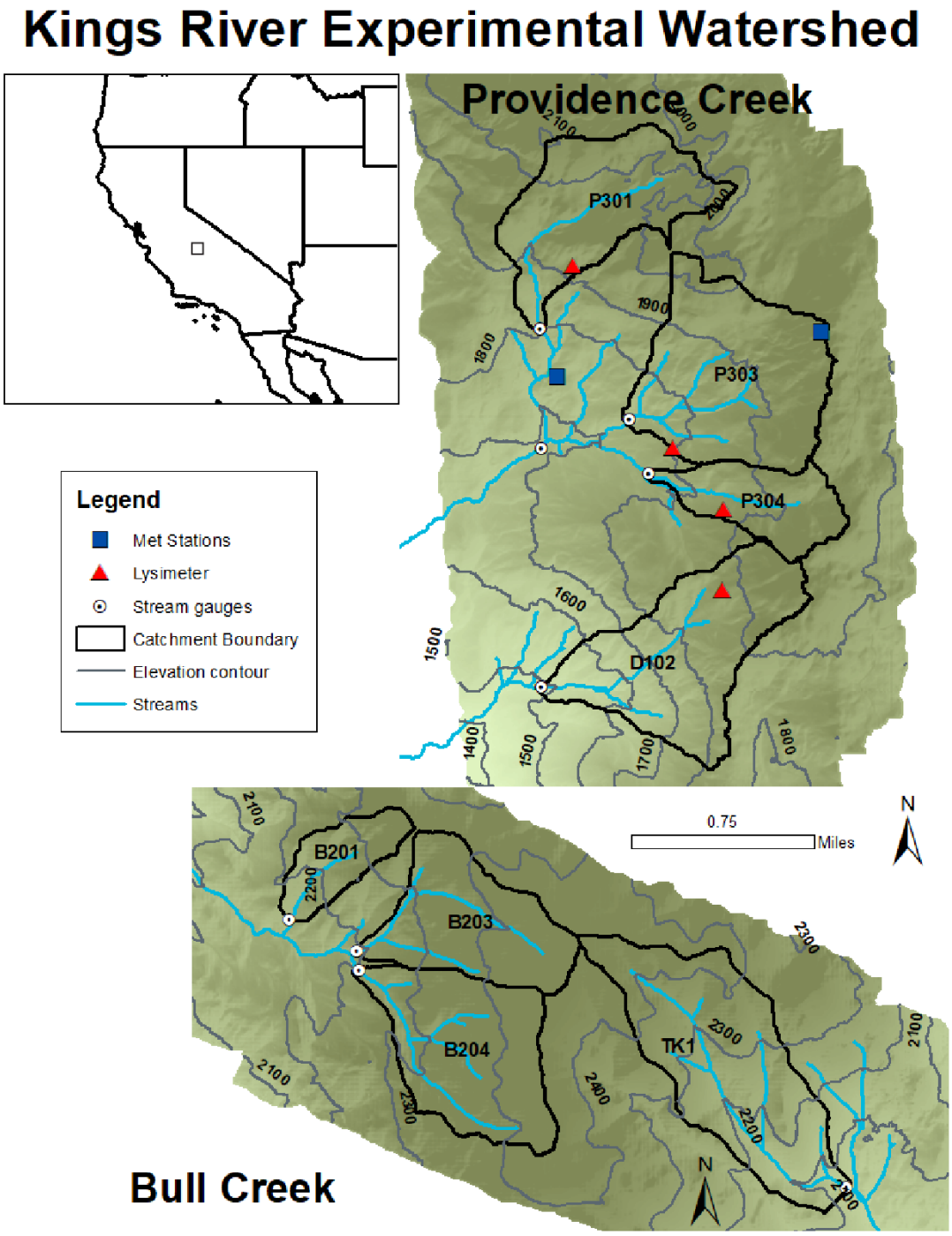

Figure 1.1: Map of the Kings River Experimental Watershed. Catchment boundaries for the Providence and Bull Creek sub-catchments.

Our study was conducted during water year 2009 (WY2009) with annual precipitation

of 1074 to 1207 mm yr^{-1} and temperature between 3.0 and 19 ^{o}C (Safeeq and Hunsaker, 2016). The snowpack developed from the first snow event on December 13th, 2008 until maximum snow depth on February 17th, 2009 (Figure 1.2a). During this time, stream discharge was low and likely sustained by groundwater (Figure 1.2b and 1.2c). However, there are some discharge pulses during the snow accumulation period. All KREW sub-catchments experienced a sharp discharge pulse on January 24th, 2009 (Figure 1.2b and 1.2c). Since the snowpack developed before this precipitation event, the sharp pulse in January may be from snowmelt runoff caused by rainfall on the snowpack. Besides the January 24th precipitation event, discharge increased during the snowmelt period except for D102 (Figure 1.2b). Instead, the falling limb of D102 corresponds to the snowmelt period. This catchment has the lowest mean elevation (1754 m) and the highest mean slope (33%) among the KREW watersheds (Table 1.1) (Liu et al., 2013). Therefore, precipitation at D102 is mostly rain and the higher relief can result in a greater hydraulic gradient leading to shorter water residence times (Tetzlaff et al., 2009). Moreover, baseflow was higher in P304 than at any other catchment in KREW (Figure 1.2b). This different hydrologic behavior has been attributed to a greater groundwater storage reflected by a higher runoff ratio (Safeeq and Hunsaker, 2016).

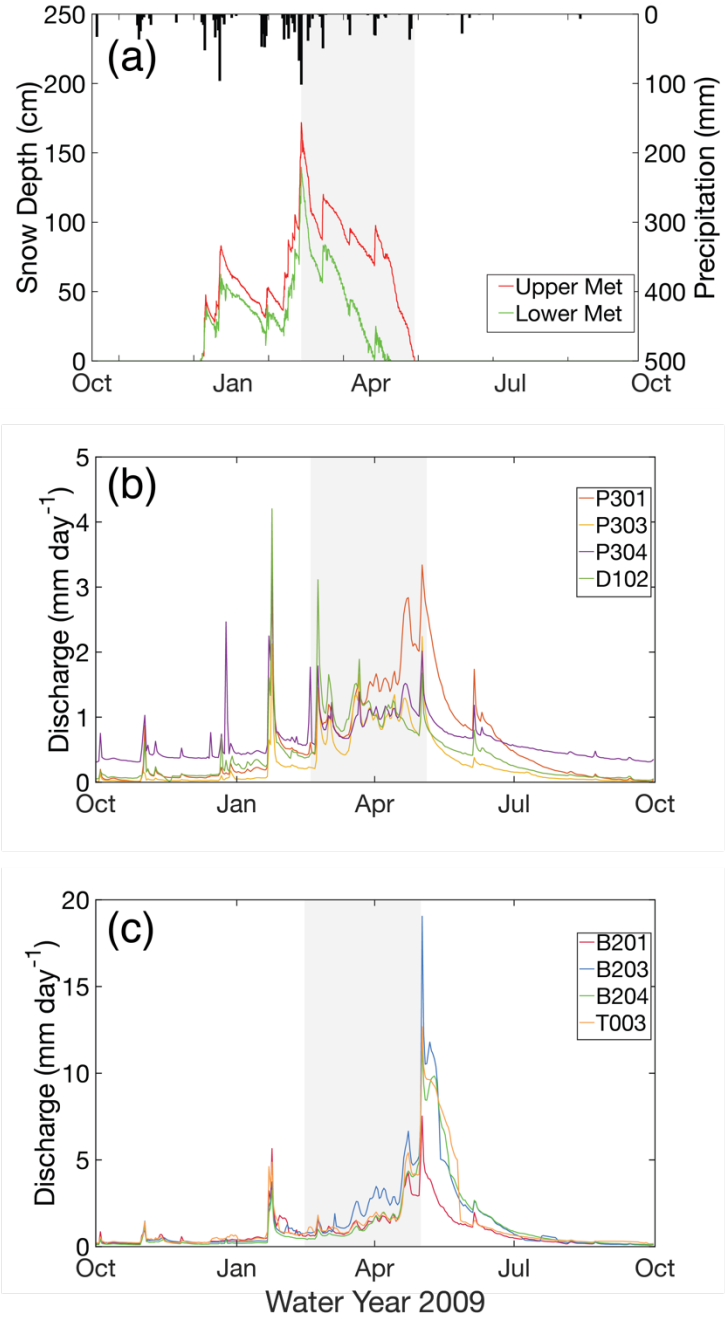

Figure 1.2: KREW precipitation, snow depth and discharge. (a) precipitation and snow depth for WY2009 in upper (1950 m) and lower (1730 m) meteorological stations. (b) and (c) are discharge for Providence and Bull Creek respectively. The grey bar represents the snowmelt period.

The higher elevation catchments of Bull Creek display a more gradual increase in discharge during the snowmelt period (Figure 1.2c). On January 24th, 2009, we can also observe the hydrograph pulse seen in the Providence catchments. The magnitude of the hydrograph pulse during WY2009 reached discharge levels greater than those observed in Providence Creek (4.0-6.0 mm day^{-1}). For example, B203 peak discharge was 19 mm day^{-1} on May 2nd, 2009. Discharge at Bull Creek is greater than Providence Creek despite similar annual precipitation. This is consistent with observations that streamflow increases with elevation as a result of lower sublimation and evapotranspiration (Safeeq and Hunsaker, 2016). It can be observed that Bull Creek experiences fewer and lower magnitude pulses throughout WY2009. Since Bull Creek is above the 2000 m threshold receiving mostly snow, discharge is strongly dependent on snowmelt. Consequently, every sub-catchment in Bull Creek has peak discharge after snowpack depletion.

Land cover is dominated by mature mixed-conifer forests with some areas of exposed bedrock and meadows (Bales et al., 2018). The forest consists of white fir (*Abies concolor*), sugar pine (*Pinus lambertiana*), ponderosa pine (*Pinus ponderosa*) and California Black Oak (*Quercus kelloggii*) (Dolanc and Hunsaker, 2017). Vegetation at Providence Creek is largely Sierran mixed-conifer forest with some chaparral. In Bull Creek, vegetation is mostly Sierran mixed-conifer forest and red fir (*Abies magnifica*) (Hunsaker et al., 2012).

Bedrock at KREW is granitic and characterized as Dinkey Creek granodiorite and Bald Mountain leucogranite (Bateman, 1992).

Table 1.2: KREW bedrock chemistry and Ge/Si composition

Bulk Chemistry						
	SiO_2	**Al_2O_3**	**MgO**	**CaO**	**Na_2O**	**Ge/Si[a]**
			wt. %			**pmol μmol^{-1}**
Dinkey Creek granodiorite	59.3	17.3	3.3	6.2	3.1	1.9

Hahm et al. (2014)

[a]Germanium analyzed using x-ray fluorescence (XRF). The Ge measurement uncertainty may be 20-30%.

Table 1.3: KREW bedrock mineralogy

Mineralogy						
	Quartz	**K-feldspar**	**Plagioclase**	**Biotite**	**Hornblende**	**Mafics undivided**
				vol. %		
Dinkey Creek granodiorite	22.5	10	48.7	-	-	19.1

Bateman et al. (1984)

The Dinkey Creek granodiorite is dominated by feldspars (~58 vol. %) and quartz (22.5 vol. %) mineral phases (Table 1.3). These framework silicates generally have lower to intermediate Ge/Si ratios. Not surprisingly, given the abundance of feldspars in the bedrock, the granodiorite Ge/Si ratio is 1.9 pmol μmol^{-1}. This ratio is within range of values reported for feldspars and other granites (Evans and Derry, 2002; Kurtz et al., 2002). Seismic refraction in the P301 sub-catchment of Providence Creek has shown that the depth to un-weathered bedrock can be as deep as 35 m (Holbrook et al., 2014) (Figure 1.3). Most of this thick regolith is composed of saprolite and moderately weathered bedrock.

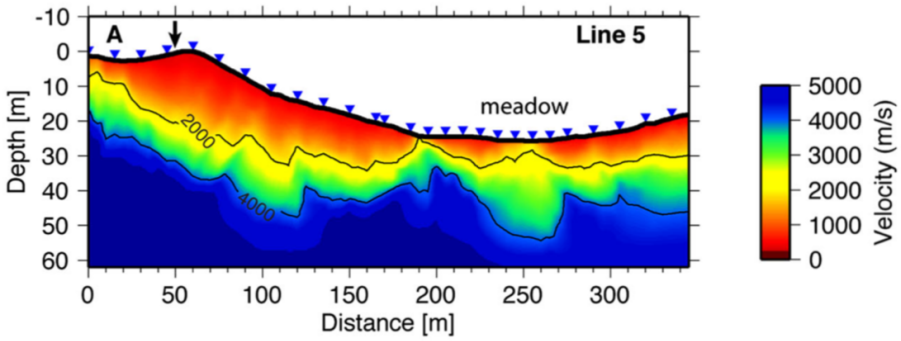

Figure 1.3: Seismic velocity profile of P301. The high velocity regions (blue) represent un-weathered bedrock. Above fresh bedrock, there is a region of moderately weathered to weathered regolith that can be 35 meters thick. This figure is adapted from Holbrook et al. (2014).

Soils at Providence Creek are thin ranging between 1.0-1.5 m in thickness. Soil thickness can vary from less than 0.50 m to greater than 1.50 m across short distances. This is strongly influenced by the slope of the terrain. Steeper slopes have shallower soils (<0.5 m) while gently sloped terrain can have soil depths of around 1.0 m (Bales et al., 2011). Average soil depth between Providence and Bull Creek does not differ significantly with depths averaging around 0.75 m (Johnson et al., 2011). However, the weathering rate at Providence Creek is greater than sites above and below its elevation (Dixon et al., 2009a). In other words, the mid elevation catchments of Providence Creek (1479-2113 m) are at a weathering maximum. Hence the thick regolith observed in P301 (Figure 1.3). This may be a consequence of temperature and distribution of precipitation. While lower elevation sites are warmer, they receive less precipitation inhibiting removal of solutes. At higher elevations, temperatures are cooler and most precipitation falls in the winter as snow. Therefore, cooler temperatures and rapid snowmelt runoff significantly inhibit chemical weathering (Dixon et al., 2009b).

The bulk chemistry and Ge/Si ratios of soils in P301 indicate minor loss of Si

and other base cations from chemical weathering (Table 1.4).

Table 1.4: P301 soil chemistry and Ge/Si ratios.

Depth	SiO_2	Al_2O_3	MgO	CaO	Na_2O	Ge/Si
m			wt. %			pmol µmol^{-1}
0.7	54.2%	17.5%	1.2%	3.1%	2.7%	2.21
1.7	52.9%	18.2%	1.4%	3.1%	2.6%	2.19
2.7	55.4%	19.1%	1.8%	3.7%	2.3%	2.16
3.7	55.6%	19.0%	1.9%	3.8%	2.4%	2.08
4.7	56.8%	19.5%	2.8%	4.8%	3.3%	2.20
5.7	53.2%	17.2%	2.0%	4.4%	3.2%	2.00
6.7	58.1%	17.7%	2.4%	4.3%	3.0%	2.00
7.7	58.3%	17.8%	2.3%	4.5%	3.2%	1.89
8.7	58.5%	17.5%	3.1%	4.7%	3.1%	2.17
9.7	57.3%	17.2%	2.8%	4.9%	3.1%	2.11
10.7	57.2%	16.5%	1.9%	5.2%	4.0%	1.88
11.4	59.0%	13.2%	0.0%	0.7%	3.3%	1.73

At 11.4-meter depth, SiO_2 concentration are similar to the Dinkey Creek granodiorite (Table 1.2). Moving upwards in the profile, SiO_2 concentrations gradually decrease to 54.2 wt. %. In tandem, base cations like Ca and Na decrease closer to the surface. This suggests some mass loss as a result of plagioclase weathering. Conversely, Al and Ge/Si increase closer to the surface. This is an indicator of secondary aluminosilicate formation resulting from the weathering of plagioclase. Since the depth to the weathering front can be as deep as 35 m, this data is only as snapshot of the chemistry of the altered sub-surface of KREW.

Soil orders at KREW are Entisols and Inceptisols composed of the Shaver, Gerle-Cagwin and Cagwin soil families (Giger, 1993). The Cagwin and Gerle-Cagwin soils are found at higher elevations of Providence Creek and all of Bull Creek (1800-

2400 m). The last glacial advance is believed to have terminated at 1800 m. Therefore, soils are less developed above this threshold with a bedrock contact within 1.0 m depth (Bales et al., 2011) The Shaver soils are predominant at lower elevations (1750-1900 m) below the extent of Pleistocene glaciation (Giger, 1993). As a result, the soils are more weathered with a greater regolith thickness. Additionally, the Shaver soils have a higher clay content than the Cagwin and Gerle-Cagwin soils found at Bull Creek (Bales et al., 2011).

The climate gradient of the Sierras and Pleistocene glaciation has resulted in different geologic contexts for Providence and Bull Creek. The warmer and rain-dominated Providence Creek has experienced greater weathering resulting in a thick and highly porous regolith (Holbrook et al., 2014). Additionally, most catchment area is at or below the extent of the glacial advance. Therefore, soils developed without glacial scouring that may have removed the upper layer of soil. These factors have significant implications for the hydrology at Providence Creek. The highly fractured and porous sub-surface has resulted in greater groundwater storage as shown by a higher baseflow to total stream flow ratio (baseflow index) than Bull Creek (Safeeq and Hunsaker, 2016).

There is still an incomplete understanding of sub-surface structure at Bull Creek. Seismic refraction studies were not conducted at these upper elevation catchments (Holbrook et al., 2014). Nonetheless, the baseflow index has demonstrated that Bull Creek has a lower groundwater storage than Providence Creek (Safeeq and Hunsaker, 2016). This difference may reflect thinner, less fractured regolith. Porosity in the Bull catchments may also be lower due to a slower weathering rates (Dixon et al., 2009a).

Additionally, glacial scouring may have reset soil development leading to a shallower contact zone with un-weathered bedrock. In this study, we will explore how these differences in CZ structure have implications on weathering processes and hydrologic flow paths.

1.3 Methods

Stream grab samples were collected at gauging station outlets in each sub-catchment of KREW (Figure 1.1). Soil pore water was collected using suction cup lysimeters (Prenart Equipment ApS) at sampling depths of 10 and 30 cm. Snow collection sites included meteorological stations and at soil Prenart sampling locations (Figure 1.1). Soil pore water and snow samples were analyzed only for the Providence catchments. All aqueous samples were collected in HNO_3 washed high density polyethylene bottles (HDPE) on a bi-weekly to monthly basis. Filtration was done in the lab with a 0.2 μm cellulose nitrate membrane filters (GE Whatman™). The filtered samples were then acidified to a pH less than 2.0 using trace metal grade HNO_3 (70% BDH Aristar® Plus). Soil samples from P301 were collected using Geoprobe® in 2012 by Cliff Riebe and Jorden Hayes. This drilling technique specializes in soil core sampling. The soils were crushed to a fine powder using a boron carbide mortar and pestle. Subsequently, the samples were ignited in a muffle furnace for 30 minutes at 900 ^{o}C then weighed to determine loss on ignition mass (LOI). The LOI mass was used to calculate element concentrations. A flux with a 1:1 ratio of lithium tetraborate and lithium metaborate was mixed with the sample in a ratio of 2:1. This flux and sample mixture was heated in the furnace at 1050^{o} C to form a glass bead. The bead was poured

into 50 ml of 10% HNO_3 and shaken overnight until the glass completely dissolved. The final dilution was prepared in 2% HNO_3. Samples were analyzed using inductively coupled plasma optical emission spectroscopy (ICP-OES; AMETEK SpectroBlue) at Cornell University to determine major cation concentrations. Stream water was not corrected for precipitation inputs of dissolved solutes because Cl^- data was not available for this dataset. Silicon inputs from precipitation are negligible but Mg, Ca and Na can be significantly deposited from arid and coastal regions (Kennedy et al., 1986; Aciego et al., 2017). Germanium was analyzed using hydride-generation ICP-mass spectrometry (Mortlock and Froelich, 1996). Samples were prepared using isotope dilution analysis (IDA) for the accurate determination of trace germanium concentrations only in stream and soil pore waters. Silicon concentrations in snow were very low (less than 5 μM). Therefore, Ge concentrations of snow was too low for accurate analysis. An enriched ^{70}Ge tracer solution (spike) was added to the water samples and equilibrated for at least 24 hours at 60 ^{o}C. The target $^{70}Ge/^{74}Ge$ in the sample was 10, corresponding to the geometric mean between the natural (0.56) and the spike (162) $^{70}Ge/^{74}Ge$ ratios. The target ratio corresponds to the lowest analytical uncertainty for IDA (Heumann, 1988; Mortlock and Froelich, 1996). The samples were introduced into the hydride system along with a 4% $NaBH_4$ solution that promoted the reduction of germanic acid ($GeOH_4$) to a volatile hydride (GeH_4) that was then transported by argon gas into the ICP-MS (Thermo-Finnigan Element 2). Germanium was quantified both by standard curve method and isotope dilution using the $^{70}Ge/^{74}Ge$ ratio. Corrections for mass bias and signal drift were done using sample-standard bracketing. At the same time, response curves were established by analysis of Ge standards at 5, 20, 50, 100,

200 and 500 ng L^{-1}. Additionally, the results from isotope dilution calculations were cross-checked against the standard response curves measured at m/z =74. With ($^{70}Ge/^{74}Ge$) spike = 162, the spike contribution to m/z 74 is negligible. The analytical uncertainty of the Ge measurement by IDA was quantified using error propagation of the compositional uncertainties of the measured isotopes (Heumann, 1988). This is assuming the that the contribution to uncertainty from the spike addition and isotopic abundances are negligible so that they can be ignored.

Model fits for concentration-discharge relationships were determined using the polyfit function in MatLab® (R2017b). Additionally, the corrcoef function was used to extract the correlation coefficients and the p-values for testing that there is no relationship between C-Q (null-hypothesis). Lastly, a cubic spline interpolation of the Si flux values was performed using the spline function. The trapezoidal numerical integration technique was applied to the Si flux curve using the trapz function.

1.4 Results

1.4.1 Seasonal variations in silicon and Ge/Si

Silicon concentrations show dilution during the snowmelt period of February 17th to May 4th, 2009 in the Providence Creek catchments (Table 1.5 and Figure 1.4). The fall and summer are characterized by the highest solute concentrations for WY2009. In the fall, silicon concentrations at P301 and P303 were between 330 and 497 μM respectively. Concentrations dropped to 280 and 342 μM respectively at the onset of the snowmelt period. By the summer when the hydrograph relaxed to baseflow levels, Si concentrations increased to around 450 μM. The pattern at P304 experiences only minor

dilution during snowmelt. Concentrations in the fall are 442 μM and drop to 382 μM in April. This behavior may be associated with the greater groundwater storage at P304 that supplies most discharge to the stream. In D102 the decrease in Si concentration is less pronounced than in the other catchments. During the fall, concentrations are between 488 and 501 μM until the January 24th pulse were concentrations increased to 702 μM. At the start of the snowmelt period, discharge increased to 3 mm day^{-1} and Si concentrations dropped to 320 μM. After this decrease, silicon gradually increases to around 500 μM by the end of WY2009. Overall, D102 has higher baseflow Si concentrations but is strongly affected by dramatic shifts in discharge. These two anomalous samples are likely associated with storm runoff because they occur during sharp hydrograph pulses. The January 24th pulse also resulted in spikes of Al and Fe but dilution of other solutes (Table 1.5). Colloidal transport of aluminosilicates has been observed in upper-montane snow dominated catchments like Gordon Gulch in the Boulder Creek CZO (Aguirre et al., 2017). However, at D102 we do not see a corresponding spike in Ge/Si that would fingerprint suspended aluminosilicates. Instead, the low Ge/Si ratios and anomalously elevated Si concentrations would suggest biogenic Si dissolution from the shallow soil. However, mixed-conifer forests are some of the lowest accumulators of biogenic SiO_2 (Bartoli, 1983; Conley, 2002). The most likely explanation is return flow. This flow regime occurs when infiltrated precipitation flowing downslope encounters saturated areas and is forced to reemerge onto the ground surface. In the case of the low Si sample in D102 at the onset of the snowmelt period, we may be seeing the dominance of surface runoff from the snowpack. Snow has very low Si concentrations (mean of 2.2 μM refer to Appendix 1).

Table 1.5: Providence Creek stream chemistry for WY2009.

Date	Catchment	Discharge mm day-1	Na (µM)	Mg (µM)	Ca (µM)	K (µM)	Si (µM)	Al (µM)	Sr (µM)	Fe (µM)	Ge (pM)	Ge/Si (pmol µmol-1)
11/4/2008	P301	0.19	168	21.0	95.0	22.5	370	0.54	0.52	0.29	27.7	0.07
11/26/2008	P302	0.13	173	21.0	93.9	21.0	367	0.40	0.55	0.15	23.0	0.06
1/27/2009	P303	0.76	151	16.6	75.8	17.9	331	0.64	0.41	0.41	26.5	0.08
2/23/2009	P304	1.42	149	17.6	81.7	18.0	280	0.65	0.44	0.52	20.7	0.07
3/30/2009	P305	1.51	121	17.5	77.0	18.8	293	0.42	0.47	0.37	23.3	0.08
4/28/2009	P306	2.11	129	15.1	68.5	14.0	306	0.75	0.42	0.45	23.8	0.08
5/12/2009	P307	1.72	147	16.2	77.2	15.9	298	0.57	0.44	0.47	29.6	0.10
6/29/2009	P308	0.49	170	22.1	100	19.1	438	0.79	0.65	0.23	27.2	0.06
7/28/2009	P309	0.18	210	24.2	115	21.8	443	0.49	0.67	0.50	34.1	0.08
8/25/2009	P310	0.08	188	25.7	120	23.3	433	0.28	0.69	0.13	35.5	0.08
11/4/2008	P303	0.05	214	47.3	184	28.6	498	0.13	1.15	0.23	32.3	0.06
11/26/2008	P304	0.04	227	44.5	163	30.8	458	0.18	1.00	0.19	30.6	0.07
1/27/2009	P305	0.31	214	26.7	94.9	19.6	426	0.29	0.54	0.15	30.5	0.07
2/24/2009	P306	1.09	159	24.0	85.6	19.0	342	0.55	0.49	0.19	24.1	0.07
3/30/2009	P307	1.04	160	25.3	89.9	17.2	322	0.34	0.54	0.11	22.7	0.07
6/29/2009	P308	0.16	211	37.3	136	26.1	392	0.11	0.81	0.12	44.4	0.11
7/28/2009	P309	0.06	237	44.1	178	33.1	569	0.20	1.03	0.22	50.6	0.09
8/25/2009	P310	0.04	215	47.5	184	31.4	458	0.13	1.06	0.15	34.2	0.07
11/4/2008	P304	0.57	211	47.0	199	37.3	443	0.64	1.13	0.71	23.4	0.05
11/26/2008	P305	0.53	209	41.8	168	33.3	416	0.31	0.92	0.48	31.9	0.08

continued on next page

Table 1.5 (*continued*)

Date	Catchment	Discharge mm day^{-1}	Na (µM)	Mg (µM)	Ca (µM)	K (µM)	Si (µM)	Al (µM)	Sr (µM)	Fe (µM)	Ge (pM)	Ge/Si (pmol µmol^{-1})
12/10/2008	P306	0.37	223	47.4	208	27.1	484	0.36	1.13	0.28	23.1	0.05
1/27/2009	P307	0.78	201	41.9	155	25.3	398	0.33	0.92	0.30	22.8	0.06
2/24/2009	P308	1.12	191	38.6	141	23.9	384	0.38	0.80	0.54	22.0	0.06
3/30/2009	P309	1.06	205	40.9	152	25.4	382	0.24	0.84	0.24	24.1	0.06
5/12/2009	P310	0.87	218	43.4	159	29.7	480	0.30	1.00	0.30	34.6	0.07
6/29/2009	P311	0.56	226	44.4	192	20.9	435	2.11	1.04	0.27	27.3	0.06
7/28/2009	P312	0.45	231	43.7	178	22.8	452	0.43	1.03	0.25	20.2	0.04
8/25/2009	P313	0.39	246	48.8	185	37.8	478	0.34	1.14	0.58	19.3	0.04
11/4/2008	D102	0.21	252	34.0	148	36.8	502	0.73	0.85	0.54	22.0	0.04
11/26/2008	D103	0.12	245	34.1	144	40.1	465	0.20	0.78	0.45	13.7	0.03
12/10/2008	D104	0.10	255	32.3	147	27.9	489	0.12	0.77	0.16	13.2	0.03
1/27/2009	D105	0.61	203	25.5	107	22.1	703	1.49	0.56	0.60	21.5	0.03
2/24/2009	D106	1.82	197	21.7	89.5	22.6	320	0.68	0.48	0.41	19.6	0.06
3/28/2009	D107	1.25	204	23.2	99.9	22.0	417	0.39	0.54	0.25	19.8	0.05
4/28/2009	D108	0.77	190	27.3	114	25.4	440	0.47	0.66	0.14	27.8	0.06
5/12/2009	D109	0.65	238	26.4	116	25.6	421	0.39	0.64	0.13	21.4	0.05
6/29/2009	D110	0.26	233	27.7	125	26.5	450	0.12	0.70	0.23	22.7	0.05
7/28/2009	D111	0.11	261	31.5	145	30.5	522	0.33	0.80	0.21	28.1	0.05
8/25/2009	D112	0.08	263	32.7	152	28.9	513	0.25	0.88	0.21	17.4	0.03

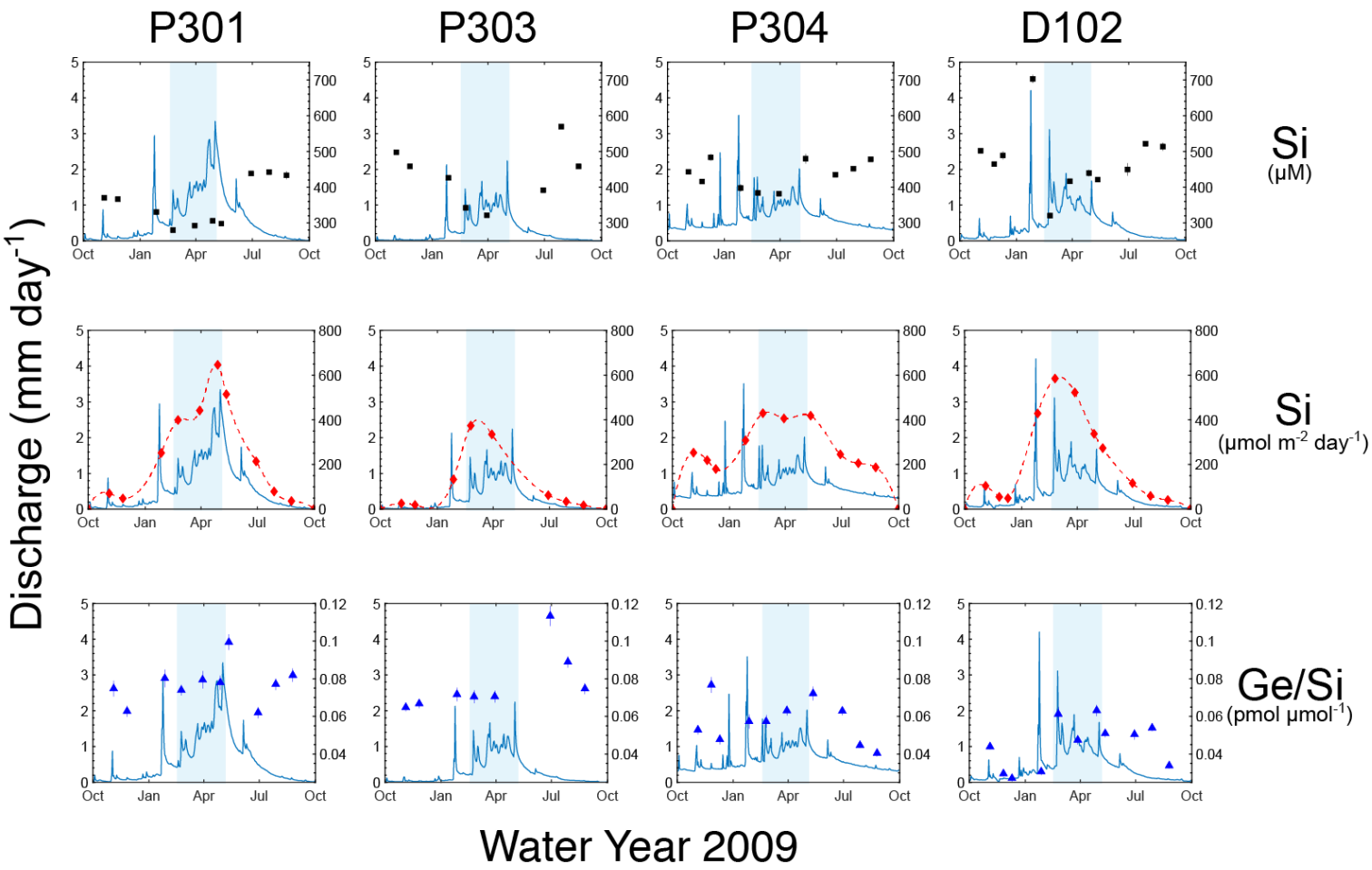

Figure 1.4: Providence Creek stream chemistry for WY2009. Si (μM), Si flux (μmol m^{-2} day^{-1}) and Ge/Si (pmol μmol^{-1}) for WY2009. Discharge is shown in blue and the snowmelt period (February 17th to May 5th, 2009) is represented by the light blue region.

Snowmelt runoff may have been rapidly transported by macropore flow to the stream. These anomalous samples obscure the rather simple dilution trend during the snowmelt period that is also observed in other catchments.

Silicon concentrations at Providence Creek show consistent dilution during the snowmelt period. However, the Si flux is highest during snowmelt and represents between 32-59% of the annual Si flux (Appendix 2). This indicates that chemical weathering is highest during snowmelt infiltration. Catchments P301 and D102 have the highest flux in Providence Creek during peak discharge. In P301, the flux was around 645 μmol m^{-2} day^{-1} when discharge was 2.1 mm day^{-1}. Silicon flux in D102 was slightly less at 584 μmol m^{-2} day^{-1} when stream discharge was 1.8 mm day^{-1}. The Si flux at P303 and P304 increases gradually to 400 μmol m^{-2} day^{-1} and plateaus for the rest of the snowmelt season. The Si flux pattern is significantly dependent on discharge. That is why P303 and P304 do not have a sharper increase in flux during the snowmelt period.

Ge/Si ratios in Providence Creek are below 0.12 pmol $\mu$$mol^{-1}$ and do not show a clear response with discharge or snowmelt. In P301, the ratio increases from baseflow at 0.06 to 0.09 pmol $\mu$$mol^{-1}$ by the end of the snowmelt period. However, most ratios leading up to maximum discharge are essentially identical to baseflow in the fall (Figure 1.4). In P303, Ge/Si does not vary significantly from the baseflow ratio of 0.06 pmol $\mu$$mol^{-1}$ even during the snowmelt period. Ge/Si peaks at 0.11 pmol $\mu$$mol^{-1}$ in June 29th then gradually decreases to 0.07 pmol $\mu$$mol^{-1}$ as the hydrograph relaxes. For P304 and D102, the Ge/Si range is smaller. In P304, there is a clear increase in Ge/Si during the snowmelt period. Maximum Ge/Si in P304 reached 0.07 pmol $\mu$$mol^{-1}$ then gradually decreased to 0.04 pmol $\mu$$mol^{-1}$ by August 25th. In D102, baseflow ratio was lowest at

0.02 pmol μmol^{-1} then increased to 0.06 pmol μmol^{-1} during the snowmelt period and remained at that level for most of the summer. Given the very low Ge/Si ratios, the variations among sites can be given less weight in the analysis. Overall, Ge/Si does not vary significantly with snowmelt infiltration. This reflects a dominant Si source from incongruent weathering of primary minerals because the Ge/Si ratio is less than 0.5 pmol μmol^{-1}. During higher discharge, we would expect elevated Ge/Si as soil water that has interacted with secondary minerals is displaced by infiltrating snowmelt. Since Si dilution is observed during the snowmelt period in all catchments, infiltrating snowmelt must be transported rapidly to the stream. This end-member may be analogous to event water during rain events. The Ge/Si patterns shows that snowmelt infiltration and Si dilution does not affect the Ge/Si dynamics of the system. Instead, groundwater flow is a major contributor of Si such that the smaller contribution from the shallow soil reservoir does not significantly affect the Ge/Si mass balance. This observation is supported by end-member mixing analysis (EMMA) in Providence Creek that suggests that groundwater can contribute more than 80% of discharge to the stream. The same study found that soil pore water is not a quantitatively important end-member to the system (Liu et al., 2013).

In Bull Creek, Si concentrations are generally lower than 300 μM with a clear dilution pattern during the snowmelt period (Table 1.6 and Figure 1.5). In B201, baseflow Si concentrations are around 200 μM then decrease to 65 μM by April 28th near snowpack depletion. Silicon concentrations then sharply increase during the summer and early fall to 318 μM. In B203, baseflow concentrations are lower, ranging between 90-150 μM then decrease to 36 μM during the snowmelt period. These Si

concentrations are some of the lowest measured in the study. By the summer in B203, concentrations increase to 150 μM. The B204 catchment shows the most consistent baseflow concentrations during the fall and summer with minor dilution. Baseflow ranges between 150 and 185 μM then experiences dilution during the snowmelt period to only 100 μM. For T003, the Si pattern resembles the pattern of B201 with a gradual decrease in concentration from 290 μM to 157 μM by the end of the snowmelt period. Stream Si concentrations increase to 250 μM in September, this is the only observation in the fall 2009. The Si flux in Bull Creek is also very dependent on discharge but is lower than Providence Creek (Appendix 2 and Figure 1.4). During baseflow, silicon flux is less than 100 μmol m^{-2} day^{-1} throughout Bull Creek but increases during the snowmelt season. Peak Si flux occurs near snow pack depletion during peak discharge. The highest flux was 1529 μmol m^{-2} day^{-1} on May 7th, 2009 in the T003 catchment. This was six days after peak discharge of 12 mm day^{-1}. Catchments B203 and B204 had similar Si flux patterns where baseflow flux was around 40 μmol m^{-2} day^{-1} then increased to 288 and 413 μmol m^{-2} day^{-1} respectively. Interestingly, B203 did not have the highest Si flux even though this catchment had the highest discharge in Bull Creek with 19 mm day^{-1} on May 2nd, 2009. This may be due to sample bias since stream water collection was done on a bi-weekly to monthly basis. Therefore, the peak Si flux may have occurred before sample collection at this site and may have been greater than observed at T003. Total annual Si flux at B201-204 was lower than the flux in Providence Creek.

Table 1.6: Bull Creek stream chemistry for WY2009.

Date	Catchment	Discharge mm day-1	Na (μM)	Mg (μM)	Ca (μM)	K (μM)	Si (μM)	Al (μM)	Sr (μM)	Fe (μM)	Ge (pM)	Ge/Si (pmol μmol-1)
11/4/2008	B201	0.4	119	12.5	49.0	28.0	201	0.73	0.19	1.04	25.6	0.13
11/26/2008	B201	0.6	117	8.88	39.5	20.6	162	0.43	0.00	0.81	22.0	0.14
12/9/2008	B201	0.2	111	11.5	58.6	11.4	194	0.23	0.16	0.43	23.6	0.12
2/25/2009	B201	0.9	99.1	10.3	39.9	0.00	124	0.24	0.13	0.71	18.9	0.15
3/31/2009	B201	1.5	95.5	9.04	34.0	9.37	94.2	0.23	0.12	0.63	20.4	0.22
4/28/2009	B201	3.0	94.9	6.75	28.8	8.45	65.1	0.59	0.00	0.65	32.4	0.50
5/13/2009	B201	2.5	81.1	7.40	34.3	0.00	102	0.28	0.11	0.57	31.0	0.30
7/28/2009	B201	0.3	77.4	14.5	71.3	5.96	237	0.22	0.25	0.48	40.1	0.17
8/25/2009	B201	0.2	112	14.0	70.3	8.92	319	0.49	0.21	0.48	36.0	0.11
11/5/2008	B203	0.3	106	9.78	30.6	18.6	91.1	0.22	0.00	0.53	27.8	0.31
11/26/2008	B203	0.3	112	7.86	24.1	13.3	120	0.24	0.09	0.29	23.1	0.19
12/9/2008	B203	0.2	102	8.28	27.5	9.17	149	0.12	0.10	0.21	23.0	0.15
1/28/2009	B203	1.0	85.4	6.18	19.4	0.00	40.2	0.38	0.07	0.36	35.1	0.87
2/25/2009	B203	1.1	52.6	6.80	19.5	9.40	66.2	0.20	0.00	0.33	30.8	0.46
3/31/2009	B203	2.9	50.4	5.91	16.5	5.91	61.5	0.23	0.07	0.24	37.5	0.61
4/28/2009	B203	4.9	303	6.18	20.3	0.00	36.8	0.88	0.08	0.28	29.3	0.80
5/13/2009	B203	7.5	75.0	4.76	15.0	0.00	38.2	0.47	0.06	0.30	34.9	0.91
6/29/2009	B203	0.8	55.8	7.47	22.3	5.94	118	0.27	0.00	0.37	37.9	0.32
7/28/2009	B203	0.5	96.5	8.68	30.6	0.00	163	0.38	0.12	0.37	39.6	0.24
8/25/2009	B203	0.2	104	9.06	30.4	6.65	125	0.09	0.00	0.30	30.1	0.24

continued on next page

Table 1.6 (*continued*)

Date	Catchment	Discharge mm day-1	Na (μM)	Mg (μM)	Ca (μM)	K (μM)	Si (μM)	Al (μM)	Sr (μM)	Fe (μM)	Ge (pM)	Ge/Si (pmol μmol^{-1})
8/25/2009	B204	0.2	77.5	9.99	39.9	10.9	185	0.27	0.19	0.17	32.5	0.18
11/5/2008	B204	0.2	108	10.5	45.0	18.4	177	0.37	0.17	0.32	28.0	0.16
11/26/2008	B204	0.2	106	8.96	39.0	11.0	179	0.17	0.15	0.25	25.4	0.14
2/25/2009	B204	0.7	101	9.57	39.0	11.1	146	0.13	0.15	0.47	29.8	0.20
3/31/2009	B204	1.5	95.0	8.87	35.7	8.42	106	0.16	0.18	0.46	38.0	0.36
4/28/2009	B204	4.2	82.5	6.92	26.0	0.00	99.3	0.22	0.11	0.28	30.6	0.31
6/29/2009	B204	0.9	64.1	8.66	32.1	6.39	163	0.31	0.16	0.28	40.3	0.25
7/28/2009	B204	0.4	102	8.90	38.0	0.00	151	0.00	0.17	0.19	38.1	0.25
1/28/2009	T003	1.4	126	14.2	64.5	14.0	211	0.57	0.21	0.21	20.5	0.10
11/5/2008	T003	0.4	132	17.3	80.4	22.8	252	0.56	0.26	0.28	19.7	0.08
11/26/2008	T003	0.3	129	16.9	79.5	18.8	244	0.33	0.27	0.17	14.2	0.06
12/9/2008	T003	0.2	112	17.8	84.9	18.7	289	0.20	0.29	0.09	17.8	0.06
2/24/2009	T003	1.3	97.8	13.6	59.7	15.9	158	0.49	0.20	0.29	16.1	0.10
3/30/2009	T003	1.7	107	13.0	60.6	12.5	196	0.32	0.19	0.24	20.9	0.11
5/7/2009	T003	9.6	93.7	11.0	47.8	10.4	159	0.52	0.17	0.19	22.5	0.14
8/25/2009	T003	0.3	130	18.4	85.2	14.4	249	0.33	0.29	0.15	20.7	0.08

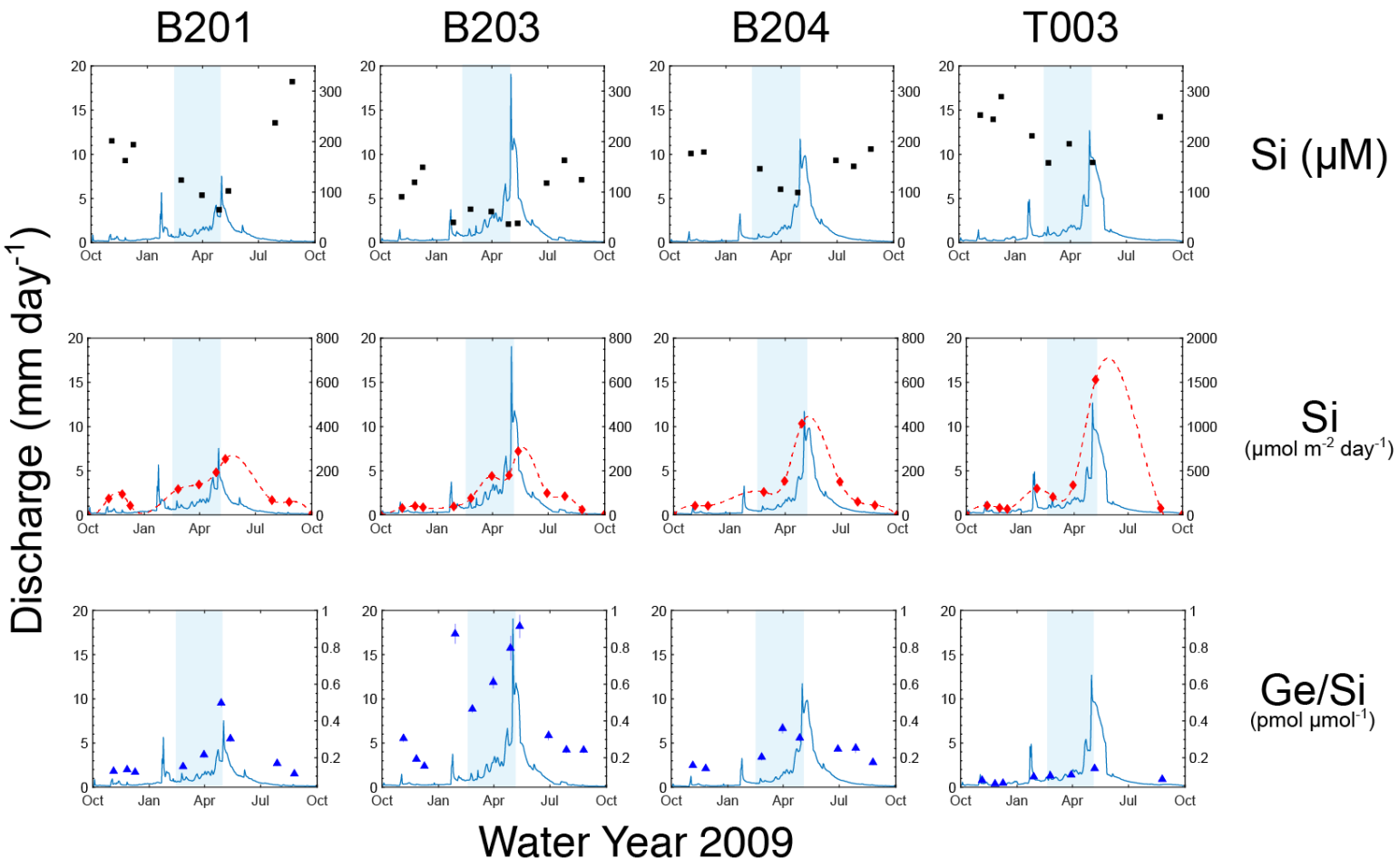

Figure 1.5: Bull Creek stream chemistry for WY2009. Si (µM), Si flux (µmol m^{-2} day^{-1}) and Ge/Si (pmol μmol^{-1}) for WY2009. Discharge is shown in blue and the snowmelt period (February 17th to May 5th, 2009) is represented by the light blue region.

T003 had the highest annual flux of more than 190,000 μmol m^{-2}. However, we only have one observation at peak discharge (May 7th) and in September 25th. Therefore, we cannot validate the goodness of fit of the spline interpolation during this period of apparent high flux. Nonetheless, there are clear differences in flux between Providence and Bull Creek. The Si flux during snowmelt at Bull Creek constituted around 30% of the total while Providence was up to 59%. Additionally, the majority of the Si flux in Bull Creek occurred once the snow depleted and during hydrograph recession.

The Ge/Si patterns at Bull Creek are dramatically different from Providence Creek. In Bull Creek, ratios increase to 0.9 pmol $\mu$$mol^{-1}$. Additionally, Ge/Si increases with discharge and snowmelt infiltration as observed in B201, B203, B204 and to a lesser extent in T003. The best example of this process is in B203 during the snowmelt period. Baseflow ratios are around 0.3 pmol $\mu$$mol^{-1}$ then gradually increase to 0.9 pmol $\mu$$mol^{-1}$ after peak discharge. In B201 and B204, Ge/Si also increases during the snowmelt period but less dramatically than in B203. Baseflow in both catchments ranges between 0.1-0.2 pmol $\mu$$mol^{-1}$ then increases to 0.49 pmol $\mu$$mol^{-1}$ for B201 and 0.36 pmol $\mu$$mol^{-1}$ for B204. The ratio in T003 does not increase significantly with changes in hydrologic conditions. The Ge/Si ratio ranges between 0.05 and 0.15 pmol $\mu$$mol^{-1}$ in a similar way to Providence Creek. The T003 catchment has a different slope aspect (south) compared to B201-204. This should have an effect on the water balance that can influence the weathering processes at this site (Anderson et al., 2010). Considering only Ge concentrations in the Bull catchments, Ge concentrations are not significantly different than in Providence Creek (Table 1.5 & 1.6). Germanium concentrations range between 20-30 pM in the entire KREW study site. The difference

between sites are Si concentrations. Providence Creek baseflow concentrations are 500 μM while Bull Creek concentrations are around 200 μM. The Ge/Si ratios are driven by differences in Si concentrations. These upper elevation catchments have been characterized as highly leaching environments with significant desilication as a result of snowmelt (Dahlgren et al., 1997). With the elevation gradient and its effect on the distribution of snow in these catchments, the expectation is that Bull Creek should be more intensely leached since it develops a larger snowpack (Safeeq and Hunsaker, 2016). However, observations show that Providence has greater Si export (Figure 1.4). The greater regolith porosity in Providence may play an important role in the leaching conditions at this site.

1.4.2 Concentration-discharge relationships

The concentration-discharge relationships for the major cations in the Providence Creek catchments show generally negative power law exponents within the chemostatic range ($-0.2 < b < 0.0$) (Godsey et al., 2009; Herndon et al., 2015) (Figure 1.6 & Table 1.7). All sub-catchments of Providence Creek have chemostatic Si-Q relationships that are mostly statistically significant with 95% confidence (Figure 1.7). The upper elevation catchments of P301 and P303 show very similar Si-Q patterns with

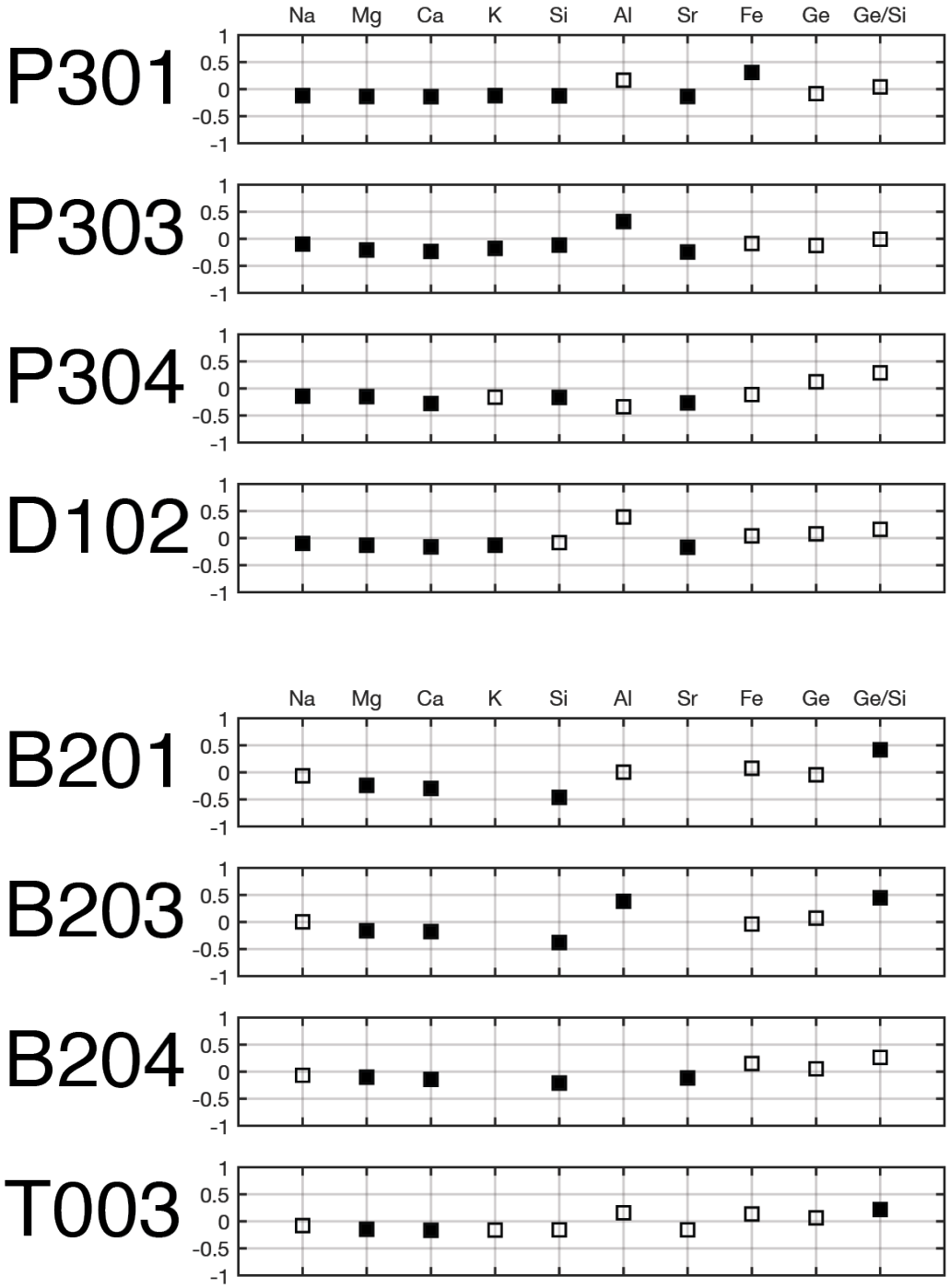

Figure 1.6: KREW C-Q exponents. C-Q and Ge/Si-discharge power law exponents for the KREW sub-catchments. Filled markers are statistically significant with 95% confidence.

Table 1.7: Providence Creek solute-discharge and Ge/Si-discharge power law exponents and constants.

		Na	Mg	Ca	K	Si	Al	Sr	Fe	Ge	Ge/Si
P301											
	a	146.03	17.69	80.97	17.52	322.88	0.59	0.47	0.39	25.35	0.08
	b	-0.12	-0.14	-0.14	-0.12	-0.12	0.17	-0.13	0.31	-0.08	0.04
	R^2	0.71	0.75	0.70	0.83	0.67	0.21	0.56	0.40	0.25	0.22
	p-value	0.00	0.00	0.00	0.00	0.00	0.19	0.01	0.05	0.14	0.17
P303											
	a	168.76	24.24	85.74	17.94	342.15	0.38	0.50	0.14	25.79	0.08
	b	-0.10	-0.21	-0.23	-0.18	-0.12	0.32	-0.24	-0.08	-0.12	-0.01
	R^2	0.92	0.75	0.72	0.74	0.67	0.78	0.70	0.10	0.45	0.05
	p-value	0.00	0.01	0.01	0.01	0.01	0.00	0.01	0.43	0.07	0.58
P304											
	a	201.49	40.70	151.51	25.75	401.13	0.37	0.87	0.35	25.97	0.06
	b	-0.14	-0.15	-0.28	-0.16	-0.16	-0.34	-0.27	-0.11	0.13	0.29
	R^2	0.57	0.65	0.72	0.12	0.49	0.04	0.71	0.01	0.03	0.20
	p-value	0.01	0.00	0.00	0.32	0.02	0.59	0.00	0.76	0.63	0.20
D102											
	a	205.14	24.49	103.64	23.74	427.23	0.56	0.57	0.28	22.03	0.05
	b	-0.10	-0.13	-0.16	-0.13	-0.08	0.39	-0.17	0.04	0.08	0.16
	R^2	0.66	0.80	0.84	0.42	0.28	0.10	0.79	0.01	0.01	0.32
	p-value	0.00	0.00	0.00	0.03	0.10	0.33	0.00	0.77	0.72	0.07

power exponents of -0.12. The y-intercepts are similar at 322 and 342 μM respectively. Both catchments display initial dilution with increasing discharge until Si concentrations plateau at around 300 μM. In the lower elevation catchments of P304 and D102, y-intercepts are higher but with a poorer model fit (R^2 of 0.49 and 0.28 respectively). The hydrograph of the P304 catchment is less responsive to snowmelt infiltration than P301 and P303. The higher groundwater storage in P304 results in sustained groundwater flow throughout the year. Discharge pulses may play a minor role in the Si-Q relationship at P304. The D102 catchment is an outlier showing a poor model fit ($R^2 = 0.28$) and no statistical significance between Si and discharge (p-value > 0.05). This is likely due to the January 24th pulse event where Si concentration surpassed 700 μM. This sample falls off the model fit causing the relationship with discharge to be poor. The power law exponents for the Ge/Si patterns are very close to zero (P301 and P303) or very positive (P304 and D102) (Figure 1.7). However, the model fits are poor and not statistically significant. Not surprisingly, we observed in WY2009 that the Ge/Si ratios in Providence Creek did not respond to changes in hydrologic conditions. Ge/Si ratios are consistently below 0.1 pmol μmol^{-1} and fall within a narrow and low range uncommon for most river systems (Froelich et al., 1992; Kurtz et al., 2011).

In Bull Creek, there was more variation in the solute-discharge patterns among sub-catchments (Table 1.8 & Figure 1.6). B201 had solute-discharge power law exponents less than -0.2 for Mg, Ca and Si (Table 1.8). In B203 and B204, solute-discharge patterns are within the chemostatic range for Na, Mg and Ca. However,

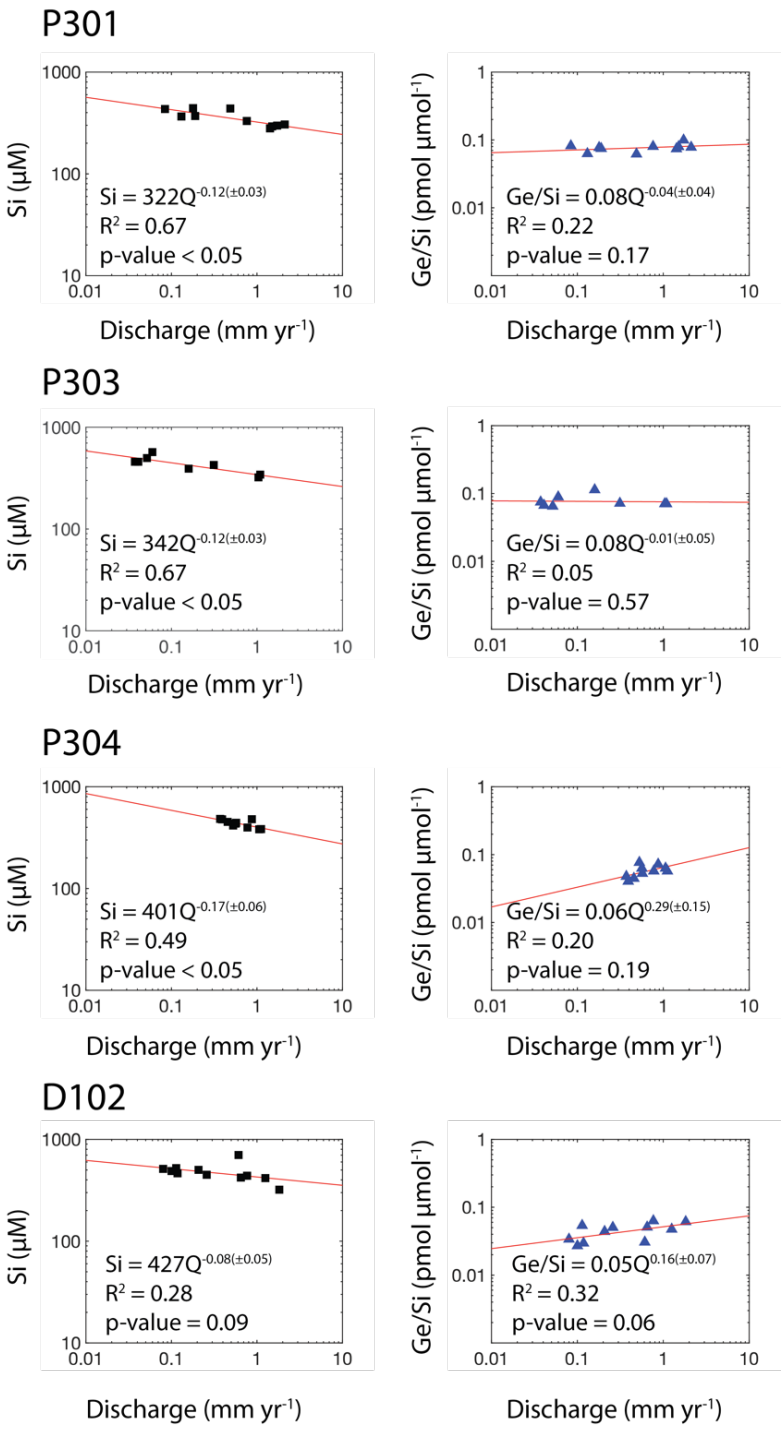

Figure 1.7: Providence Creek Si-Q and Ge/Si-Q relationships. The black markers are Si (µM) and the blue triangles are Ge/Si (pmol µmol^{-1}). The red line represents the model fit.

Table 1.8: Bull Creek solute-discharge and Ge/Si-discharge power law exponents and constants.

		Na	Mg	Ca	K	Si	Al	Sr	Fe	Ge	Ge/Si
B201											
	a	97.14	9.25	39.82	-	123.56	0.35	-	0.64	26.43	0.21
	b	-0.06	-0.24	-0.30	-	-0.46	0.00	-	0.07	-0.04	0.42
	R^2	0.24	0.73	0.62	-	0.66	0.01	-	0.00	0.00	0.88
	p-value	0.18	0.00	0.01	-	0.01	0.85	-	1.00	0.92	0.00
B203								-			
	a	91.01	7.07	22.15	-	76.67	0.28	-	0.31	31.51	0.41
	b	0.01	-0.16	-0.18	-	-0.38	0.38	-	-0.04	0.07	0.45
	R^2	0.08	0.63	0.50	-	0.47	0.44	-	0.07	0.06	0.61
	p-value	0.39	0.00	0.02	-	0.02	0.03	-	0.42	0.47	0.00
B204											
	a	88.02	8.56	33.99	-	132.90	-	0.15	0.31	33.29	0.25
	b	-0.07	-0.10	-0.14	-	-0.21	-	-0.11	0.15	0.05	0.26
	R^2	0.11	0.75	0.75	-	0.67	-	0.66	0.02	0.00	0.43
	p-value	0.43	0.01	0.01	-	0.01	-	0.01	0.73	0.93	0.08
T003											
	a	113.60	14.73	67.31	15.12	210.25	0.40	0.23	0.20	19.03	0.09
	b	-0.08	-0.14	-0.16	-0.16	-0.16	0.16	-0.16	0.14	0.06	0.22
	R^2	0.43	0.59	0.60	0.43	0.42	0.13	0.47	0.00	0.30	0.73
	p-value	0.08	0.03	0.02	0.08	0.08	0.38	0.06	0.92	0.16	0.01

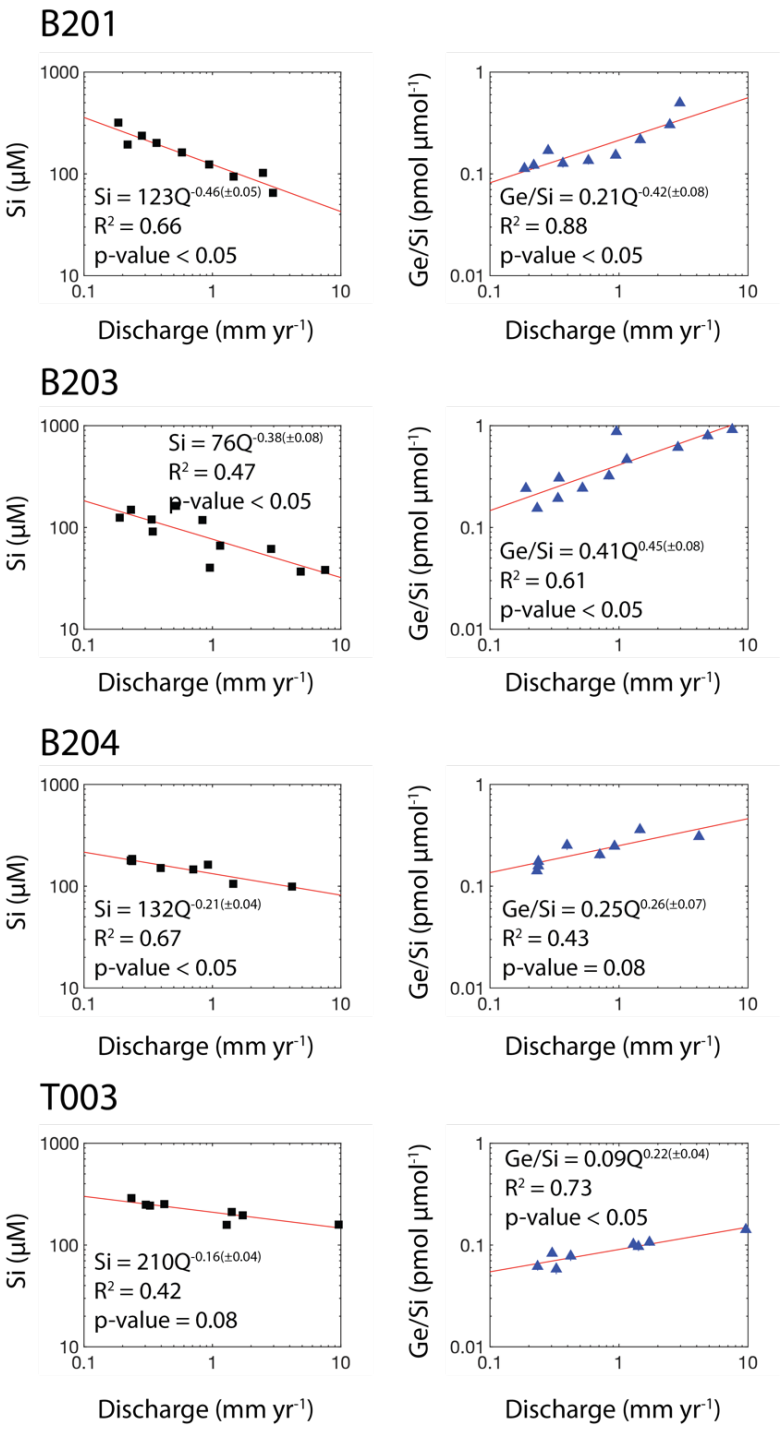

Figure 1.8: Bull Creek Si-Q and Ge/Si-Q power law relationships. The black markers are Si (µM) and the blue triangles are Ge/Si (pmol µmol^{-1}). The red line represents the model fit.

the Si-Q relationship in both catchments is not chemostatic with exponents of -0.38 and -0.21 (Figure 1.8). Catchment T003 had the most consistent C-Q relationships (Table 1.8). The elements of Na, Mg, Ca, K and Si had relationships within the chemostatic range. Surprisingly, the Ge/Si-discharge relationships in Bull Creek have power law exponents ranging between 0.22 and 0.45. The higher exponents corresponded to B201 and B203 with 0.42 and 0.45 respectively. As for B204 and T003, the exponents were above the chemostatic threshold with 0.26 and 0.22 respectively. It is evident that discharge at Bull Creek has a strong relationship with Ge/Si ratios. This was also observed over WY2009 where increased snowmelt led to higher ratios for B201-204. As opposed to Providence, the activation of shallow soil hydrologic pathways does affect mass balance at Bull Creek. This could suggest a stronger coupling between soil pore water and stream discharge that was not observed Providence Creek.

1.4.3 Soil pore water chemistry

Porewater samples were collected at soil Prenart lysemeter sites at depths of 10 and 30 cm in every sub-catchment of Providence Creek (Figure 1.1). Soil volumetric water content (VWC) displays a seasonal pattern in response to snowmelt infiltration (Figure 1.9). The shallow soil at 10 cm depth has higher VWC than the deeper 30 cm soil from October to January. This period corresponds to the wet season in this Mediterranean climate (Figure 1.2). Only during the dry season of July through October, VWC at 30 cm is greater than the 10 cm soil depth. During the dry season from May to October, root water uptake and ET exceed water inputs into the soil (Bales et al., 2011; Goulden et al., 2012). There are some significant differences between the chemistry of

soil water and stream water in our study. In soil water, concentrations for Na and Si are lower while Mg, Ca, K, Al, Sr and Fe are higher or similar to stream water concentrations (Table 1.9). Potassium is the only element in our dataset that appears significantly impacted by biota. The leaching of litterfall in the shallow soil is likely concentrating K in the soil water (Stallard and Murphy, 2014; Wymore et al., 2017). Soil water concentrations of Mg, Ca and Sr are within the same range as stream water in Providence Creek. Sodium is much lower in soil water than in stream water (Table 1.9). In stream water, sodium during baseflow is at least greater than 150 μM while in soil water it ranges between 50-70 μM.

Silicon concentrations in soil water are much lower than concentrations observed in stream water (Figure 1.9). Maximum Si concentrations are observed in P301 at 112 μM while the other catchments have highest concentrations around 70 μM. The most noticeable contrast between soil and stream water chemistry is with aluminum (Al). In stream water, Al was below 1.0 μM with some peaks above 1.0 μM occurring after periods of increased discharge (Table 1.5). In soil water, aluminum can be as high as 35 μM as observed in P304 (Figure 1.9). The increase in Al is followed by much higher Ge/Si ratios than in stream water. The highest Ge/Si was observed in P301 with 2.6 pmol μmol^{-1} in February at the beginning of the snow accumulation period. The higher Ge/Si ratios in these soil waters suggest that the source of silicon is an enriched Ge mineral phase. Both high Al and Ge/Si are clear indicators of weathering of secondary aluminosilicates.

The differences in moisture between the 10 to 30 cm depth do not seem to have an effect on soil water chemistry. In P301, silicon concentrations for samples at 30 cm

Table 1.9: Providence Creek soil pore water chemistry.

Date mm/dd/yyyy	catchment	Depth (cm)	Na (µM)	Mg (µM)	Ca (µM)	K (µM)	Si (µM)	Al (µM)	Sr (µM)	Fe (µM)	Ge (pM)	Ge/Si (pmol µmol-1)
3/24/2009	P303	26	68.1	44.8	178.2	143.4	45.6	2.9	0.6	0.3	47.1	1.03
3/24/2009	P303	13	57.2	35.4	228.6	355.7	32.3	5.0	0.8	0.6	53.8	1.66
3/25/2009	P301	13	68.1	54.9	343.4	186.3	48.0	20.4	1.2	2.5	90.3	1.88
4/21/2009	P301	26	125.7	103.6	521.7	626.6	112.8	15.2	1.8	2.0	39.1	0.35
5/5/2009	P303	26	44.1	42.6	164.1	140.5	60.7	5.8	0.6	1.5	84.7	1.39
2/3/2009	P301	13	68.6	40.8	220.1	181.1	32.3	15.3	0.7	1.2	86.9	2.69
3/25/2018	P301	26	44.0	64.6	284.7	467.6	58.7	5.2	1.1	0.9	55.2	0.94
3/24/2009	P304	13	96.8	35.5	138.4	73.4	47.9	35.4	0.4	1.8	61.7	1.29
4/21/2009	P301	13	52.2	54.8	343.1	216.4	44.3	17.1	1.2	2.0	66.9	1.51
3/24/2009	D102	26	64.0	47.0	175.1	141.6	56.6	1.4	0.5	0.3	47.1	0.83
5/5/2009	D102	26	64.7	42.5	159.3	144.2	73.7	1.8	0.5	0.4	71.7	0.97
4/22/2009	P304	26	70.2	28.4	88.4	64.5	48.5	3.9	0.3	0.3	76.7	1.58
4/22/2009	D102	26	56.7	44.5	163.5	139.4	65.2	1.8	0.5	0.3	53.0	0.81
2/3/2009	P303	13	59.0	31.1	134.2	69.4	60.1	0.9	0.5	0.1	57.1	0.95
2/3/2009	P304	26	89.9	34.9	112.5	43.3	36.2	1.3	0.4	0.1	48.0	1.33
2/4/2009	D102	13	58.9	46.6	242.9	131.8	40.7	3.1	0.7	0.5	43.5	1.07
5/5/2009	D102	13	72.1	28.9	114.5	76.9	32.4	8.0	0.3	0.8	69.5	2.14
2/3/2009	P303	26	24.2	44.7	135.9	96.7	74.6	1.4	0.6	0.6	49.8	0.67
5/5/2009	P304	26	68.0	22.0	76.5	30.2	65.7	0.5	0.3	0.0	59.5	0.90
1/21/2009	P301	26	65.1	57.1	220.1	416.6	87.4	2.1	0.9	0.6	58.2	0.67
1/21/2009	D102	13	65.6	41.1	205.9	109.1	51.8	2.1	0.5	0.3	46.3	0.89

continued on next page

Table 1.9 (*continued*)

Date mm/dd/yyyy	catchment	Depth (cm)	Na (µM)	Mg (µM)	Ca (µM)	K (µM)	Si (µM)	Al (µM)	Sr (µM)	Fe (µM)	Ge (pM)	Ge/Si (pmol µmol^{-1})
1/21/2009	P303	26	58.0	42.8	125.1	106.7	71.0	1.6	0.5	0.2	58.4	0.82
4/22/2009	P303	13	52.0	29.1	146.0	67.8	52.4	1.3	0.5	0.2	41.0	0.78
5/5/2009	P303	13	52.9	29.6	123.4	69.4	58.6	0.8	0.4	0.1	52.6	0.90
1/21/2009	P303	13	56.6	32.7	155.7	66.1	68.3	0.6	0.6	0.1	69.8	1.02
1/21/2009	P304	26	68.3	45.3	102.7	56.6	65.7	2.2	0.4	0.3	122.8	1.87

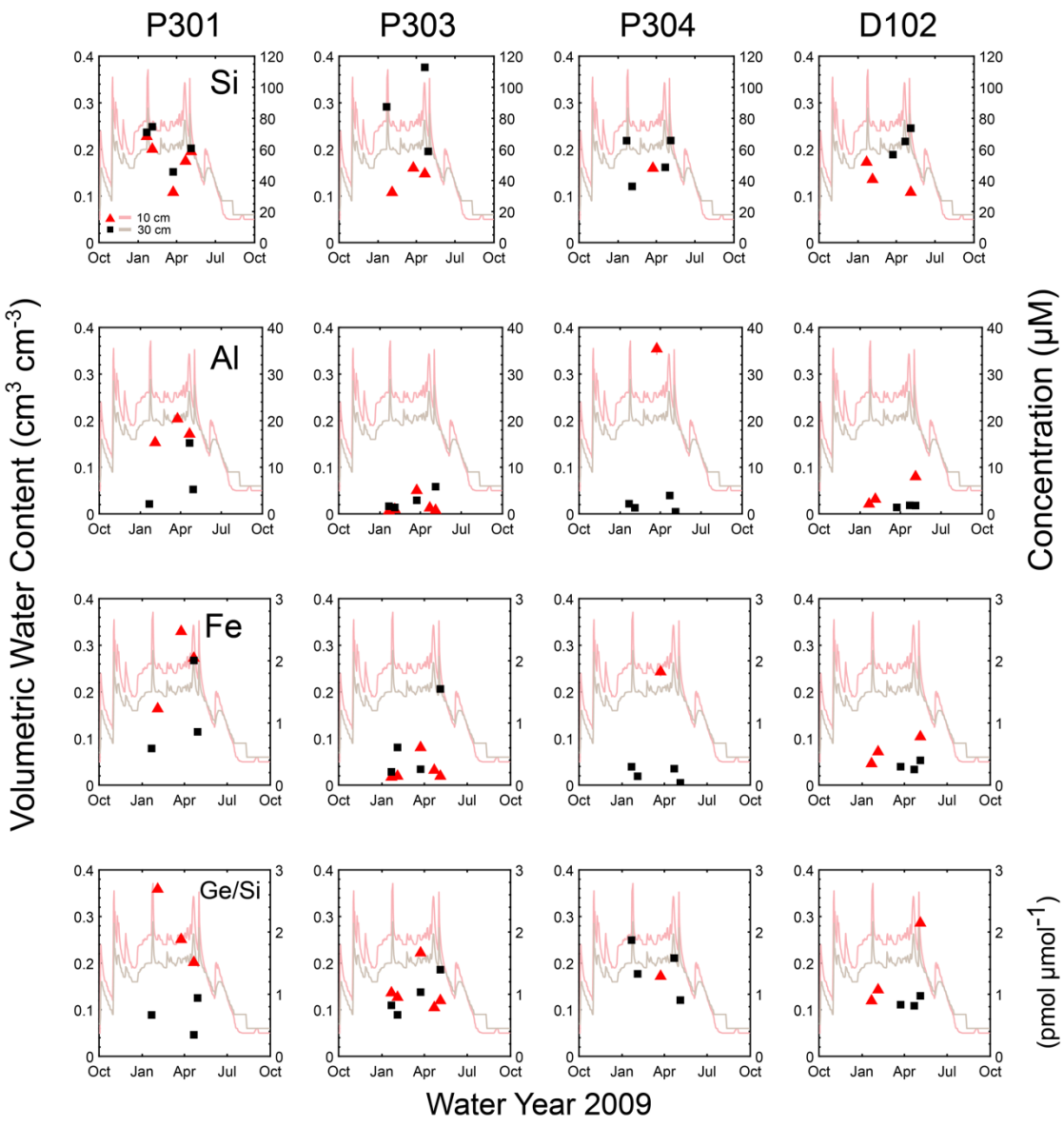

Figure 1.9: Providence Creek soil pore water chemistry. Soil pore water chemistry for 10 (red triangles) and 30 (black squares) cm depths. Soil volumetric water content is shown for 10 (grey) and 30 (light red) cm depths.

depth are higher than in shallow soil. In P303 and P304, there is no clear pattern between the shallow to deeper soil water. Peaks in Si concentration happen for the deeper 30 cm during periods of increased infiltration and higher VWC. In D102, we observe decreasing Si concentrations while at 30 cm depth samples gradually increase until the end of the snowmelt season.

The similar soil water chemistry between the 10 to 30 cm soil depths is likely a consequence of the uniform soil mineralogy. Throughout the catchments, soil textural variations are minor and the clay size fraction ranges between 0.06 and 0.11 (Bales et al., 2011). Additionally, we observed minor variations in SiO_2 and Ge/Si along a 11-meter soil core in P301 (Table 1.4). Therefore, the pore water chemistry at both depths reflects similar fluid-rock interactions. Based on the elevated aluminum and Ge/Si, it is very clear that soil water is interacting with secondary aluminosilicate clays. Soil pore water was not analyzed for the upper elevation Bull Creek Catchments (B201-204 and T003). However, the P301 catchment has similar elevation to Bull Creek (Table 1.1). Therefore, soil pore water from P301 can be used as a proxy for soil water at these upper elevation catchments.

1.5 Discussion

1.5.1 End-member mixing space

The Na, Mg, Ca and Si mixing figures of Providence Creek demonstrate a two end-member mixing system (Figure 1.10). Stream samples form a simple two end-member mixing line with snow. The two exceptions are the Mg-Ca and Na-Si mixing patterns. For Mg-Ca, soil water is super imposed onto stream water and form a mixing

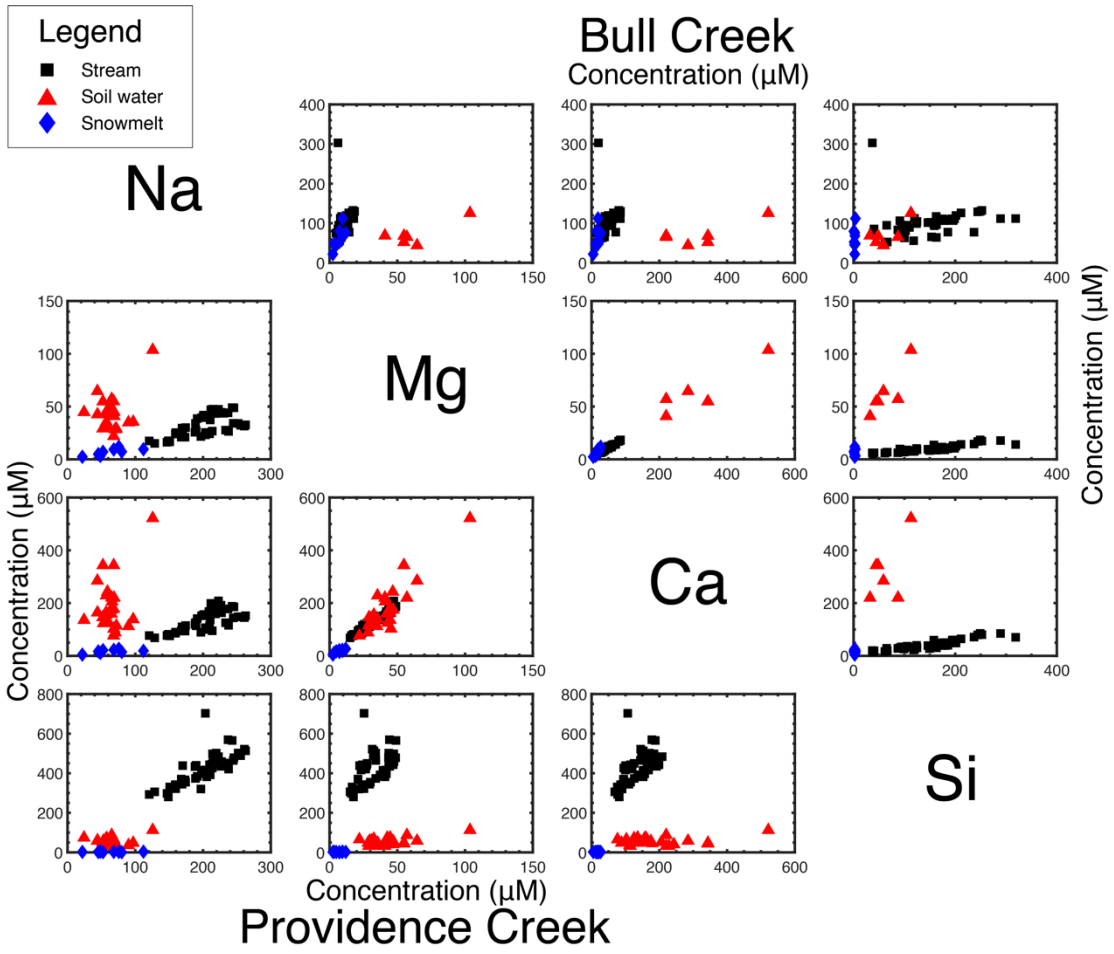

Figure 1.10: End-member mixing spaces in Providence and Bull Creek. Mixing space for stream water (black squares), soil water (red triangles) and snowmelt (blue diamonds).

line with snow. Calcareous inputs from Asian or central valley dust deposition can be significant sources of Ca and Mg to soils in this system (Aciego et al., 2017; Lawrence et al., 2013). Therefore, in the case of Mg-Ca mixing, there may be a greater influence of carbonate dissolution in soil water to stream flow. In the case of Na-Si, soil water and snow coincide as dilute end-members in the two-component mixing line with stream water. Soil water may be reflecting significant contribution from infiltrating snowmelt. Therefore, along this mixing line the Na-Si concentrated end-member is represented by weathering of feldspars in groundwater. The dilute end-member may be represented by snowmelt runoff.

In Bull Creek, we observe similar two end-member mixing between snow and stream water for most solutes (Figure 1.10). However, more dilute concentrations for Na, Mg and Ca in stream water result in soil water samples overlapping with snow samples. As observed in Providence, the Mg-Ca mixing space displays mixing between soil water (higher Mg and Ca) and snowmelt/stream water (lower Mg and Ca). Once again, the enrichment of Mg and Ca in the soil may be caused by dust deposition outpacing supply of these nutrients by bedrock weathering. The Na-Si mixing space in Bull Creek also forms a two-component mixing array. As we observed in Providence Creek, snow, soil water and stream samples fall along a two-component mixing line. Unlike Providence, low concentrations in Bull Creek streams overlap with soil water. In Bull Creek, Ge/Si was significantly correlated with discharge. This suggests the activation of a soil hydrologic pathway during increased discharge. The Na-Si mixing space corroborates this interpretation since some stream water samples overlap with soil water. For Na and Si, it is evident that the two end-member mixing is between

groundwater and snowmelt runoff or soil water. The two most conservative solutes Na and Si are clearly not mixing with soil pore water in Providence Creek. Instead, snow appears to be the dilute end-member in this two-component mixing. In Bull Creek, mixing relationships appear to be between groundwater and soil water. As for the mixing space between Mg and Ca, dust deposition might be a significant contributor.

1.5.2 Weathering processes

Germanium-silicon ratios in stream water in KREW can give us some insight into the sources of Si to the stream. Stream water Ge/Si is within a very narrow range of 0.02 and 0.12 pmol μmol^{-1} in Providence Creek. The most surprising result is the very low ratios observed even during high discharge (Figure 1.4). The global average clean river Ge/Si is 0.5 pmol μmol^{-1} (Baronas et al., 2016; Froelich et al., 1992; Kurtz et al., 2002). This value is an integration of the weathering of multiple mineral phases. This would include phases like kaolinite and hornblende that would increase Ge/Si ratios in stream water. Instead, in Providence Creek we may be seeing the dominance of feldspar weathering that can yield significantly lower Ge/Si ratios.

Mineral saturation indexes for stream water, soil water and snowmelt were calculated with Geochemist's Workbench (GWB Version 12) using the LLNL thermodynamic database;

$$SI = log(Q/K) \quad (1)$$

where Q represents the activity product and K the equilibrium constant. Stream samples in KREW are undersaturated with respect to albite, amorphous silica, anorthite and saturated with respect to secondary minerals (i.e. gibbsite, illite and kaolinite) and quartz

(Appendix 3 & 4). Additionally, K^+/H^+ to SiO_2 mineral stability diagram shows that stream water in KREW is in equilibrium with kaolinite (Figure 1.11). Therefore, the dominant weathering reaction in this system should be feldspar weathering to kaolinite.

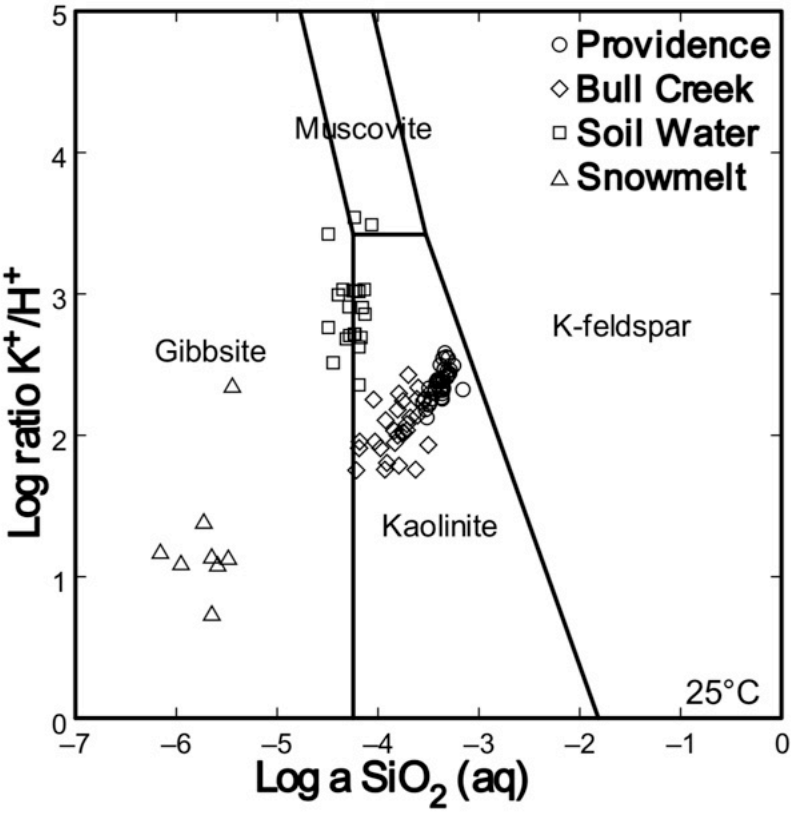

Figure 1.11: Mineral stability diagram for KREW samples. KREW stream water samples (circles and diamonds), soil pore water (squares) and snowmelt (triangles).

This would corroborate our observation that Providence has a significantly lower Ge/Si than the global average ratio of 0.5 pmol μmol^{-1} observed in other catchments. Stream water ratios less than 0.1 pmol μmol^{-1} would suggest the dissolution of quartz or biogenic opal (phytoliths) (Bernstein, 1985; Cornelis et al., 2010a; Derry et al., 2005). Quartz dissolution is not occurring because the mineral saturation index in stream water are saturated with respect to this mineral (Appendix 3). The role of phytoliths as a

dominant source of SiO_2 can also be discounted because mixed-conifer forests are not major biogenic Si accumulators (Bartoli, 1983; Cornelis et al., 2010b; Gerard et al., 2008; Markewitz and Richter, 1998). Nonetheless, these landscapes can still contain phytoliths in shallow soils concentrated by needles of mixed-conifers (Bartoli, 1983; Cornelis et al., 2010b). However, we can be confident phytoliths are not a major component of the Si mass balance. Soil pore water samples collected at 10 and 30 cm depth indicate undersaturation with respect to amorphous silica but saturation with respect to kaolinite (Appendix 5). Additionally, the mineral stability diagram shows that soil pore waters cluster along the gibbsite-kaolinite boundary (Figure 1.11). This indicates that for some soil water samples, dilute and acidic infiltrating snowmelt lowered the H_4SiO_4 saturation promoting kaolinite and feldspar dissolution.

The very low Ge/Si ratios in stream water at Providence Creek suggests higher Ge retention in secondary clays or the effective Si removal from intense leaching conditions. Consider the following Ge/Si mass balance relationship;

(2) $$1 = f_{gw} + f_{kaol}$$

(3) $$Ge/Si_{feldspar} = Ge/Si_{gw} \cdot f_{gw} + Ge/Si_{kaol} \cdot f_{kaol}$$

where f_{gw} represents fraction of groundwater and f_{kaol} fraction of kaolinite during incongruent weathering of primary minerals. Equation (3) shows the Ge/Si mass balance where Ge/Si_{gw} and Ge/Si_{kaol} are derived from the same source and f_{gw} represent the fraction of Si exported by groundwater during incongruent weathering. For Providence Creek, we will assume baseflow has the Ge/Si composition of groundwater. Consider an average $Ge/Si_{feldspar}$ of 2.1 (± 0.6), Ge/Si_{kaol} of 5.4 (± 0.06)

and average Providence Creek Ge/Si_{gw} of 0.08 (± 0.02) pmol μmol^{-1} (Aguirre et al., 2017; Evans and Derry, 2002; Kurtz et al., 2002; Lugolobi et al., 2010). By rearranging equations (2) and (3) we can solve for f_{kaol} using a Monte Carlo simulation with 5,000 uniformly distributed random trials;

(4) $$f_{kaol} = \frac{Ge/Si_{feld} - Ge/Si_{gw}}{Ge/Si_{kaol} - Ge/Si_{gw}}$$

the f_{kaol} yields 0.39 (± 0.07) implying that 61% of SiO_2 is available for groundwater export. The 39% of silicon sequestered in kaolinite is slightly higher than that calculated for the Upper Gordon Gulch catchment in Boulder Creek CZO (Aguirre et al., 2017). Equation (4) demonstrates that f_{kaol} is most sensitive to the Ge/Si composition defined for this system. The relative standard deviation (RSD) of kaolinite from our compiled Ge/Si composition is 1.1%. The RSD for feldspar is much higher at 28.6%. Therefore, the highest uncertainty in our mass balance calculation is dependent on the Ge/Si composition of feldspar. This is unfortunate given the greater challenge of separating feldspar grains from rock samples than clays using simple dispersion/flocculation methods. Nonetheless, this mass balance calculation indicates that Si export at KREW agrees with the stoichiometry of the model feldspar to kaolinite weathering reaction;

(5) $$2KSi_3AlO_8 + 2H^+ + 9H_2O \rightarrow Si_2Al_2O_5(OH)_4 + 2K^+ + 4Si(OH)_4$$

Silicon stoichiometry = 3:1:2

Feldspar:kaolinite:dissolved Si

Therefore, these lower ratios during baseflow can still be explained by traditional incongruent weathering. In order to understand the partitioning of Ge/Si between

mineral phases, consider the following partitioning factor presented by Froelich et al. (1992);

(6) $$K_W = \frac{(Ge/Si)_{clay}}{(Ge/Si)_{bedrock}}$$

Assuming the Ge/Si ratio of bedrock is equivalent to that of feldspar, we can take the Si stoichiometry derived above and use a modified version of equation (3) to obtain the following;

(7) $$3(Ge/Si)_{feld} = (Ge/Si)_{clay} + 2(Ge/Si)_{gw}$$

By rearranging equation (6) and substituting for $(Ge/Si)_{clay}$ we obtain the following relationship;

(8) $$K_W = 3 - \frac{2(Ge/Si)_{gw}}{(Ge/Si)_{feld}}$$

Notice that our maximum K_w can be 3.0 if our system has a complete Ge incorporation into the secondary phase and $(Ge/Si)_{gw} = 0$. If we take the $(Ge/Si)_{gw} = 0.06$ pmol μmol^{-1} used before and $(Ge/Si)_{feld} = 2.1$ pmol μmol^{-1}, our K_W equals 2.94. We obtain almost complete partitioning of Ge into the secondary phase responsible for the very low Ge/Si ratios in Providence Creek. This indicates a possible long fluid residence time which can exceed the time required for the water to reach chemical equilibrium with the precipitating secondary phase. This process has been argued as a dominant control on the chemostatic C-Q relationships observed across catchments (Maher, 2011). Groundwater with a residence time of up to 28 years has been documented in some catchments in the Sierra Nevada (Rademacher et al., 2005). With the significant groundwater storage caused by high porosity and thick regolith, there may be a significant influence of old groundwater to the stream chemistry of Providence

Creek.

Murnane and Stallard (1990) proposed the relationship of Ge/Si ratio to 1/Si as a representation of the weathering intensity of a system (Figure 1.12). Our data shows an extreme weathering limited regime (high [Si] and low [Ge/Si]) for Providence Creek. In Bull Creek, there is a greater distribution of observations along the two end-member mixing line where most samples lie close to the weathering limited regime. However, there are multiple observations plotting closer to a lower [Si] and high [Ge/Si] transport limited regime. The y-intercept of -0.02 suggests an end-member Ge/Si composition of zero or complete Ge incorporation into secondary minerals ($K_W = 0$). The slope of 33.2 in our linear fit is lower than that reported by catchments from diverse lithologies and climates (Froelich et al., 1992). This lower slope is once again an indicator that incongruent weathering of feldspars is by far the dominant weathering reaction in this system. However, there is a difference in response to snowmelt infiltration between the lower and upper elevation sites. While Providence Creek has chemostatic Si-Q exponents sustained by constant groundwater inputs to the stream, Bull Creek experiences greater dilution (slopes 0.21 to -0.46). This dilution behavior can be caused by intense leaching conditions from dilute snowmelt that can lead to significant desilication (Dahlgren et al., 1997). Inputs of Si dilute snowmelt may be promoting kaolinite weathering in the Bull Creek soils as observed in the soil water samples in the mineral stability diagram (Figure 1.11). Recall that Bull Creek is within the advancement of Pleistocene glaciers. The scouring of the catchment surface has resulted in a shallower contact zone with fresh bedrock than Providence Creek. This intense leaching environment coupled with lower groundwater storage would lead to a shorter

water residence time.

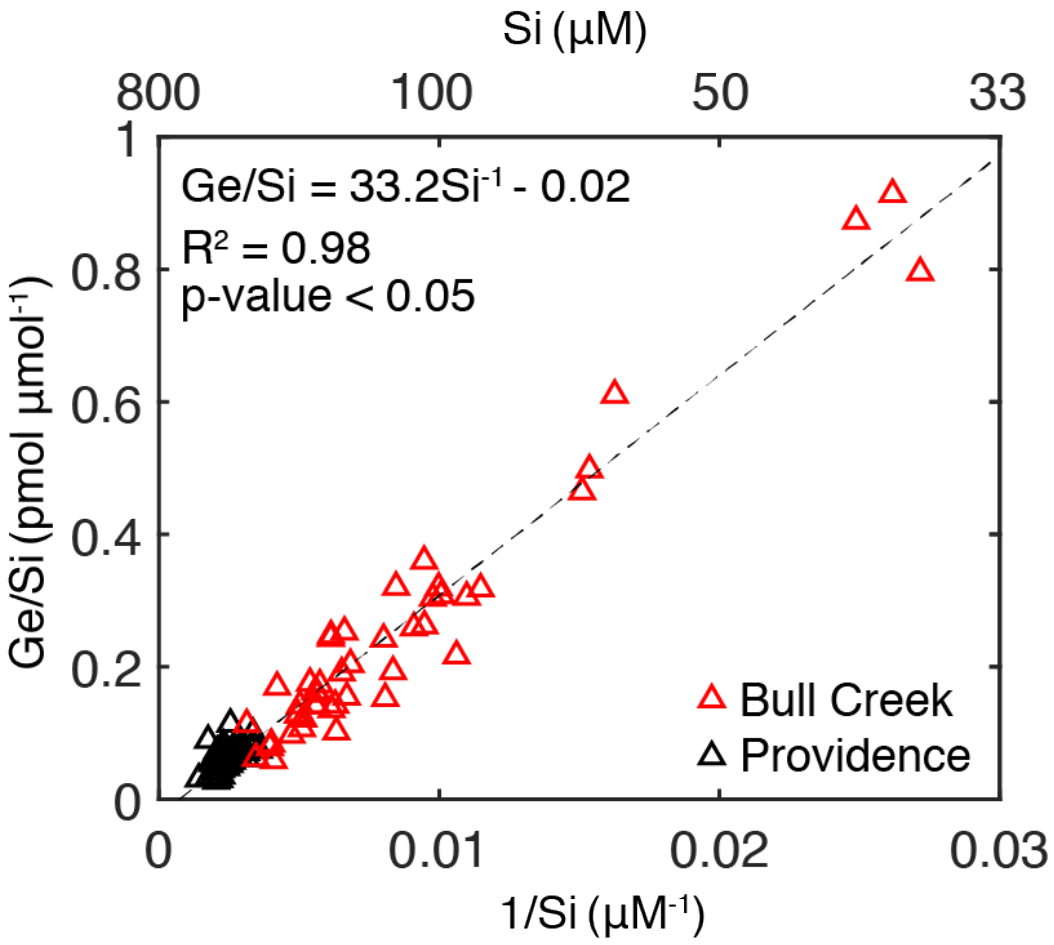

Figure 1.12: Two end-member mixing space of 1/Si and Ge/Si for KREW. Observations include Providence (black triangles) and Bull Creek (red triangles).

Moreover, we have not considered the seasonal soil moisture variation caused by changes in ET. This can have significant effects on the clay mineralogy of the system. Strong leaching conditions result in the loss of base cations which favor the precipitation of kaolinite (Chadwick and Chorover, 2001). However, smectite can form in dry environments and can include more soluble elements (i.e. alkali metals) (Maher, 2011). There is still an insufficient understanding of the role these clay forming processes have on the partitioning of Ge into different mineral phases.

1.6 Conclusion

The Kings River Experimental Watershed provides a unique setting where we can test hypothesis of water transport and solute generation. We have shown that Ge/Si in stream water of Providence Creek ranges between 0.03 and 0.12 pmol μmol^{-1} suggesting strong incongruent weathering of feldspars to form kaolinite. Soil pore water has higher ratios between 0.67 and 2.69 pmol μmol^{-1} indicating that kaolinite does break down to release Si. Data on major elements (Si, Na, K, Ca and Mg) can be well explained by two component mixing between snowmelt and groundwater, supporting Liu et al. (2013) that soil pore water is not an important end-member in Providence Creek. Seasonally, silicon concentration experience dilution during the snowmelt period as a result of snowmelt runoff. However, the chemostatic Si-Q (b = -0.08 to -0.12) relationships suggests that groundwater is a dominant contributor to stream flow despite increased snowmelt runoff. The Ge/Si mass balance supports this conclusion because during high discharge, Ge/Si ratios do not increase above 0.12 pmol μmol^{-1}. Contribution to stream flow from soil water would shift stream water ratios towards the soil pore water Ge/Si value. In fact, Ge/Si-discharge relationship is weak and variations in Ge/Si ratios do not correspond to changes in discharge.

The modeled partition coefficient (K_W) for Ge/Si in the Providence Creek system show near complete Ge incorporation into the secondary minerals. This process is likely associated with long fluid residence times that permit approach to equilibrium. The thick regolith at Providence Creek increased groundwater storage which is largely responsible for stream flow at this site. In Ge/Si to 1/Si mixing space, Providence Creek lies on the extreme weathering limited regime where high dissolved Si concentrations are caused

by incongruent weathering of feldspars.

The Bull Creek catchment was compared to Providence Creek where the effects of precipitation and geologic history could be assessed on the Si dynamics of this system. Bull Creek has less developed soils and a shallower contact to un-weathered bedrock (Johnson et al., 2011). This is in part due to lower temperatures at higher elevation and Pleistocene glaciation that may have scoured the upper mantle of soil. These differences had profound consequences on the C-Q relationships and Si dynamics at Bull Creek. The seasonal variations in Si concentrations show that there is dilution during the snowmelt period. Most strikingly, the Si-Q relationships for B201-204 are not chemostatic, with power law exponents of -0.21 to -0.46 indicating dilution behavior. These samples show increased Ge/Si and suggest that new hydrologic pathways are activated during snowmelt and must contribute significantly to stream flow for Si-Q patterns to exhibit dilution. At Bull Creek, Ge/Si ratios provide the most convincing evidence that with increasing discharge soil pore water is an end-member. Ratios are significantly correlated with discharge and increase up to 0.91 pmol μmol^{-1}. Stream water Si concentrations decrease because the system is shifting to weathering of secondary minerals with higher Ge/Si ratios. The mineral stability at Bull Creek shows a system at the interface of kaolinite/gibbsite while snow is in equilibrium with gibbsite. The significant inputs of dilute Si snowmelt into the system leads to undersaturated conditions with respect to Si and promotes kaolinite weathering. The smaller groundwater storage capacity at Bull Creek should also lead to shorter fluid residence times and conditions far from chemical equilibrium. At this site, we observe a greater influence from our transport limited regime in the Ge/Si to 1/Si mixing space. The

limitation at Bull Creek is the kinetics of weathering reactions coupled with rapid transport processes.

The Kings River Experimental Watershed has provided a unique setting where weathering and transport processes can be explored among catchments with different geologic history. The geochemical tracer of Ge/Si has been a useful tool to elucidate the different weathering mechanisms in each watershed and has provided insight into its hydrologic pathways. Moreover, it has been shown that precipitation patterns and rain/snow distribution is a more significant factor influencing CZ processes than total precipitation alone. Despite identical bedrock composition, the slight temperature differences and glacial history have had profound effects on subsurface groundwater storage and hydrology. In future studies, workers must consider these effects on watersheds when doing cross-site comparisons. Even among catchments with similar bedrock composition, climate and vegetation; precipitation patterns and geologic history can have profound effects on soils and CZ structure that can impact stream chemistry.

References

Aciego, S.M., Riebe, C.S., Hart, S.C., Blakowski, M.A., Carey, C.J., Aarons, S.M., Dove, N.C., Botthoff, J.K., Sims, K.W.W. and Aronson, E.L. (2017) Dust outpaces bedrock in nutrient supply to montane forest ecosystems. Nature Communications 8.

Aguirre, A.A., Derry, L.A., Mills, T.J. and Anderson, S.P. (2017) Colloidal transport in the Gordon Gulch catchment of the Boulder Creek CZO and its effect on C-Q relationships for silicon. Water Resources Research 53, 2368-2383.

Allen, B.L. and Hajek, B.F. (1989) Mineral Occurrence in Soil Environments, in: Dixon, J.B., Weed, S.B. (Eds.), Minerals in Soil Environments. Soil Science Society of America, Madison, WI, pp. 199-278.

Anderson, S.P., Blum, A.E., Hinckley, E.S., Lee, J., Gilbert, R., Trotta, J. and Dethier, D. (2010) Slope aspect and weathering in the Colorado Front Range. Geochimica Et Cosmochimica Acta 74, A21-A21.

Bales, R., Stacy, E., Safeeq, M., Meng, X.D., Meadows, M., Oroza, C., Conklin, M., Glaser, S. and Wagenbrenner, J. (2018) Spatially distributed water-balance and meteorological data from the rain-snow transition, southern Sierra Nevada, California. Earth System Science Data 10, 1795-1805.

Bales, R.C., Hopmans, J.W., O'Geen, A.T., Meadows, M., Hartsough, P.C., Kirchner, P., Hunsaker, C.T. and Beaudette, D. (2011) Soil Moisture Response to Snowmelt and Rainfall in a Sierra Nevada Mixed-Conifer Forest. Vadose Zone Journal 10, 786-799.

Baronas, J.J., Hammond, D.E., Berelson, W.M., McManus, J. and Severmann, S. (2016) Germanium-silicon fractionation in a river-influenced continental margin: The Northern Gulf of Mexico. Geochimica Et Cosmochimica Acta 178, 124-142.

Bartoli, F. (1983) The Biogeochemical Cycle of Silicon in 2 Temperate Forest Ecosystems. Ecol Bull, 469-476.

Bateman, P.C. (1992) Plutonism in the central part of the Sierra Nevada batholith, California.

Bernstein, L.R. (1985) Germanium Geochemistry and Mineralogy. Geochimica Et Cosmochimica Acta 49, 2409-2422.

Chadwick, O.A. and Chorover, J. (2001) The chemistry of pedogenic thresholds. Geoderma 100, 321-353.

Clow, D.W. and Mast, M.A. (2010) Mechanisms for chemostatic behavior in catchments: Implications for CO2 consumption by mineral weathering. Chemical Geology 269, 40-51.

Conley, D.J. (2002) Terrestrial ecosystems and the global biogeochemical silica cycle. Global Biogeochemical Cycles 16.

Cornelis, J.T., Delvaux, B., Cardinal, D., Andre, L., Ranger, J. and Opfergelt, S. (2010a) Tracing mechanisms controlling the release of dissolved silicon in forest soil solutions using Si isotopes and Ge/Si ratios. Geochimica Et Cosmochimica Acta 74, 3913-3924.

Cornelis, J.T., Ranger, J., Iserentant, A. and Delvaux, B. (2010b) Tree species impact the terrestrial cycle of silicon through various uptakes. Biogeochemistry 97, 231-245.

Dahlgren, R.A., Boettinger, J.L., Huntington, G.L. and Amundson, R.G. (1997) Soil development along an elevational transect in the western Sierra Nevada, California. Geoderma 78, 207-236.

Derry, L.A., Kurtz, A.C., Ziegler, K. and Chadwick, O.A. (2005) Biological control of terrestrial silica cycling and export fluxes to watersheds. Nature 433, 728-731.

Dixon, J.L., Heimsath, A.M. and Amundson, R. (2009a) The critical role of climate and saprolite weathering in landscape evolution. Earth Surface Processes and Landforms 34, 1507-1521.

Dixon, J.L., Heimsath, A.M., Kaste, J. and Amundson, R. (2009b) Climate-driven processes of hillslope weathering. Geology 37, 975-978.

Dolanc, C.R. and Hunsaker, C.T. (2017) The transition from riparian to upland forest plant communities on headwater streams in the southern Sierra Nevada, California, United States. Journal of the Torrey Botanical Society 144, 280-295.

Evans, M.J. and Derry, L.A. (2002) Quartz control of high germanium/silicon ratios in geothermal waters. Geology 30, 1019-1022.

Froelich, P.N., Blanc, V., Mortlock, R.A., Chillrud, S.N., Dunstan, W., Udomkit, A. and Peng, T.H. (1992) River fluxes of dissolved silica to the ocean were higher during glacials: Ge/Si in diatoms, rivers, and oceans. Paleoceanography 7, 739-767.

Gerard, F., Mayer, K.U., Hodson, M.J. and Ranger, J. (2008) Modelling the biogeochemical cycle of silicon in soils: Application to a temperate forest ecosystem. Geochimica Et Cosmochimica Acta 72, 741-758.

Giger, D.R.a.G.J.S. (1993) Soil Survey of Sierra National Forest, in: USDA-SCS (Ed.). U.S. Gov. Print. Off., Washington, DC.

Godsey, S.E., Kirchner, J.W. and Clow, D.W. (2009) Concentration-discharge relationships reflect chemostatic characteristics of US catchments. Hydrological Processes 23, 1844-1864.

Goulden, M.L., Anderson, R.G., Bales, R.C., Kelly, A.E., Meadows, M. and Winston, G.C. (2012) Evapotranspiration along an elevation gradient in California's Sierra Nevada. Journal of Geophysical Research-Biogeosciences 117.

Hahm, W.J., Riebe, C.S., Lukens, C.E. and Araki, S. (2014) Bedrock composition regulates mountain ecosystems and landscape evolution. Proceedings of the National Academy of Sciences of the United States of America 111, 3338-3343.

Herndon, E.M., Dere, A.L., Sullivan, P.L., Norris, D., Reynolds, B. and Brantley, S.L. (2015) Landscape heterogeneity drives contrasting concentration-discharge relationships in shale headwater catchments. Hydrology and Earth System Sciences 19, 3333-3347.

Heumann, K.G. (1988) Isotope Dilution Mass Spectrometry, in: F. Adams, R.G.a.R.V.G. (Ed.), Inorganic Mass Spectrometry. John Wiley & Sons, New York, NY.

Holbrook, W.S., Riebe, C.S., Elwaseif, M., Hayes, J.L., Basler-Reeder, K., Harry, D.L., Malazian, A., Dosseto, A., Hartsough, P.C. and Hopmans, J.W. (2014) Geophysical constraints on deep weathering and water storage potential in the Southern Sierra Critical Zone Observatory. Earth Surface Processes and Landforms 39, 366-380.

Hooper, R.P. (2003) Diagnostic tools for mixing models of stream water chemistry. Water Resources Research 39.

Hooper, R.P. and Shoemaker, C.A. (1986) A Comparison of Chemical and Isotopic Hydrograph Separation. Water Resources Research 22, 1444-1454.

Hunsaker, C.T. and Johnson, D.W. (2017) Concentration-discharge relationships in headwater streams of the Sierra Nevada, California. Water Resources Research 53, 7869-7884.

Hunsaker, C.T., Whitaker, T.W. and Bales, R.C. (2012) Snowmelt Runoff and Water Yield Along Elevation and Temperature Gradients in California's Southern Sierra Nevada. J Am Water Resour As 48, 667-678.

Johnson, D.W., Hunsaker, C.T., Glass, D.W., Rau, B.M. and Roath, B.A. (2011) Carbon and nutrient contents in soils from the Kings River Experimental Watersheds, Sierra Nevada Mountains, California. Geoderma 160, 490-502.

Kennedy, V.C., Kendall, C., Zellweger, G.W., Wyerman, T.A. and Avanzino, R.J. (1986) Determination of the components of stormflow using water chemistry and environmental isotopes, Mattole River basin, California. Journal of Hydrology 84, 107-140.

Kurtz, A.C., Derry, L.A. and Chadwick, O.A. (2002) Germanium-silicon fractionation in the weathering environment. Geochimica Et Cosmochimica Acta 66, 1525-1537.

Kurtz, A.C., Lugolobi, F. and Salvucci, G. (2011) Germanium-silicon as a flow path tracer: Application to the Rio Icacos watershed. Water Resources Research 47.

Lawrence, C.R., Reynolds, R.L., Ketterer, M.E. and Neff, J.C. (2013) Aeolian controls of soil geochemistry and weathering fluxes in high-elevation ecosystems of the Rocky Mountains, Colorado. Geochimica Et Cosmochimica Acta 107, 27-46.

Liu, F.J., Conklin, M.H. and Shaw, G.D. (2017) Insights into hydrologic and hydrochemical processes based on concentration-discharge and end-member mixing analyses in the mid-Merced River Basin, Sierra Nevada, California. Water Resources Research 53, 832-850.

Liu, F.J., Hunsaker, C. and Bales, R.C. (2013) Controls of streamflow generation in small catchments across the snow-rain transition in the Southern Sierra Nevada, California. Hydrological Processes 27, 1959-1972.

Lugolobi, F., Kurtz, A.C. and Derry, L.A. (2010) Germanium-silicon fractionation in a tropical, granitic weathering environment. Geochimica Et Cosmochimica Acta 74, 1294-1308.

Maher, K. (2011) The role of fluid residence time and topographic scales in determining chemical fluxes from landscapes. Earth and Planetary Science Letters 312, 48-58.

Markewitz, D. and Richter, D.D. (1998) The bio in aluminum and silicon geochemistry. Biogeochemistry 42, 235-252.

Mortlock, R.A. and Froelich, P.N. (1996) Determination of germanium by isotope dilution hydride generation inductively coupled plasma mass spectrometry. Analytica Chimica Acta 332, 277-284.

Rademacher, L.K., Clark, J.F., Clow, D.W. and Hudson, G.B. (2005) Old groundwater influence on stream hydrochemistry and catchment response times in a small Sierra Nevada catchment: Sagehen Creek, California. Water Resources Research 41.

Safeeq, M. and Hunsaker, C.T. (2016) Characterizing Runoff and Water Yield for Headwater Catchments in the Southern Sierra Nevada. J Am Water Resour As 52, 1327-1346.

Shanley, J.B., McDowell, W.H. and Stallard, R.F. (2011) Long-term patterns and short-term dynamics of stream solutes and suspended sediment in a rapidly weathering tropical watershed. Water Resources Research 47.

Stallard, R.F. and Murphy, S.F. (2014) A Unified Assessment of Hydrologic and Biogeochemical Responses in Research Watersheds in Eastern Puerto Rico Using Runoff-Concentration Relations. Aquatic Geochemistry 20, 115-139.

Torres, M.A., West, A.J. and Clark, K.E. (2015) Geomorphic regime modulates hydrologic control of chemical weathering in the Andes-Amazon. Geochimica Et Cosmochimica Acta 166, 105-128.

Trostle, K.D., Runyon, J.R., Pohlmann, M.A., Redfield, S.E., Pelletier, J., McIntosh, J. and Chorover, J. (2016) Colloids and organic matter complexation control trace metal concentration-discharge relationships in Marshall Gulch stream waters. Water Resources Research 52, 7931-7944.

Wymore, A.S., Brereton, R.L., Ibarra, D.E., Maher, K. and McDowell, W.H. (2017) Critical zone structure controls concentration-discharge relationships and solute

generation in forested tropical montane watersheds. Water Resources Research 53, 6279-6295.

CHAPTER TWO[1]:

COLLOIDAL TRANSPORT IN THE GORDON GULCH CATCHMENT OF THE BOULDER CREEK CZO AND ITS EFFECT ON C-Q RELATIONSHIPS FOR SILICON

Abstract

The near constant Si concentration under varying discharge observed in Gordon Gulch of the Boulder Critical Zone Observatory (CZO) indicates that the silica fluxes are strongly controlled by discharge. To identify the mechanisms supplying increased Si at high discharge (Q) we examine Si-Al-Fe-Ge in soils, streams and ground waters. We identify bedrock weathering in groundwater and colloidal transport as the two end-members that supply Si to the system. During baseflow, stream flow is derived from groundwater, and weathering of feldspar is the main source of Si with a Ge/Si ratio 0.2-0.5 μmol mol^{-1} and low dissolved Al and Fe. The groundwater data are consistent with incongruent weathering of feldspar as the main source of dissolved Si. As discharge increases, Si-Al-Fe bearing colloids are mobilized, and the Ge/Si ratio of the stream rises to 3.0 μmol mol^{-1}. Mineralogical analysis using XRD identified Al-Si phases including kaolinite, illite and quartz in the colloidal size fraction (< 0.45 μm). The Ge/Si ratio of stream and soil colloids ≈ 3.8 μmol mol^{-1}. The mechanism of colloidal transport with increasing discharge can account for the concentration-discharge (C-Q) patterns of

[1]Aguirre, A.A., Derry, L.A., Mills, T.J. and Anderson, S.P. (2017) Colloidal transport in the Gordon Gulch catchment of the Boulder Creek CZO and its effect on C-Q relationships for silicon. Water Resources Research 53, 2368-2383.

Si, Al and Fe with near-zero or positive power law slopes observed in the Gordon Gulch catchment. Anomalously high Ge/Si ratios also identified a third end-member resulting from coal fly ash deposition during the winter and spring. Wind trajectories during 2012, correlation between Ge/Si and SO_4^{2-}, and comparison to atmospheric deposition data imply contamination from nearby coal fired power plant operations.

2.1 Introduction

Changes in the concentration and flux of stream solutes as a function of discharge contain information about water flow paths, biogeochemical reactions, and transport times in the watershed (Buttle and Peters, 1997; Chanat et al., 2002; Evans and Davies, 1998; Hornberger et al., 2001). It is common for solute concentrations to vary less widely than stream discharge, indicating that elemental fluxes are most strongly controlled by discharge variation. Godsey et al. (2009) proposed that concentration-discharge (C-Q) data in many catchments could be fit to a simple power law of the form $C = aQ^b$, where a and b are constants. The case of $b = -1$ corresponds to perfect dilution behavior, while in the case of $b = 0$ C does not vary with Q, behavior they termed "chemostatic." Given that small catchments in particular can show large variations in discharge, chemostatic behavior implies equally large changes in the flux of solutes that exhibit this pattern. An important question raised by this scenario is what are the sources of the increased solute flux when discharge increases? What are the reactions as well as flow paths that provide large increase in solute flux on the time scale of a watershed response to a rain event? Here we focus on solutes primarily derived from mineral weathering and use elemental ratios of both solute and solid phases to

characterize the sources of solutes to the upper Gordon Gulch catchment of the Boulder Creek Critical Zone Observatory (CZO) located in the Colorado Front Range.

Silicon has been of interest in C-Q studies because it is primarily derived from rock weathering and has minor impacts from atmospheric deposition (Kennedy et al., 1986; Scanlon et al., 2001). Silicon is the most abundant element in the continental crust after oxygen, and weathering processes that release Si to solution are coupled to the release of mineral nutrients, soil formation, and the regulation of atmospheric CO_2 (Berner et al., 1983). Watershed silica fluxes can be impacted by biocycling, either by consumption by diatoms or by uptake by vascular plants (Carey and Fulweiler, 2012; Derry et al., 2005). If biomass storage in a catchment is small or at steady state, variations in catchment silica fluxes must dominantly reflect processes that control the generation and transport of silica from mineral sources. One class of models commonly used to analyze C-Q relationships are end-member mixing models. These models represent solute concentrations as a linear mixture of water from various reservoirs whose proportions can change through a hydrographic event (Hooper, 2003; Kurtz et al., 2011). End-member mixing models generally do not require knowledge of the reactions that introduce dissolved silica into those reservoirs. Variations in silica fluxes can be caused by changes in mechanisms that produce dissolved silica or emergence of new flow paths that sample different reservoirs and reaction zones. Recent work in the Gordon Gulch catchment at the Boulder Creek CZO has documented "chemostatic" behavior for Si in this small montane catchment. An intriguing observation about silica chemistry from Gordon Gulch is the recognition of significant colloidal mobilization of Si in stream water (Mills et al., 2017). In the following study, a geochemical perspective

is used to understand the sources of silicon to the stream and how that changes in response to variations in discharge

The use of geochemical tracers can provide considerable insight into solute sources and pathways. Germanium-silicon ratios can be an effective tool for tracing sources of silica at the catchment scale (Derry et al., 2005; Kurtz et al., 2002; Kurtz et al., 2011; Lugolobi et al., 2010). Germanium has geochemical properties similar to silicon (both group 14 elements). With an average crustal concentration near 1.4 ppm, germanium can form an ideal solid solution with Si in the tetrahedral sites of common silicate minerals (Capobianco and Navrotsky, 1982; Evans and Derry, 2002; Martin et al., 1996). In stream water at pH < 8 germanium exists as germanic acid ($Ge(OH)_4$), analogous to silicic acid ($Si(OH)_4$) (Pokrovski and Schott, 1998). Germanium serves as a generally conservative tracer for silicon in the aqueous environment (Evans et al., 2004). The controls on Ge substitution are not completely understood but empirical data indicate that it is partly dependent on mineral structure, with Ge/Si ratios (O)10^{-6} mol/mol and generally increasing from quartz < feldspars < sheet silicates (Evans and Derry, 2002; Kurtz et al., 2002; Lugolobi et al., 2010). In the near surface environment Ge fractionates relative to Si in predictable ways, with Ge/Si an effective tracer of silica sources and pathways (Froelich et al., 1992). Of particular interest here is that during incongruent weathering of primary minerals like feldspars Ge/Si ratios are fractionated by precipitation of Ge-enriched secondary clays, leaving low Ge/Si in the residual solute phase (Kurtz et al., 2002). Congruent dissolution of secondary clays does not appear to further fractionate Ge/Si; in this case the solute ratio will be the same as the mineral ratio. Ge/Si ratios, in combination with other data, can

provide useful information on mineral sources, reaction pathways and water flow paths in the Critical Zone.

2.2 Site Description

Sampling was conducted in the Gordon Gulch sub-catchment of the Boulder Creek Critical Zone Observatory (Figure 2.1). Gordon Gulch is located west of the city of Boulder, CO in the Colorado Front Range at an elevation of 2,446-2,737 meters. It lies in the upper montane forest zone with mean annual precipitation of 55 cm and a mean annual temperature of 5.6^{o} C (Barry, 1973). Precipitation is highest in the summer while in the winter, precipitation falls in the form of snow. Stream discharge increases in early spring and summer as a result of snowmelt and higher precipitation. The watershed is divided into upper and lower Gordon Gulch. The upper catchment has a perennial stream while the lower can run dry for some months of the year. With an area of 0.95 km^2, the upper catchment is underlain by Paleoproterozoic biotite gneiss with granitoid intrusions (Gable, 1980). The elevation of Gordon Gulch is below the extent of Pleistocene glaciers and above Quaternary canyon incision from streams draining through the Front Range (Anderson et al., 2012). The catchment is aligned east-west and has north and south facing slopes. During the winter, the north facing slope has a snowpack while the south facing slope is partially covered (Anderson et al., 2011). Lodgepole pine (*Pinus contorta*) is dominant in the north facing slope with dense stands and few areas of understory. The south facing slope is dominated by ponderosa pine (*Pinus ponderosa*) with widely spaced stands and a grassy understory (Anderson et al., 2011). The low relief setting and tectonic stability since the end of the Laramide

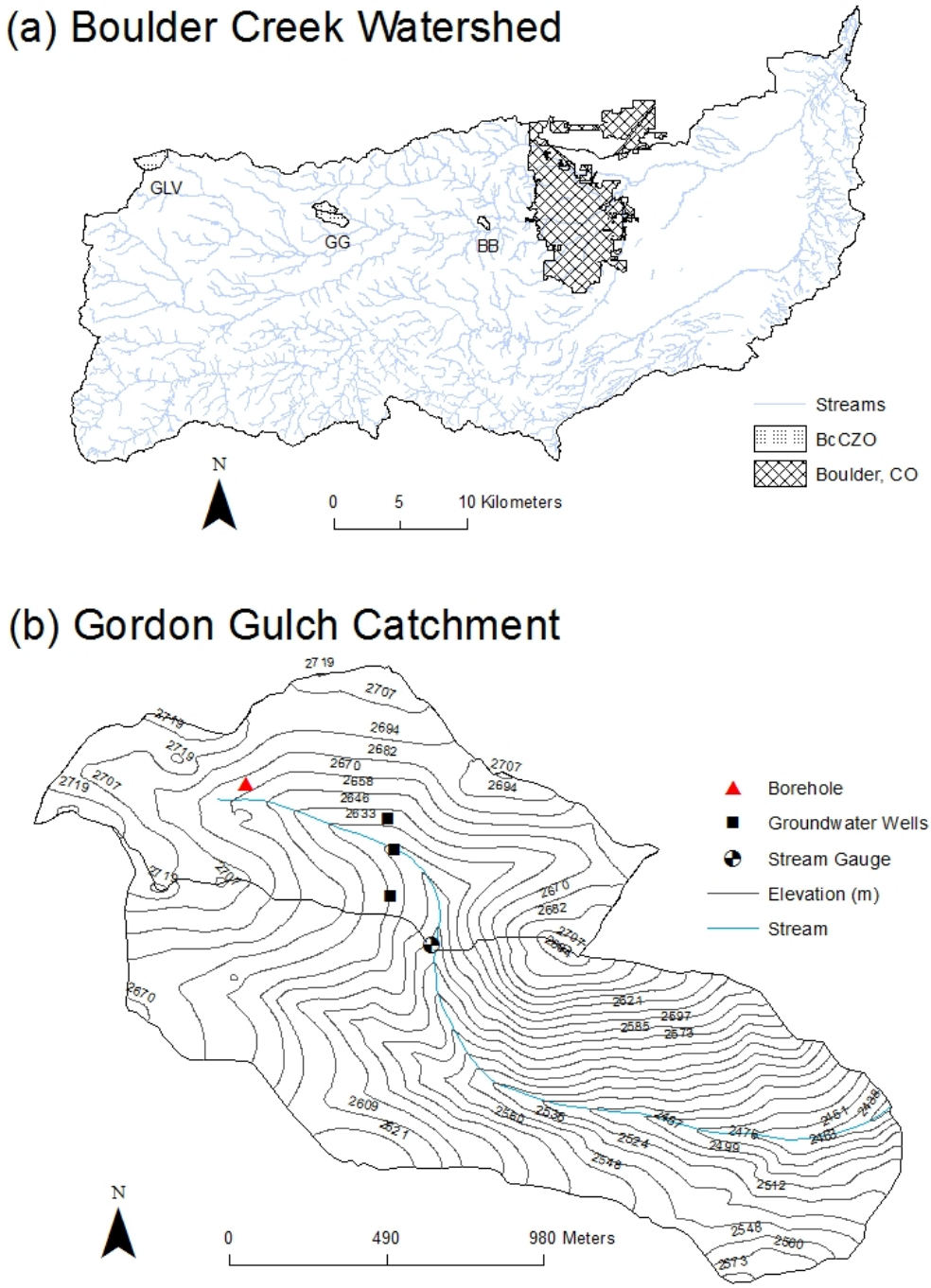

Figure 2.1: Map of Boulder Creek Critical Zone Observatory. (a) Boulder Creek watershed with the CZO catchments of Betasso (BB), Gordon Gulch (GG) and Green Lakes Valley (GLV). (b) Sampling location of soils (borehole), north-south groundwater well trasnect and stream in the Gordon Gulch catchment.

orogeny has resulted in the propagation of the weathering front to as deep as 19 meters

in some parts of the catchment. Differences in moisture retention caused by insolation may explain the presence of a deeper weathering front in the north facing slope (Befus et al., 2011). The major mineralogical phases in bedrock include plagioclase, potassium feldspar, quartz and biotite (Gable and Johnson Jr, 1996). Soils are alfisols with a Bt horizon of accumulated clay or Bw horizon of oxidized saprolite depending on slope aspect (Birkeland et al., 2003; Dethier et al., 2012). The major clay minerals in the soil include kaolinite, smectite and illite (Dethier and Bove, 2011). Minor amounts of clay are sourced from the bedrock and clay and Fe-oxides accumulate in the mobile regolith with progression of soil development (Dethier et al., 2012).

2.2.1 Biogenic Cycle of Silicon in the Boulder Creek CZO

Biologic cycling of Si in the Gordon Gulch catchment is expected to have a minor effect on silicon concentrations in stream water. Conifers like ponderosa and lodgepole pine are weak accumulators of silicon (Ma et al., 2001). Conifers have low rates of silica uptake relative to other tree classes, with reported values between 2-44 kg ha^{-1} yr^{-1} (Bartoli, 1983; Cornelis et al., 2010b; Gerard et al., 2008; Markewitz and Richter, 1998). Silica is taken up as aqueous silicic acid and mobilized to transpiration sites where biogenic opal structures (phytoliths) are formed (Cornelis et al., 2010a; Jones and Handreck, 1965). In conifers, phytoliths are concentrated in the needles (0.05 % wt. SiO_2) and Si content increases with needle age (Cornelis et al., 2010b). Silica restitution to the surface soil by litterfall ranges between 2-5 kg ha^{-1} yr^{-1} for conifers, once again, the lowest restitution rate among tree classes (Bartoli, 1983; Cornelis et al., 2010b). In vascular plants Ge/Si fractionation is believed to be associated with active

transport across the Casparian strip in the root (Ma et al., 2006; Sparks et al., 2011). Discrimination of Ge results in Ge/Si ratios in phytoliths of <0.5 (μmol mol^{-1}) (Blecker et al., 2007; Delvigne et al., 2009; Derry et al., 2005). Subsequent dissolution of phytoliths in soil can contribute a low Ge/Si component to stream waters (Derry et al., 2005).

Additional biological cycling of silicon is carried out by diatoms that build shells from silica. Blooms of the freshwater diatom *Didymosphenia geminata* have been observed in the Boulder Creek watershed as early as 2002 (Cullis et al., 2015). This diatom species can dominate algal communities in oligotrophic, high shear and turbulent streams of the Front Range (Cullis et al., 2012; Kirkwood et al., 2007). Cullis et al. (2015) demonstrated that benthic algae occurrences in Boulder Creek are dependent on substrate disturbances caused by fluid shear stress rather than nutrient concentrations in stream water. A study of factors that control *D. geminata* in Boulder Creek did not find a significant relationship between dissolved Si and algal abundance. The silica budget in Gordon Gulch does not appear to be significantly affected by blooming occurrences of *D. geminata* or other algal communities. In terms of Ge/Si, it has been shown that diatoms incorporate Si and Ge in similar proportions as present in their surrounding waters (Bareille et al., 1998; Filippelli et al., 2000; Froelich et al., 1992). Incorporation of silica by diatoms will not cause fractionation of the Ge/Si of stream water. Variations in Ge/Si must reflect mineralogic transformations in the catchment.

2.3 Methods

2.3.1 Sample Collection

Stream samples for this study were collected manually at the location of the stream gauge in upper Gordon Gulch, during calendar year 2012. Stream discharge data was collected from a permanent stream gauge using pressure-transducers. Stream flow measurements below 3 L s^{-1} are estimated values due to issues with the pressure-transducers during low flow conditions (Mills et al., 2017). Some discharge values in the data indicate a value of zero L s^{-1}. This does not mean complete drying of the stream. "Zero" flow represents low flow conditions where data values were below the calibration range for stream discharge. Groundwater samples were obtained during the same year from three wells in a north-south transect in upper Gordon Gulch catchment. Water samples were collected using acid-washed LDPE plastic bottles and filtered through 0.45 μm gridded cellulose ester filters. Samples were acidified with trace metal grade 68% HNO_3. Solid samples including soil, regolith and saprolite were collected from a drilling project organized by Kamini Singha from Colorado School of Mines that drilled as deep as 7 meters (borehole in Figure 2.1). Additionally, an outcrop near the upper reaches of Upper Gordon Gulch was sampled to characterize the bedrock of the catchment. For the colloids, a 12-liter stream sample was filtered through a high-capacity 0.45 μm Geotech dispos-a-filters™. The filtrate was centrifuged for 4.5 hours at 8000 rpm to remove colloids >0.02 μm (Mills et al., 2017). After centrifuging the filtrate, the supernatant was decanted and the centrifuged pellets of colloids (>0.02 d_{eff} < 0.45 μm) were combined for analysis. For the soil colloids, a soil sample 10 meters

from the stream channel and 200 m upstream from the gauge was collected by bucket auger until refusal at 50 cm (Mills et al., 2017). The soil sample was mixed with 4 L of deionized (DI) water and placed in a shaker table for 1 hour. Separation of soil colloids >0.02 μm was accomplished using the same procedure as described above. The sampling procedure operationally defines two element fractions; the dissolved plus colloidal (<0.45 μm) and the dissolved fraction (<0.02μm) (Mills et al., 2017).

2.3.2 Analysis of water samples

Water samples were analyzed using inductively coupled plasma optical emission spectroscopy (ICP-OES; AMETEK SpectroBlue) at Cornell University to determine solute concentrations. Sulfate was measured by ion chromatography at the University of Colorado Boulder. Germanium concentrations were measured using isotope-dilution hydride-generation ICP-mass spectrometry (Mortlock and Froelich, 1996). A ^{70}Ge spike was added to the water samples and equilibrated overnight. Germanium was analyzed using a custom hydride generation system coupled online to a Thermo-Finnigan Element 2 ICP-MS. Quantification was by isotope dilution using the ^{70}Ge/^{74}Ge ratio with corrections for mass bias and signal drift from sample-standard bracketing. At the same time, response curves were established by analysis of Ge standards at 5, 20, 50, 100 and 200 ng L^{-1}. Results from isotope dilution calculations were cross-checked against the standard response curves measured at m/z =74. With $(^{70}Ge/^{74}Ge)_{spike}$ = 162 the spike contribution to m/z 74 is negligible.

2.3.3 Ge spike equilibration with colloidal material

With evidence for the presence of a colloidal mineral phase in the 0.45 μm

filtered stream water samples (Mills et al., 2017), we conducted an experiment to test how effectively colloids equilibrated with the Ge spike. In order to measure total germanium in stream and groundwater, we need to make sure that the spike equilibrates with every phase (dissolved + colloidal). A subset of samples suspected of containing significant concentrations of colloids (collected during periods of high discharge) were spiked with the enriched ^{70}Ge tracer solution under three different conditions; acidic (pH <2), basic (pH ~11) and control (pH as sampled). Germanium spike was added and equilibrated overnight at 95^{o} C. The solubility of silica phases (quartz, opal) increases significantly at pH greater than 8.5 due to the dissociation of silicic acid (Dove, 1995). On the other hand, aluminosilicate clays will dissolve under strongly acidic conditions. Results showed that concentrations of dissolved Ge were greatest in the acidified samples, indicating that Ge spike and stream water (dissolved + colloidal) equilibration was more complete. Therefore, all stream and groundwater samples were adjusted to pH < 2 and equilibrated with the Ge spike overnight at 95^{o} C. Samples with a greater colloidal fraction had internal reproducibility of Ge concentrations (4 – 15% RSD) that was typically noisier than in samples where colloids were unimportant (3-8% RSD). We tentatively ascribe this to transport effects of colloids in the hydride generation system. Comparison of concentrations obtained by isotope dilution to those from standard response curves found that the two methods agreed in most cases to better than 15%. The agreement between two independent methods of determining concentration implies that the spike-sample equilibration under acidic conditions was effective. The exceptions were samples with [Ge] ≤ 10 ng L^{-1}. Samples with these low Ge concentrations also had very low levels of colloidal silica. Extensive prior testing of the

isotope dilution method indicates that it outperforms standard curve calibration at low Ge concentrations, so we use the isotope dilution results for these samples. Repeat analysis of standards and samples indicates reproducibility ≤ 10% above 5 ng L^{-1}, and ≤ 5% above 20 ng L^{-1}. These uncertainties are small relative to the observed range in Ge/Si in this study of a factor of approximately 30.

2.3.4 Analysis of solid samples

Mineral and clay separates were collected from the upper Gordon Gulch soil samples. Major mineral phases were separated using optical microscopy from soil samples collected at depths between 0.6-2.7 m. Mineral separations from multiple depths within the 0.6-2.7 m range were aggregated. Samples were first passed through a 2 mm mesh sieve. By hand picking, small homogenous mineral grains were separated from the < 2 mm fraction and set aside for analysis. The minerals were ground using a mortar and pestle until there were no light reflections from the faces of the grains in the powder. Prior to further analysis, the separated fractions were analyzed using a Theta-theta Scintag X-Ray Diffractometer at Cornell University. Clays (nominal 2 μm fraction) from 0.6-0.9, 1.8-2.1 and 2.4-2.7 m depths were separated following the procedure outlined in Moore and Reynolds (1997). Suspended clays were flocculated with $CaCl_2$ to separate from non-clay phases. Clay suspensions were pipetted onto a glass slide and air dried overnight. Additionally, the slides were placed in a desiccator containing ethylene glycol and placed in an oven set to 60° C for 8 hours. The slides were then scanned in the XRD to identify any expandable clay. Sample preparation for XRD analysis of colloids was the same as for the clay separations.

Solid samples analyzed for bulk chemistry and Ge were ignited in a muffle furnace at 900° C and then weighed. This value is represented as the loss on ignition (LOI) mass which is used to calculate element concentrations. A flux with a 1:1 ratio of lithium tetraborate and lithium metaborate was mixed with the sample in a ratio of 2:1. This flux and sample mixture was heated in the furnace at 1050° C to form a glass bead. The bead was poured into 50 ml of 10% HNO_3 and shaken overnight until the glass completely dissolved. The solutions were diluted in 2% HNO_3 and analyzed for major elements using ICP-OES and germanium using the ICP-MS. Standard curves for major element analysis were developed using rock standards prepared in the same way as the mineral separates. Major elements in stream and soil colloids could not be determined using the rock standard curves. Sample mass for these fractions was far lower than the mineral separates. Bottle standards with a lower concentration range were used for the determination of major elements in colloids. Germanium concentrations for the all solid phase samples was analyzed using bottle standards due to the large uncertainties in the stated Ge values of the rock standards.

2.4 Results and Discussion

2.4.1 Solid phase mineralogy, bulk chemistry and Ge/Si

XRD analysis and optical microscopy identified quartz, biotite, microcline and muscovite as the primary mineral phases in regolith (Appendix 6). Bulk chemistry and Ge/Si ratios were measured for the major mineral phases in regolith and in the clay size fraction (Table 2.1). Feldspars are a major mineral phase in the biotite gneiss bedrock. Their composition varies between plagioclase and alkali feldspar (Gable, 1980; Gable

and Johnson Jr, 1996). In this study, feldspar grains were analyzed and identified as microcline by XRD and had a Ge/Si of 1.88 μmol mol^{-1} (Table 2.1). Ge/Si ratios throughout this chapter will be presented in μmol mol^{-1}. Since mineral phases were separated by hand picking, it was difficult to distinguish between plagioclase and alkali feldspars. Germanium content and Ge/Si do not vary widely among feldspars, with reported values from 1.5 to 2.0 in non-pegmatitic feldspars of varying composition (Evans and Derry, 2002; Kurtz et al., 2002; Lugolobi et al., 2010). The Ge/Si ratio of muscovite and biotite are somewhat higher (2.02 and 2.58, respectively). X-ray analysis of mineral grains demonstrated the presence of quartz in all of the samples analyzed, with quartz peaks prominent in the muscovite and biotite separates. Quartz from Gordon Gulch had a Ge/Si of 1.03, so the presence of quartz inclusions in the biotite and muscovite mineral separates can lower the measured Ge/Si ratio. Quartz dissolution using the fusion method was unsuccessful in completely dissolving the glass bead (87 wt. % SiO_2 Table 2.1). Additionally, traces of NaO, K_2O, Al_2O_3 and Fe_2O_3 in the quartz bulk chemistry suggest inclusions from other minerals not identified in XRD. Minor inclusions of feldspar or iron-oxides would raise Ge/Si above 0.5 as reported in previous studies (Kurtz et al., 2002; Lugolobi et al., 2010).

Table 2.1: Major oxide and trace element concentrations for (LOI) mineral separates, clay size fraction and colloids

	SiO_2	Al_2O_3	CaO	MgO	Na_2O	K_2O	MnO	TiO_2	Fe_2O_3	P_2O_5	Total	Ge	Ge/Si	Al/Si	Fe/Si
						(Wt. %)					(Wt. %)	(ppm)	(µmol/mol)		
Bedrock Outcrop															
	69.3	13.9	0.3	0.1	2.0	9.1	nd	nd	1.0	-	95.6	1.22	1.45	0.23	0.02
Mineral Separates															
Quartz[1]	84.0	1.2	nd	0.0	0.1	0.7	0.0	nd	1.0	nd	87.0	1.0	1.03	0.02	0.02
Feldspar	61.9	18.3	0.0	0.1	1.6	14.1	0.0	nd	0.6	0.1	96.7	1.4	1.88	0.33	0.01
Muscovite	59.0	29.0	nd	0.9	0.4	9.9	0.0	0.7	3.1	0.0	103.0	1.4	2.02	0.56	0.08
Biotite	46.6	18.8	nd	1.2	0.4	3.1	0.1	4.1	26.6	0.0	100.9	1.5	2.58	0.46	0.85
Clay (>0.2 µm)															
2-3 feet	54.0	27.6	2.0	1.5	0.3	4.2	0.1	0.6	8.7	1.7	100.6	1.8	2.80	0.58	0.24
6-7 feet	51.2	29.5	0.9	1.1	0.2	3.6	0.1	0.3	9.7	0.5	97.0	1.5	2.43	0.65	0.28
8-9 feet	49.4	23.5	3.8	0.8	0.7	4.9	0.1	0.2	11.1	4.2	98.9	1.3	2.18	0.54	0.34
Colloids (<0.02 µm)															
Soil	56.8	25.1	1.0	1.9	0.0	2.4	0.1	nd	9.2	nd	96.5	2.1	3.84	0.63	0.31
Stream	19.4	11.0	13.5	0.9	2.4	4.9	0.1	nd	4.4	nd	56.5	1.5	3.73	0.64	0.34

nd= concentration is below detection

[1]incomplete dissolution during fusion, SO_2 missing

Clay mineral separates (< 2 μm size fraction) collected from drill core in the regolith at 0.6-0.9, 1.8-2.1, and 2.4-2.7 m depth intervals in upper Gordon Gulch contained mixtures of kaolinite, illite and quartz. In the 2 μm fractions, Al/Si is 0.54 to 0.65 and K_2O is 3.6 to 4.9 wt. %, consistent with the presence of quartz and illite (Table 2.1). Ge/Si ratios of the 2 μm fractions are 2.18 to 2.80. The Ge/Si ratio is lower than expected for kaolinite, and consistent with the presence of quartz with low Ge/Si. We used data from a local muscovite as a proxy for local illite composition and "unmixed" the kaolinite and illite components using K_2O, SiO_2 and Al_2O_3. We assume a kaolinite composition with a molar Al/Si 0.95 (Jepson, 1975) and $K_2O = 0$. In matrix form, the composition of the mineral mixture is:

$$Ax = b \tag{9}$$

where **A** is the matrix of mineral chemistry (Table 2.1), **b** is the composition of the < 2 μm fraction, and **x** is the vector of mineral fractions f, where $f_{illite} + f_{kaolinite} + f_{quartz} = 1$. For the 0.6-0.9 m sample, $f_{illite} = 0.41$, $f_{kaolinite} = 0.33$, $f_{quartz} = 0.26$. Using Ge/Si from Gordon Gulch quartz and muscovite (Table 2.1), the < 2 μm fraction value of 2.80 is satisfied with an end member kaolinite value = 5.2, consistent with kaolinites measured elsewhere (Lugolobi et al., 2010).

Similar to the clay fraction from soils, XRD shows that colloids are composed of a mixture between kaolinite, illite and quartz (Appendix 6). Stream colloids and soil colloids collected from a soil sample ten meters away from the stream have very similar XRD patterns as well as Ge/Si ratios (3.73 and 3.84, respectively). The sum of the major oxides of the stream colloids is well below 100%. Sample mass for stream colloids was 0.2 mg and this may have played a role in element loss during

the fusion process. Previous experience indicates that mass loss during fusions can result in poor yields when the total sample mass is in the range of a few milligrams or less. Nonetheless, the Ge/Si, Al/Si and Fe/Si ratios of the small stream colloid sample are similar to the larger colloid samples separated from soil for which the oxides summed to 96.5%. Consequently, we believe that the key elemental ratios obtained from the stream colloid samples are likely to be representative, even if the overall yield was low. The similarities between stream and soil colloids are consistent with the results of Mills et al. (2017) who proposed that soil wetting and drying processes results in the generation of Al-Si-Fe colloids that are transmitted to the stream.

2.4.2 Major elements and Ge/Si ratios in groundwater

Groundwater samples have an average concentration of 220 μM Si (Table 2.2). There are differences in silicon concentrations between the wells on the slopes and the well in the riparian area. The north-facing well has an average Si concentration of 198 μM. The south-facing is almost identical with 200 μM Si. In both wells, the range in silicon concentrations is between 185 μM and 210 μM. In contrast, the well in the riparian area has higher silicon concentrations with a range of 243-288 μM Si. Aluminum in groundwater is less than 1.0 μM and Fe concentrations are mostly near the ICP-OES detection limit of 0.60 μM, except for several samples from the well in the north-facing slope.

The north-facing and riparian wells have similar Ge/Si values of 0.20. The south-facing well has higher Ge/Si than the north-facing with Ge/Si near 0.50. There are differences in moisture and insolation between the two slopes. The north-facing slope

has a snowpack during the winter and sustains freezing temperatures in soils at depths of 0.3 meters (Anderson et al., 2010). This has caused deeper (>15 m) weathered profiles and greater clay accumulation than in the south-facing slope (Befus et al., 2011; Dethier et al., 2012). The south-facing slope has intermittent snowpack throughout the winter and has more outcrops (Anderson et al., 2010).

The Ge/Si range of 0.20-0.50 from groundwater is consistent with the incongruent weathering of a silicate phase, most likely feldspar, and neoformation of a clay (Kurtz et al., 2002; Lugolobi et al., 2010). Saturation indices calculated using Geochemist's Workbench® (GWB Version 10.0), show that groundwaters are supersaturated with respect to kaolinite (Ω = 1.02 to 2.18) and undersaturated with respect to K-feldspar, albite and anorthite (Figure 2.2, Appendix 7).

Table 2.2: Groundwater chemistry from wells in the south facing, north facing and riparian wells in upper Gordon Gulch of Boulder Creek CZO

Date Collected		Na (µM)	Mg (µM)	Al (µM)	Si (µM)	K (µM)	Ca (µM)	Fe (µM)	Ge (pM)	Ge/Si (µmol mol^{-1})
South Facing										
2/21/2012		318.8	860.7	0.4	198.3	43.2	665.5	0.2	88.0	0.44
3/22/2012		325.8	883.4	0.4	204.0	43.2	685.9	0.2	89.5	0.44
8/14/2012		297.5	844.3	0.4	198.0	44.5	689.4	0.2	88.2	0.45
9/20/2012		315.4	872.2	0.4	198.0	47.3	702.6	0.2	89.3	0.45
5/3/2012		306.2	866.1	0.4	195.5	45.5	687.4	0.2	97.7	0.50
5/24/2012		311.9	863.2	0.0	199.0	45.5	690.4	0.0	90.9	0.46
6/20/2012		322.3	883.4	0.0	202.6	45.3	681.4	0.0	84.5	0.42
7/16/2012		318.8	838.5	0.4	201.9	46.8	679.4	0.0	55.3	0.27
1/14/2012		341.0	900.6	0.4	205.1	45.3	685.4	0.0	109.4	0.53
1/20/2012		317.5	867.7	0.4	199.4	44.8	692.2	0.0	101.5	0.51
1/26/2012		330.1	881.7	0.0	204.4	43.2	688.7	0.0	99.8	0.49
1/31/2012		321.0	878.8	0.0	200.1	45.5	699.4	0.0	107.0	0.54
10/19/2012		313.2	868.5	0.4	200.8	44.0	692.2	0.2	87.7	0.44
11/20/2012		319.7	876.8	0.4	200.5	44.8	704.4	0.0	88.5	0.44
12/13/2012		325.4	881.7	0.4	199.4	42.2	696.6	0.0	94.0	0.47
	Average	319.0	871.2	0.3	200.5	44.7	689.4	0.1	91.4	0.46
	Max	341.0	900.6	0.4	205.1	47.3	704.4	0.2	109.4	0.54
	Min	297.5	838.5	0.0	195.5	42.2	665.5	0.0	55.3	0.27
North Facing										
2/9/2012		130.5	360.4	0.0	204.4	33.0	232.3	0.0	49.6	0.24
3/6/2012		156.6	350.1	0.0	184.8	32.7	278.7	5.4	41.9	0.23
3/22/2012		123.1	344.8	0.0	199.0	31.2	223.1	1.3	44.3	0.22
8/14/2012		123.5	338.6	0.4	195.1	33.0	230.6	22.4	30.8	0.16
9/20/2012		122.7	339.8	0.0	197.3	31.7	227.1	1.4	44.1	0.22
4/19/2012		124.4	348.1	0.0	201.5	33.8	228.6	0.0	51.1	0.25
5/24/2012		124.0	335.7	0.0	202.2	33.2	225.3	0.0	48.0	0.24
6/20/2012		121.4	342.7	0.0	194.8	31.2	217.3	251.8	39.5	0.20
1/14/2012		126.6	337.0	0.0	209.7	31.7	218.3	0.0	48.7	0.23
1/20/2012		122.7	343.6	0.0	196.5	31.2	223.1	150.2	36.6	0.19
1/26/2012		124.0	350.5	0.0	200.8	32.5	227.8	0.0	56.3	0.28
1/31/2012		123.5	351.8	0.0	196.9	31.2	229.6	72.9	37.6	0.19

continued on next page

Table 2.2 (*continued*)

Date Collected		Na (µM)	Mg (µM)	Al (µM)	Si (µM)	K (µM)	Ca (µM)	Fe (µM)	Ge (pM)	Ge/Si (µmol mol^{-1})
10/19/2012		124.0	344.0	0.0	194.4	32.0	226.1	173.7	55.9	0.29
11/20/2012		123.5	350.1	0.4	201.5	30.7	235.5	160.6	49.8	0.25
12/13/2012		124.8	342.3	0.4	191.2	33.0	228.1	11.8	31.1	0.16
	Average	126.3	345.3	0.1	198.0	32.1	230.1	56.8	44.4	0.22
	Max	156.6	360.4	0.4	209.7	33.8	278.7	251.8	56.3	0.29
	Min	121.4	335.7	0.0	184.8	30.7	217.3	0.0	30.8	0.16
Riparian Well										
3/1/2012		284.5	361.2	0.0	243.2	38.9	475.3	0.2	61.8	0.25
3/22/2012		247.5	357.1	0.0	261.7	22.3	436.1	0.0	61.8	0.24
8/14/2012		257.1	399.1	0.0	264.9	24.3	487.5	0.0	63.3	0.24
9/20/2012		247.1	396.6	0.4	284.1	26.3	488.8	0.2	60.7	0.21
4/19/2012		283.6	374.8	0.4	266.0	32.7	464.6	0.0	68.0	0.26
5/24/2012		237.5	374.0	0.0	262.8	24.6	464.6	0.2	57.1	0.22
6/20/2012		227.9	374.0	0.0	272.7	23.0	458.4	0.0	58.9	0.22
7/18/2012		254.9	406.9	0.0	252.8	23.3	483.3	0.0	56.2	0.22
1/14/2012		257.9	385.1	0.4	278.8	23.0	478.3	0.0	60.7	0.22
1/20/2012		238.8	389.2	0.0	278.1	26.6	475.6	0.0	61.1	0.22
10/19/2012		237.1	385.9	0.4	287.7	24.0	478.8	0.5	65.5	0.23
11/20/2012		240.1	382.2	0.0	281.3	27.1	472.1	0.0	62.4	0.22
12/13/2012		242.3	381.8	0.0	281.6	22.3	467.6	0.0	59.9	0.21
	Average	250.5	382.2	0.1	270.4	26.0	471.6	0.1	61.3	0.23
	Max	284.5	406.9	0.4	287.7	38.9	488.8	0.5	68.0	0.26
	Min	227.9	357.1	0.0	243.2	22.3	436.1	0.0	56.2	0.21

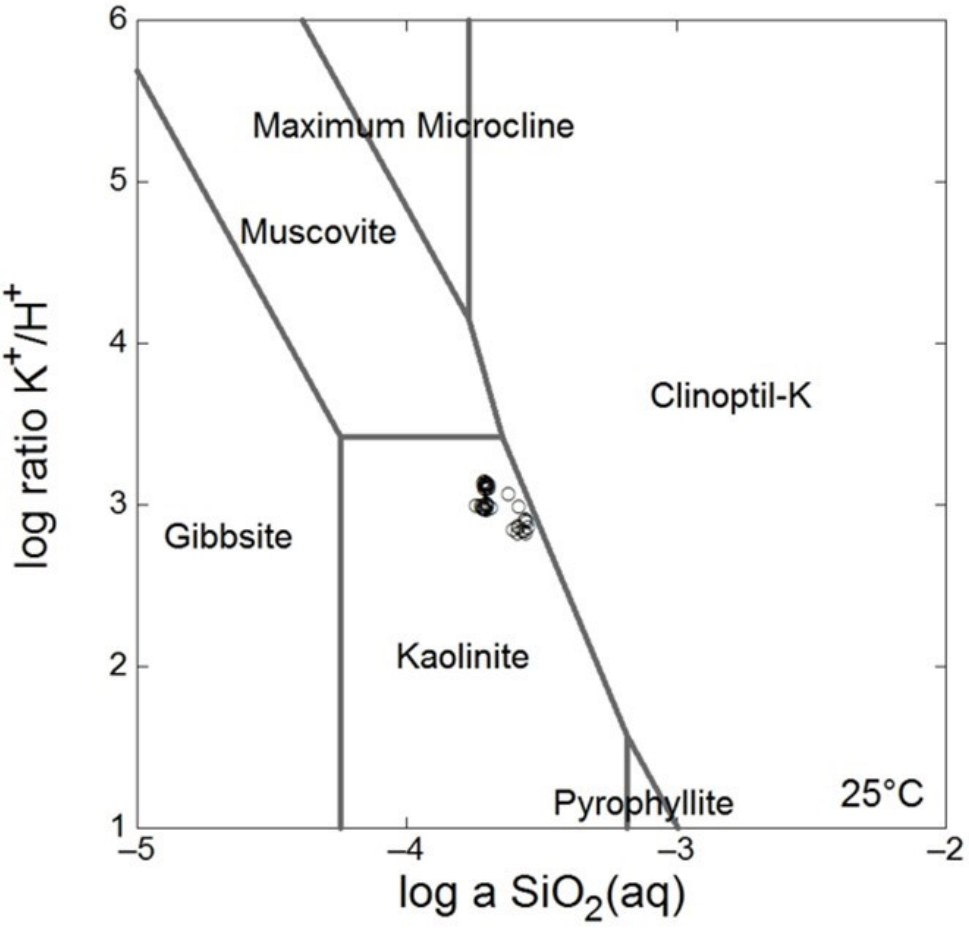

Figure 2.2: Boulder Creek CZO mineral stability diagram. Mineral stability diagram of log K^+/H^+ and log SiO_2. Groundwater samples (black circles) are within the field of kaolinite and indicate supersaturation with kaolinite.

Saturation indices for stream water are not necessarily meaningful because of the presence of colloidal Si and particularly Al. The incongruent weathering of feldspar (Ge/Si = 1.88 at Gordon Gulch) to kaolinite yields a clay with high Ge/Si and a depleted solute with Ge/Si ≤ 0.5. Using the $(Ge/Si)_{kaolinite} = 5.2$ derived above we can use the Ge/Si mass balance to estimate the fraction of Si released to groundwater during weathering versus that retained in kaolinite:

$$(Ge/Si)_{feldspar} = f_{GW} \cdot (Ge/Si)_{GW} + f_{kaol} \cdot (Ge/Si)_{kaol} \quad (10)$$

For the Gordon Gulch groundwater, Ge/Si mass balance implies that approximately 65% of the silica released during feldspar weathering is available as dissolved Si, while ≈ 35% is sequestered in a kaolin phase. The mass balance is almost exactly that predicted by the stoichiometry of the canonical feldspar to kaolinite weathering reaction:

$$2\,feldspar + 2H^+ + 9H_2O \Rightarrow kaolinite + 4Si(OH)_4 + 2cations \quad (11)$$

where 2/3 of the Si is released to solution as silica acid and 1/3 is incorporated into kaolinite. This suggest that this simple weathering reaction is a good representation of the first order control on dissolved silica release during groundwater – substrate reaction. Higher concentrations of Mg and K in the south facing well suggest dissolution of biotite in addition to feldspar. With a Ge/Si of 2.58, greater biotite weathering in the south facing slope could be responsible for the higher ratios observed in these groundwater samples.

2.4.3 Major elements and Ge/Si ratios in stream water

In 2012, upper Gordon Gulch catchment had discharge less than 3 L s^{-1} from January to February (Figure 2.3) with Si concentrations ranging between 247-307 μM. The snowpack in the spring was low and stream runoff was impacted with low

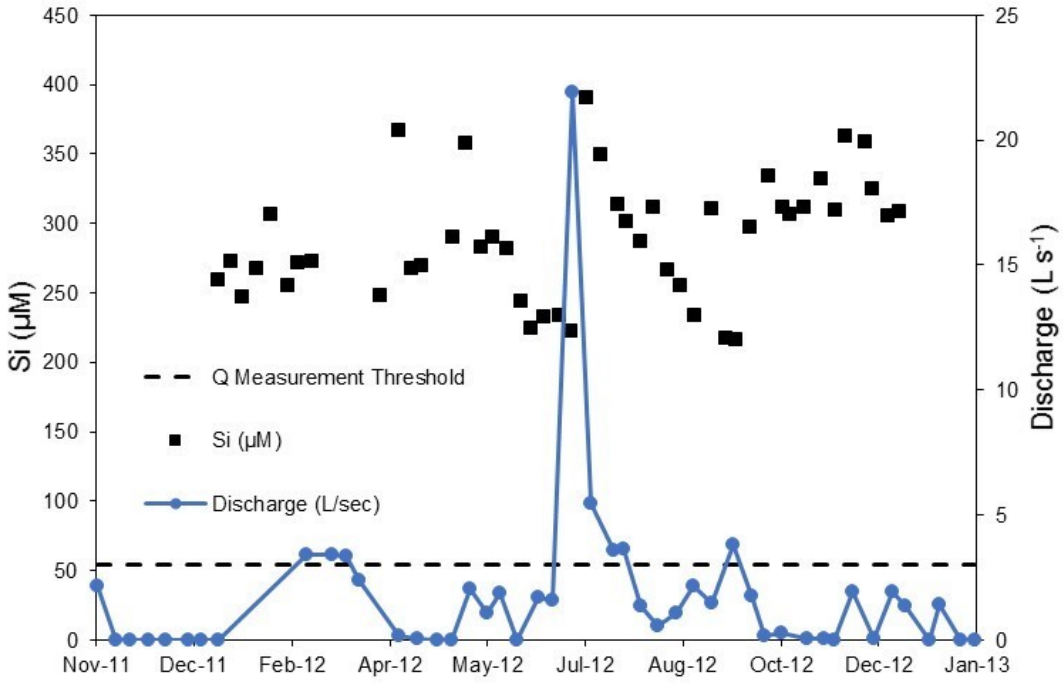

Figure 2.3: Discharge in Upper Gordon Gulch. Time series of discharge and Si concentrations for 2012 in the upper Gordon Gulch catchment of Boulder Creek CZO. Dashed black line indicates the limit of accurate discharge measurements. Discharge below 3 L sec^{-1} are estimates.

discharge. On July 11th, 2012 discharge increased to 22 L sec^{-1} following a storm event that registered up to 60 mm of rainfall on July 10th, 2012. During this event, stream water Si concentrations increased to 390 μM from 222 μM before the storm (July 3rd, 2012) (Table 2.3). After the event, Si concentration began to drop steadily towards 200 μM following the recession of the stream to base flow levels. This was the only major rainfall event during this calendar year. Thereafter, stream discharge dropped to baseflow levels (< 3 L s^{-1}) and only minor precipitation events were registered in the fall. Silicon concentrations reach a minimum at 200 μM in stream water during baseflow. Groundwater concentrations of Si are similar to concentrations in baseflow, consistent with the expectation that groundwater is a major contributor to the stream during

Table 2.3: Stream water chemistry in upper Gordon Gulch of Boulder Creek CZO.

Date Collected	Discharge ($L\ sec^{-1}$)	Na (µM)	Mg (µM)	Al (µM)	Si (µM)	K (µM)	Ca (µM)	Fe (µM)	$SO_4^{-2\dagger}$ (µM)	Ge (pM)	Ge/Si ($\mu mol\ mol^{-1}$)
1/4/2012	2.2	124.8	93.4	33.4	258.9	24.8	122.5	113.9	68.6	1384.4	5.35
1/11/2012	0.0	124.8	92.2	43.4	272.4	25.3	121.5	137.0	67.3	1632.3	6.00
1/17/2012	0.0	123.1	86.8	26.3	246.7	22.5	114.5	76.5	64.9	877.6	3.56
1/24/2012	0.0	130.5	94.2	38.2	267.4	22.5	126.5	135.0	64.2	1760.0	6.59
1/31/2012	0.0	125.3	93.8	58.6	306.6	21.2	127.0	147.0	63.9	1343.3	4.38
2/9/2012	0.0	126.6	87.6	23.7	254.6	20.7	119.5	81.8	62.5	1009.9	3.97
2/14/2012	0.0	124.8	85.6	33.7	271.3	19.7	115.3	93.1	60.3	782.1	2.88
2/21/2012	0.0	124.8	89.7	36.7	272.7	21.0	117.0	102.2	59.6	993.5	3.64
3/27/2012	3.4	117.4	81.5	28.9	247.8	20.2	106.5	80.9	63.9	653.6	2.64
4/6/2012	3.4	114.0	81.9	97.5	366.7	21.0	104.5	238.9	55.4	1155.1	3.15
4/12/2012	3.3	116.6	76.9	32.2	267.8	19.7	105.5	86.8	56.5	578.9	2.16
4/17/2012	2.4	117.0	81.1	41.9	269.9	20.7	107.3	115.3	54.1	1143.7	4.24
5/3/2012	0.2	123.5	89.3	45.2	289.5	20.2	120.8	124.8	48.6	1231.7	4.25
5/10/2012	0.0	119.6	85.6	86.4	357.1	21.2	111.5	206.8	42.8	1399.5	3.92
5/18/2012	0.0	127.9	94.2	35.6	282.4	19.7	125.8	100.8	39.0	1004.4	3.56
5/24/2012	0.0	127.0	91.8	44.5	289.8	20.5	121.0	129.1	33.0	1147.6	3.96
5/31/2012	2.0	133.5	107.0	35.2	282.0	21.0	146.2	119.6	28.7	1185.0	4.21
6/7/2012	1.1	142.7	123.4	12.2	243.9	24.8	175.7	62.0	20.9	292.1	1.20
6/12/2012	1.9	146.2	139.5	6.3	224.7	26.9	196.6	56.4	17.0	112.6	0.50
6/19/2012	0.0	160.1	158.0	1.1	232.5	32.2	231.0	46.7	8.5	79.4	0.34
6/27/2012	1.7	168.8	166.6	0.4	233.9	43.7	239.5	23.5	10.8	91.1	0.39
7/3/2012	1.6	156.2	161.7	0.4	222.2	33.0	239.5	32.2	8.5	66.1	0.30
7/11/2012	21.9	117.9	103.7	116.4	390.9	24.8	128.0	261.6	55.1	1195.5	3.06
7/18/2012	5.5	124.8	107.4	100.4	349.3	24.3	136.2	211.7	47.6	1054.5	3.02
7/27/2012	3.6	128.8	102.9	44.5	313.0	22.8	139.5	116.8	36.2	679.5	2.17
7/31/2012	3.7	128.8	102.0	40.0	301.2	20.2	139.0	116.0	28.7	940.8	3.12
8/7/2012	1.4	131.8	105.7	24.1	287.3	21.2	144.7	85.6	46.3	638.2	2.22
8/14/2012	0.5	136.6	112.7	37.1	311.5	20.7	152.5	117.5	21.6	544.1	1.75
8/21/2012	1.1	140.1	125.9	15.9	266.7	22.5	172.7	75.6	21.8	412.6	1.55
8/28/2012	2.2	148.3	137.8	11.5	255.3	27.9	189.1	52.5	23.2	152.8	0.60
9/4/2012	1.5	144.4	140.3	2.6	233.6	29.2	198.6	22.9	27.9	64.2	0.27
9/13/2012	3.8	147.5	146.1	46.7	310.5	32.7	199.6	153.8	29.1	512.4	1.65
9/20/2012	1.8	144.4	148.5	1.9	216.8	29.9	204.6	20.2	27.9	46.8	0.22
9/25/2012	0.1	146.2	148.5	1.5	215.8	32.7	210.8	16.5	25.8	36.8	0.17
10/2/2012	0.3	149.2	150.6	41.9	296.6	30.9	206.1	114.6	20.4	412.6	1.39

continued on next page

Table 2.3 (*continued*)

Date Collected	Discharge (L sec^{-1})	Na (µM)	Mg (µM)	Al (µM)	Si (µM)	K (µM)	Ca (µM)	Fe (µM)	$SO_4^{-2\dagger}$ (µM)	Ge (pM)	Ge/Si (µmol mol^{-1})
10/12/2012	0.0	147.9	140.3	66.0	333.6	32.7	193.9	161.3	20.1	524.9	2.42
10/19/2012	0.0	143.5	139.1	59.3	311.5	31.7	186.6	145.0	21.1	807.8	2.59
10/23/2012	0.0	145.3	132.5	52.3	306.6	28.4	187.4	121.9	20.7	545.7	1.78
10/30/2012	2.0	139.2	121.4	56.7	311.5	31.7	162.4	132.5	25.5	520.6	1.67
11/8/2012	0.0	144.0	125.5	70.0	332.2	26.3	170.2	151.0	26.8	706.2	2.13
11/15/2012	1.9	139.6	118.1	65.6	309.1	24.3	159.9	133.2	28.3	474.3	2.29
11/20/2012	1.4	136.6	111.1	94.9	362.5	27.9	152.7	206.3	27.1	1048.3	2.89
11/30/2012	0.0	138.3	118.1	93.0	358.2	25.6	158.4	194.8	27.4	1005.8	2.81
12/4/2012	1.4	148.3	133.3	64.1	324.7	24.6	174.4	140.4	29.8	522.4	3.10
12/12/2012	0.0	143.5	124.7	57.8	305.1	26.3	169.9	119.8	33.4	593.3	1.95
12/18/2012	0.0	136.1	108.6	63.0	308.0	24.8	148.5	131.8	32.1	617.6	2.01

baseflow conditions.

The sample collected at 22 L s^{-1} has a silicon concentration of 391 μM (Figure 2.3). Over an increase in discharge of approximately two orders of magnitude, measured silicon varies by less than a factor of two. A log-log plot of concentration to discharge yields a power law slope of 0.06 (Figure 2.4a), positive but close to the chemostatic case of Godsey et al. (2009). This behavior implies that the stream flux of silicon increases by a factor of 14 between base flow (Q = 2 L s^{-1} & 222 μM Si) and the high discharge event of July 11th, 2012 (Q = 22 L s^{-1} & 391 μM Si). New sources of dissolved silicon must be activated for the flux to dramatically increase. Power law slopes for Ge, Al and Fe are more strongly positive (0.28 to 0.46), while the data show more scatter than Si (Figure 2.4b, 2.4c and 2.4d). Colloidal transport with increasing discharge may lead to flushing of these solutes that cause positive C-Q slopes. Positive power law slopes in C-Q space have been shown to be associated with colloid transport elsewhere (Trostle et al., 2016).

Aluminum and iron concentrations in stream water (filtered at 0.45 μm) are strongly positively correlated with silicon concentrations (Figure 2.5a & 2.5b). In stream water, Al and Fe can be as high as 116 μM and 261 μM respectively. The pH in stream water is near neutral, therefore the solubility in stream water of Al and Fe should be low for this system (Stumm and Morgan, 2012). Mills et al. (2017) determined that most of the "dissolved" Al and Fe (< 0.45 μm) reside in the colloidal phase by comparing concentration of these elements in the centrifuged filtrate (truly dissolved) and total filtered solids in stream water. Regression analysis indicates that at "zero" Al and Fe, Si in stream water is predicted to have a value of 222 (-11/+23) and 195 (-

12/+25) μM Si respectively. These relationships converge in the range for Si concentrations in groundwater (200 μM Si) and are similar to base flow. This suggests that the truly dissolved silicon falls near 200 μM Si. Concentrations of Al and Fe are also low in most baseflow samples, while higher discharge samples have higher values of Al and Fe. The Si-Al-Fe systematics are consistent with groundwater as the dominant source for baseflow conditions.

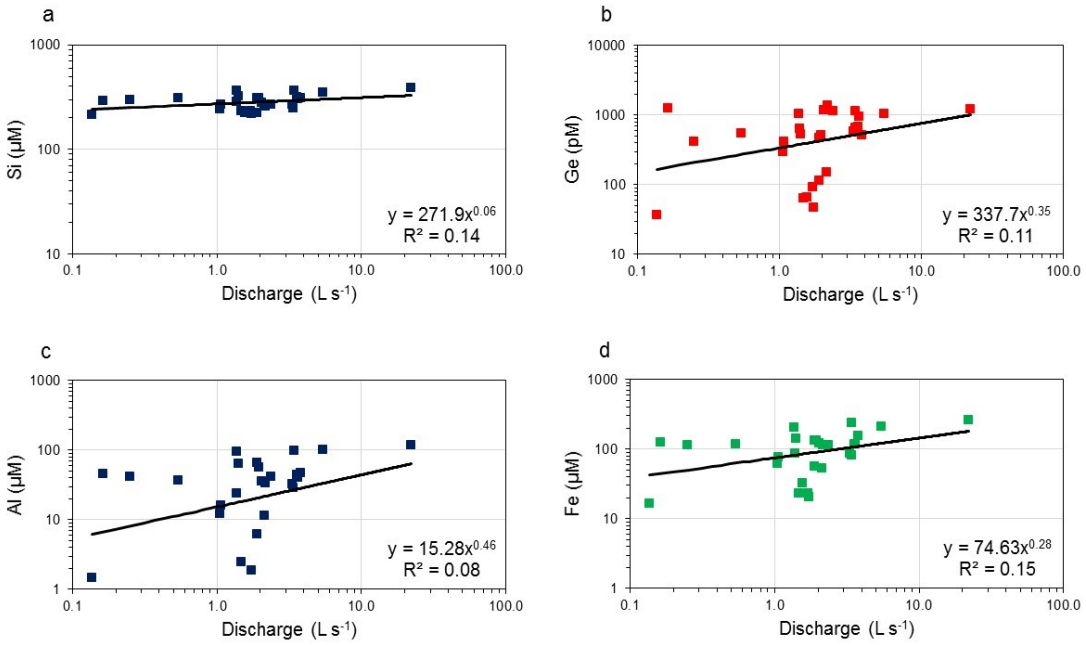

Figure 2.4: Upper Gordon Gulch concentration-discharge relationships. Concentration-discharge pattern for (a) Si, (b) Ge, (c) Al and (d) Fe in upper Gordon Gulch for calendar 2012.

The Al, Fe and Si correlation in stream samples yield an Al/Si = 0.65 mol/mol (Figure 2.5a), essentially identical to the bulk chemistry of both stream and soil colloids (Table 2.1), and consistent with the presence of kaolinite and illite identified by XRD

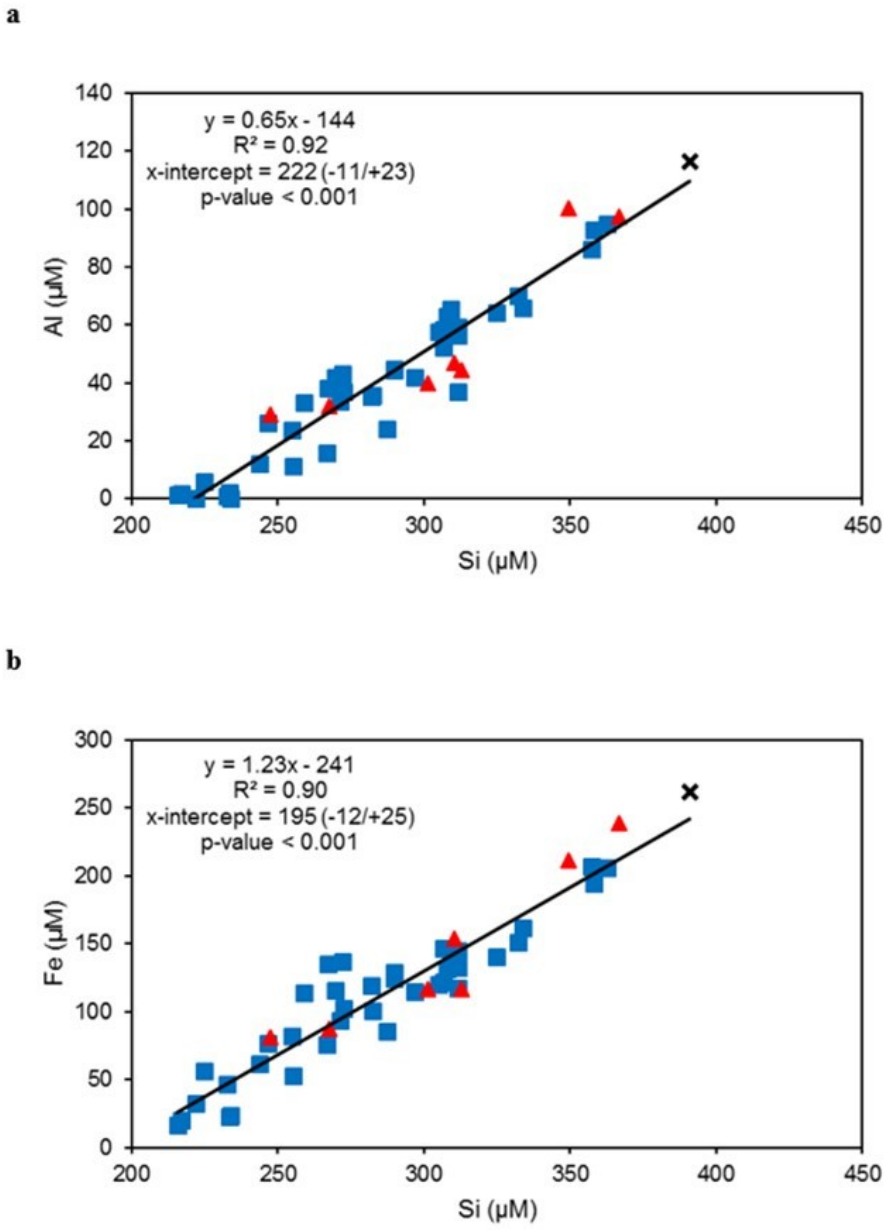

Figure 2.5: Silicon relationships with Al and Fe. Scatter plots showing (a) relationship of Al and Si and (b) Fe and Si in stream water at upper Gordon Gulch in calendar 2012.

in the colloidal fraction. The bedrock Al/Si is lower at 0.23 (Table 2.1). Therefore, the stream Al/Si fractionation displays the interaction with an enriched Al mineral phase. The Fe/Si ratio derived from the stream water regression is 1.2, notably higher than measured in the colloids (0.3). A crystalline Fe phase was not identified in XRD,

although an Fe-rich phase is visible in SEM images of the colloids (Mills et al., 2017). The Fe and Si correlation may reflect the presence of both an amorphous iron-oxide phase and/or organically bound Fe that was not captured in the colloid separation process. The linear Si-Al-Fe relationships in Figure 2.5 represent mixing lines between a high Si-Al-Fe component represented by the high discharge sample (Q = 22 L sec^{-1}) and a groundwater component with Si ≈ 200 μM and near zero values of Al and Fe. At high discharge, colloidal transport increases concentrations of Si, Al, Fe and Ge, resulting in positive power law slopes in C-Q space.

2.4.4 Ge/Si end-member

In stream water, Ge/Si ranges widely from 0.17 to 6.59 at discharge less than 3 L s^{-1} (Figure 2.6). The range narrows to 2.16 to 3.15 as discharge increases above 3 L s^{-1}. The two samples with discharge higher than 5 L s^{-1} have Ge/Si ratios of 3.02 (Q = 5.46 L s^{-1}) and 3.06 (Q = 21.96 L s^{-1}). A plot of Ge/Si vs 1/Si suggests the presence of an end member in addition to the colloidal and groundwater end members discussed above (Figure 2.7a). However, the higher discharge samples (and some lower Q samples) define a mixing line between a groundwater end member with Ge/Si ≈ 0.3 and Si ≈ 200 μM (1/Si = 0.005), and a colloidal component with Ge/Si ≈ 3.8 (based on analysis of both soil and stream colloids) and Si ≈ 400 μM (1/Si = 0.0025), consistent with the Si-Al-Fe relations discussed above. The Ge/Si mass balance can place constraints on the fractional contribution of colloidal and groundwater derived silica to the stream silica budget. For a mixture of colloidal and groundwater (GW) derived silica:

(12) $$(Ge/Si)_{stream} = f_{GW} \cdot (Ge/Si)_{GW} + f_{colloid} \cdot (Ge/Si)_{colloid}$$

Where;

(13) $$f_{GW} + f_{colloid} = 1$$

Then;

(14) $$f_{GW} = \frac{(Ge/Si)_{stream} - (Ge/Si)_{colloid}}{(Ge/Si)_{GW} - (Ge/Si)_{colloid}}$$

With $(Ge/Si)_{colloid}$ = 3.8 and $(Ge/Si)_{GW}$ = 0.3, the contribution of groundwater end member to the high discharge flux of silica ((Ge/Si)stream = 3.05) is $f_{GW} = 0.21$, while $f_{colloid} = 0.79$. The analysis implies that most of the ≈ 14× increase in Si flux associated with the high Q event of July 11th, 2012 is in the form of colloidal Si, but that groundwater fluxes must also increase by a factor of 3 to 4 over base flow conditions. Colloidal transport is typically thought to be important for strongly hydrolyzing metals such as Al, Th, and REE, but not for Si (Dupré et al., 1999; Eyrolle et al., 1996; Trostle et al., 2016). This study demonstrates that colloidal transport can be important for Si where soil processes can produce sub-micron scale alumino-silicate particles in sufficient quantity (Mills et al., 2017). We also note that the relationship along the inferred mixing line between groundwater and a colloidal component has a negative slope in Ge/Si vs 1/Si space. This pattern is unusual; in most streams the same plot yields a positive correlation. Positive correlation slope represent mixing between a low Ge/Si - high [Si] component produced by incongruent weathering and a higher Ge/Si - low [Si] component resulting from congruent dissolution of secondary minerals

(Froelich et al., 1992). Thus, the pattern of Ge - Si relations may suggest the presence or absence of a colloidal phase.

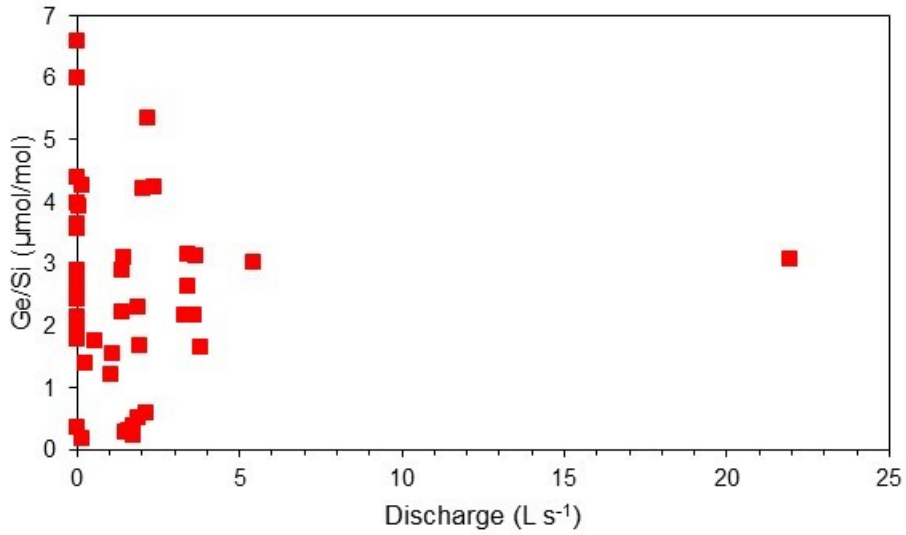

Figure 2.6: Ge/Si in stream water of Upper Gordon Gulch. Ratio-discharge pattern for Ge/Si in 2012.

During low flow conditions, a more complex pattern with large variability in Ge/Si is apparent. Data from low discharge periods indicate the presence a third end-member with high Ge/Si ≤ 7 and a Si concentration around 300 μM (Figure 2.7a). This component is common at low discharge in the winter and spring months of 2012. Ge/Si ratios range between 3.15-6.59 in these samples. The value at 6.59 is an indicator that a natural weathering process is not responsible for this high Ge/Si. These kinds of high values are only observed in waters influenced by hydrothermal fluids, sulfide ore weathering, or coal ash contamination (Anders et al., 2003; Evans and Derry, 2002; Froelich et al., 1992). Geothermal springs are not present in the Gordon Gulch catchment. The high Ge/Si ratios are positively correlated with sulfate concentrations in

stream water (Figure 2.8). Sulfate in stream water can be derived from oxidation of

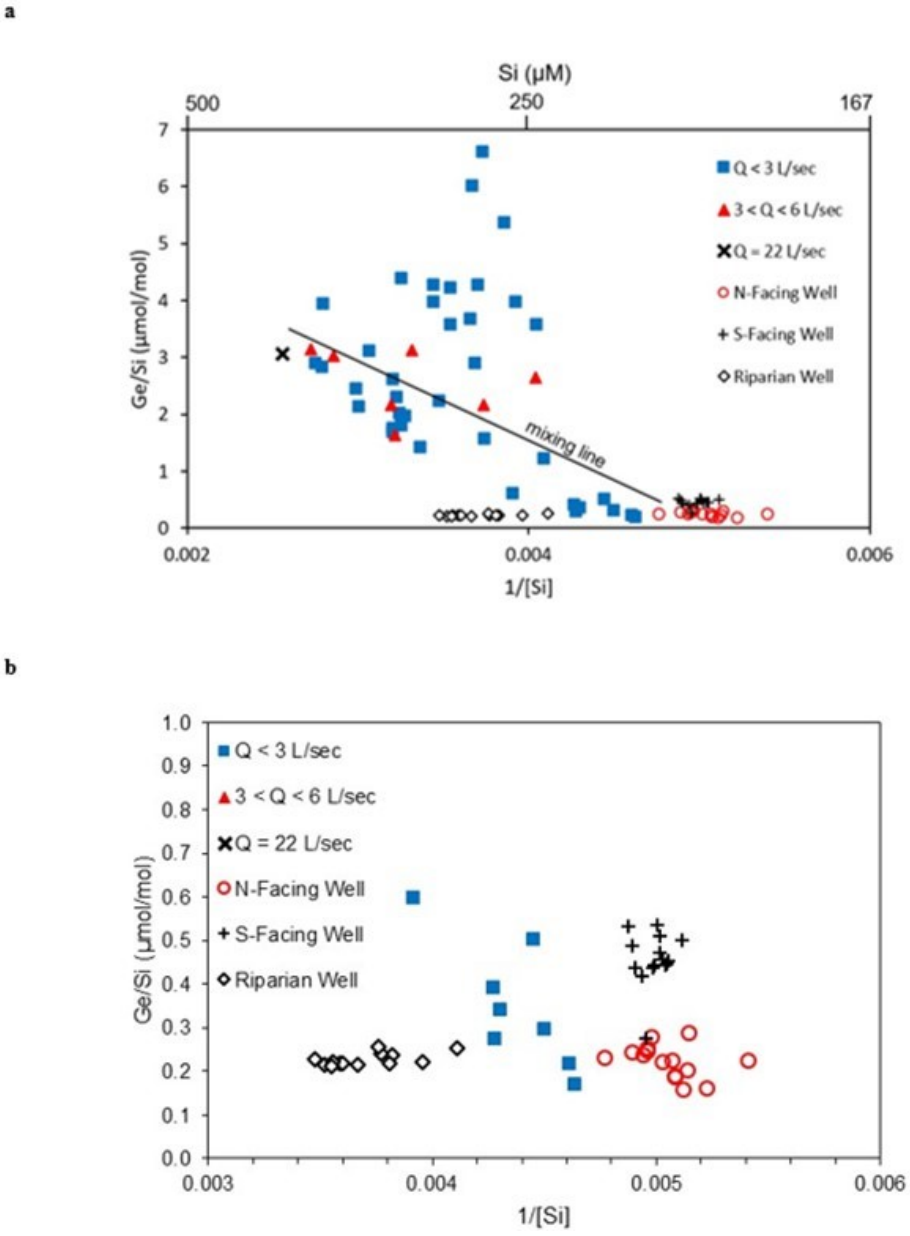

Figure 2.7: Ge/Si and 1/Si mixing space in Boulder. **(a)** Ge/Si end-members in stream water and groundwater samples for 2012. Open red circles are groundwater samples in the north-facing well. Black crosses are groundwater samples in the south-facing well. Open black diamonds are groundwater samples in the riparian well. Mixing line is defined by groundwater end-member ([Si] ≈ 200 µM, Ge/Si ≈ 0.3 µmol mol^{-1}) and colloidal end-member ([Si] ≈ 400 µM, Ge/Si ≈ 3.8 µmol mol^{-1}). **(b)** Zoomed plot of the Ge/Si end-members in stream water and groundwater for 2012. Blue squares represent samples collected at baseflow (<3 L sec^{-1}). Open red circles are groundwater samples in the north-facing well. Black crosses are groundwater samples in the south-facing well. Open triangles are groundwater samples in the riparian well.

sulfide minerals in bedrock and atmospheric deposition. The Gordon Gulch catchment is part of the Boulder County Tungsten District. Within the lower part of the catchment, the historic mines of Oregon, Quaker City, Misers and Ophir extracted ferberite ($FeWO_4$) in the early part of the twentieth century (Lovering, 1953). Currently these mines are out of operation. Sulfide minerals are associated with ferberite mineralization. In the Gordon Gulch catchment, pyrite and sphalerite were found to lightly cover the tungsten ore veins (Lovering, 1953). Sphalerite is also known to contain high traces of Ge up to several hundred parts per million (Bernstein, 1985). In upper Gordon Gulch (our study area) there are no reports of sulfide mineralization or mining activity, and no evident mineralized zones. However, it remains possible that sulfide weathering could contribute Ge and SO_4^{2-} to upper Gordon Gulch waters.

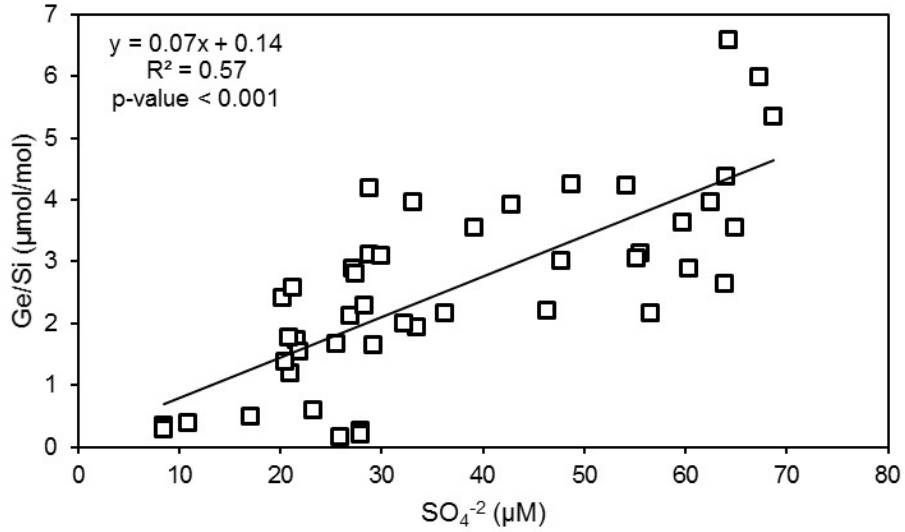

Figure 2.8: Ge/Si and sulfate concentrations in Upper Gordon Gulch. Relationship between Ge/Si and sulfate concentrations in stream water for 2012 for upper Gordon Gulch.

The other potential source of enriched Ge and SO_4^{2-} to Gordon Gulch is coal fly ash deposition from nearby coal powered electrical generation plants. Germanium is enriched in coal and through the coal burning process, concentrates in coal combustion residues like coal fly ash (Froelich and Lesley, 2001). To the west of the Gordon Gulch catchment, the Hayden power plant is a major emitter of PM 2.5 and PM 10 (particulate matter ≤ 2.5 and 10 μm diameter) (*U.S. EPA*, 2013). In the winter, the annual frequency for wind direction was north-east (Figure 2.9), effectively bringing air from the Hayden region to Gordon Gulch.

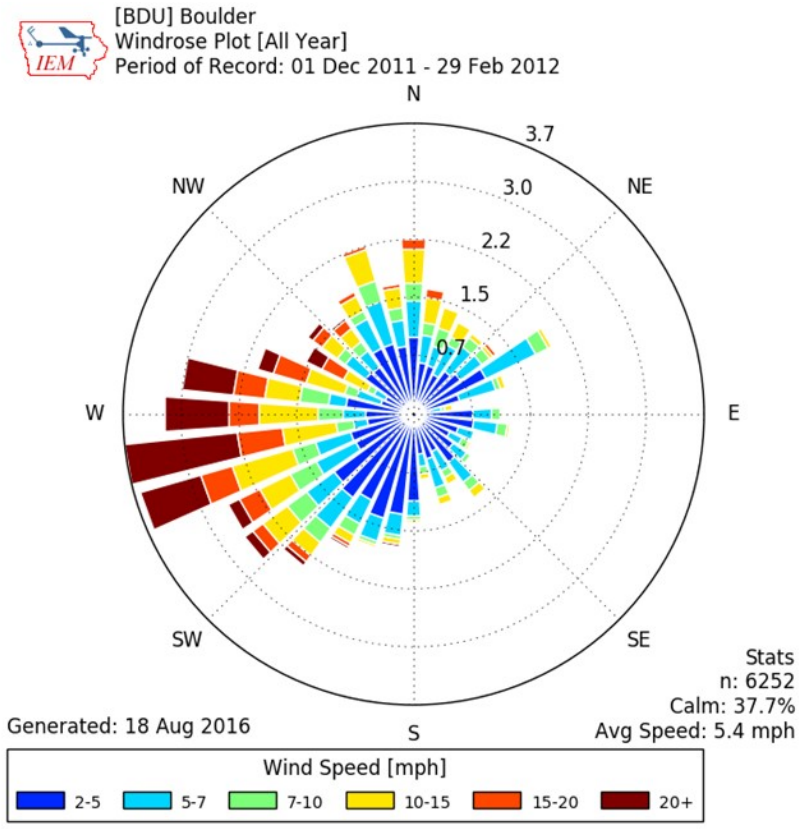

Figure 2.9: Boulder, CO wind rose plot. Frequency and speed of wind blowing from each direction in Boulder, CO during the winter months of December January and February. Plot was obtained from the Iowa Environmental Mesonet website (http://mesonet.agron.iastate.edu/). Accessed on August 18, 2016.

The predominance of the westerly winds could have deposited emissions from the Hayden power plant on the snowpack in the catchment. Since discharge is low from January to May in 2012, a large input of this material is not necessary to produce anomalous Ge/Si ratios. Using a mean fly ash Ge/Si = 25 (Froelich et al., 1985) a 15 – 20 % contribution of fly ash – derived Si in a stream sample can yield $(Ge/Si)_{stream} = 6$. However, this estimate is in fact very conservative, since coal ash retaining ponds can have $(Ge/Si)_{dissolved}$ in excess of 1000, as Ge is released from coal ash solution more efficiently than Si (Froelich and Lesley, 2001). Additionally, the two size fractions of particulate matter (2.5 and 10 μm) of which Hayden is a top emitter, are typically the most enriched in germanium (Querol et al., 1995). If the effective coal ash end member has a Ge/Si =100 μmol/mol only a few percent Si at very low flow conditions need be derived from ash to explain the highest Ge/Si we observe in Gordon Gulch. Similar to the measurements of particulate matter, the Hayden power plant is also a regionally important source of sulfate emissions in the state of Colorado (*U.S. EPA*, 2013). Back trajectory analysis of SO_4^{2-} in the Front Range has shown that the main sources are derived from the west of the continental divide (Gebhart et al., 2011). In order to understand the effect on SO_4^{2-} deposition from coal fired power plants, wet and dry SO_4^{2-} deposition data was analyzed for the year 2012. Wet deposition of SO_4^{2-} from the National Atmospheric Deposition Program (NADP) was obtained for the Sugarloaf monitoring station (CO94) near the Gordon Gulch catchment. Additionally, dry deposition for the Rocky Mountain National Park (ROM406) station of the CASTNET network was obtained to calculate the contribution of particulates to the SO_4^{2-} flux. In 2012, the median SO_4^{2-} dry deposition was 12% of the total S deposition in the

catchment. Deposition was greatest during the summer with the highest rates of deposition between the month of May and July. Mass balance of SO_4^{2-} in Gordon Gulch shows that atmospheric inputs are very similar to exports from stream water. The mean atmospheric deposition flux of SO_4^{2-} is 5.5 kg $week^{-1}$ compared to the mean stream water flux of 4.14 kg $week^{-1}$. Students t-test of the mean fluxes indicates that the fluxes are identical at a 95% significance level. Additionally, Cl^-/SO_4^{2-} ratios in wet + dry deposition for the month of January range between 0.24-0.44 (mol/mol). Stream water Cl^-/SO_4^{2-} for this month fall within a narrower range of 0.40-0.42 (mol/mol) near the upper end of the ratios of atmospheric deposition. Oxidation of sulfide minerals would offset Cl^-/SO_4^{2-} of stream water to a lower ratio since Cl/S ratios in sulfide minerals are very low. Consequently, we conclude that the most likely cause of elevated Ge/Si during the winter and spring low discharge samples is atmospheric deposition from coal combustion emissions. This conclusion is consistent with the observation that groundwater is the dominant source of stream water at low Q, and has a low Ge/Si ratio. If sulfide weathering was an important input at low Q then we would expect to see high, not low Ge/Si in groundwater. Further work needs to be done in order to quantify the impact of atmospheric deposition on the snowpack of Gordon Gulch. Snow could be collected to measure metalloids enriched in coal ash like Ge, As and Sb in order to quantify inputs of this source.

2.5 Conclusion

The Gordon Gulch catchment shows chemostatic C-Q behavior for silica, implying large variations in Si flux as a function of discharge. A colloidal phase that

contains kaolinite, illite and quartz can be separated from the 0.02 μm filtrate. Strong correlations of Si with Al and Fe reflect the presence of Si-Al-Fe bearing colloids as a major transport phase for Si at moderate to high discharge. Ge/Si data on groundwater, stream water and collloids support this view, and permit quantification of the influence of colloids on stream Si export fluxes. The Si-Al-Fe-Ge systematics in Gordon Gulch can be explained as a mixing relationship between a groundwater component with $\approx$ 200 μm Si, Ge/Si $\approx$ 0.3 and near zero Al and Fe, and a colloidal component with Si $\approx$ 400 μm, Ge/Si $\approx$ 3.8, and Al/Si = 0.64. At low Q, the main component is groundwater. The chemostatic behavior of Gordon Gulch can be explained by the activation of transport of colloidal alumino-silicate material at increasing discharge, potentially linked to wetting and drying cycles and changes in soil solution ionic strength (Mills et al., 2017). The mechanisms that can produce chemostatic behavior in C-Q plots are evidently varied. Anomalously high Ge/Si ratios at low discharge in Gordon Gulch appear to reflect contamination by coal fly ash.

References

Anders, A.M., Sletten, R.S., Derry, L.A. and Hallet, B. (2003) Germanium/silicon ratios in the Copper River Basin, Alaska: Weathering and partitioning in periglacial versus glacial environments. Journal of Geophysical Research-Earth Surface 108.

Anderson, S.P., Anderson, R.S., Hinckley, E.L.S., Kelly, P. and Blum, A. (2011) Exploring weathering and regolith transport controls on Critical Zone development with models and natural experiments. Applied Geochemistry 26, S3-S5.

Anderson, S.P., Anderson, R.S. and Tucker, G.E. (2012) Landscape scale linkages in critical zone evolution. Comptes Rendus Geoscience 344, 586-596.

Anderson, S.P., Blum, A.E., Hinckley, E.S., Lee, J., Gilbert, R., Trotta, J. and Dethier, D. (2010) Slope aspect and weathering in the Colorado Front Range. Geochimica Et Cosmochimica Acta 74, A21-A21.

Bareille, G., Labracherie, M., Mortlock, R.A., Maier-Reimer, E. and Froelich, P.N. (1998) A test of (Ge/Si)(opal) as a paleorecorder of (Ge/Si)(seawater). Geology 26, 179-182.

Barry, R.G. (1973) A climatological transect on the east slope of the Front Range, Colorado. Arctic and Alpine Research, 89-110.

Bartoli, F. (1983) The Biogeochemical Cycle of Silicon in 2 Temperate Forest Ecosystems. Ecol Bull, 469-476.

Befus, K.M., Sheehan, A.F., Leopold, M., Anderson, S.P. and Anderson, R.S. (2011) Seismic Constraints on Critical Zone Architecture, Boulder Creek Watershed, Front Range, Colorado (vol 10, pg 915, 2011). Vadose Zone Journal 10, 1342-1342.

Berner, R.A., Lasaga, A.C. and Garrels, R.M. (1983) The carbonate-silicate geochemical cycle and its effect on atmospheric carbon-dioxide over the past 100 million years. American Journal of Science 283, 641-683.

Bernstein, L.R. (1985) Germanium Geochemistry and Mineralogy. Geochimica Et Cosmochimica Acta 49, 2409-2422.

Birkeland, P., Shroba, R., Burns, S., Price, A. and Tonkin, P. (2003) Integrating soils and geomorphology in mountains—an example from the Front Range of Colorado. Geomorphology 55, 329-344.

Blecker, S.W., King, S.L., Derry, L.A., Chadwick, O.A., Ippolito, J.A. and Kelly, E.F. (2007) The ratio of germanium to silicon in plant phytoliths: quantification of biological discrimination under controlled experimental conditions. Biogeochemistry 86, 189-199.

Buttle, J.M. and Peters, D.L. (1997) Inferring hydrological processes in a temperate basin using isotopic and geochemical hydrograph separation: A re-evaluation. Hydrological Processes 11, 557-573.

Capobianco, C. and Navrotsky, A. (1982) Calorimetric Evidence for Ideal Mixing of Silicon and Germanium in Glasses and Crystals of Sodium-Feldspar Composition. Am Mineral 67, 718-724.

Carey, J.C. and Fulweiler, R.W. (2012) The Terrestrial Silica Pump. Plos One 7.

Chanat, J.G., Rice, K.C. and Hornberger, G.M. (2002) Consistency of patterns in concentration-discharge plots. Water Resources Research 38.

Cornelis, J.T., Delvaux, B., Cardinal, D., Andre, L., Ranger, J. and Opfergelt, S. (2010a) Tracing mechanisms controlling the release of dissolved silicon in forest soil solutions using Si isotopes and Ge/Si ratios. Geochimica Et Cosmochimica Acta 74, 3913-3924.

Cornelis, J.T., Ranger, J., Iserentant, A. and Delvaux, B. (2010b) Tree species impact the terrestrial cycle of silicon through various uptakes. Biogeochemistry 97, 231-245.

Cullis, J.D.S., Gillis, C.A., Bothwell, M.L., Kilroy, C., Packman, A. and Hassan, M. (2012) A conceptual model for the blooming behavior and persistence of the benthic mat-forming diatom Didymosphenia geminata in oligotrophic streams. Journal of Geophysical Research-Biogeosciences 117.

Cullis, J.D.S., McKnight, D.M. and Spaulding, S.A. (2015) Hydrodynamic control of benthic mats of Didymosphenia geminata at the reach scale. Canadian Journal of Fisheries and Aquatic Sciences 72, 902-914.

Delvigne, C., Opfergelt, S., Cardinal, D., Delvaux, B. and Andre, L. (2009) Distinct silicon and germanium pathways in the soil-plant system: Evidence from banana and horsetail. Journal of Geophysical Research-Biogeosciences 114.

Derry, L.A., Kurtz, A.C., Ziegler, K. and Chadwick, O.A. (2005) Biological control of terrestrial silica cycling and export fluxes to watersheds. Nature 433, 728-731.

Dethier, D.P., Birkeland, P.W. and McCarthy, J.A. (2012) Using the accumulation of CBD-extractable iron and clay content to estimate soil age on stable surfaces and nearby slopes, Front Range, Colorado. Geomorphology 173, 17-29.

Dethier, D.P. and Bove, D.J. (2011) Mineralogic and Geochemical Changes from Alteration of Granitic Rocks, Boulder Creek Catchment, Colorado. Vadose Zone Journal 10, 858-866.

Dove, P.M. (1995) Kinetic and thermodynamic controls on silica reactivity in weathering environments. Chemical Weathering Rates of Silicate Minerals 31, 235-290.

Dupré, B., Viers, J., Dandurand, J.-L., Polve, M., Bénézeth, P., Vervier, P. and Braun, J.-J. (1999) Major and trace elements associated with colloids in organic-rich river waters: ultrafiltration of natural and spiked solutions. Chemical Geology 160, 63-80.

Evans, C. and Davies, T.D. (1998) Causes of concentration/discharge hysteresis and its potential as a tool for analysis of episode hydrochemistry. Water Resources Research 34, 129-137.

Evans, M.J. and Derry, L.A. (2002) Quartz control of high germanium/silicon ratios in geothermal waters. Geology 30, 1019-1022.

Evans, M.J., Derry, L.A. and France-Lanord, C. (2004) Geothermal fluxes of alkalinity in the Narayani river system of central Nepal. Geochemistry Geophysics Geosystems 5.

Eyrolle, F., Benedetti, M.F., Benaim, J.Y. and Fevrier, D. (1996) The distributions of colloidal and dissolved organic carbon, major elements, and trace elements in small tropical catchments. Geochimica Et Cosmochimica Acta 60, 3643-3656.

Filippelli, G.M., Carnahan, J.W., Derry, L.A. and Kurtz, A. (2000) Terrestrial paleorecords of Ge/Si cycling derived from lake diatoms. Chemical Geology 168, 9-26.

Froelich, P.N., Blanc, V., Mortlock, R.A., Chillrud, S.N., Dunstan, W., Udomkit, A. and Peng, T.H. (1992) River fluxes of dissolved silica to the ocean were higher during glacials: Ge/Si in diatoms, rivers, and oceans. Paleoceanography 7, 739-767.

Froelich, P.N., Hambrick, G.A., Andreae, M.O., Mortlock, R.A. and Edmond, J.M. (1985) The Geochemistry of Inorganic Germanium in Natural-Waters. J Geophys Res-Oceans 90, 1133-1141.

Froelich, P.N. and Lesley, P. (2001) Tracing germanium contamination from coal-fired power plants down the Chattahoochee–Apalachicola River: implications for the toxic metalloids Arsenic and Selenium, Proceedings of the 2001 Georgia Water Resources Conference, University of Georgia, Athens, pp. 488-491.

Gable, D.J. (1980) The Boulder Creek batholith, Front Range, Colorado. US Government Printing Office.

Gable, D.J. and Johnson Jr, W. (1996) Mineralogy, geochemistry, metamorphism, and provenance of the Early Proterozoic metamorphic rocks of the central Front Range, Colorado. US Geological Survey.

Gebhart, K.A., Schichtel, B.A., Malm, W.C., Barna, M.G., Rodriguez, M.A. and Collett, J.L. (2011) Back-trajectory-based source apportionment of airborne sulfur and nitrogen concentrations at Rocky Mountain National Park, Colorado, USA. Atmospheric Environment 45, 621-633.

Gerard, F., Mayer, K.U., Hodson, M.J. and Ranger, J. (2008) Modelling the biogeochemical cycle of silicon in soils: Application to a temperate forest ecosystem. Geochimica Et Cosmochimica Acta 72, 741-758.

Hooper, R.P. (2003) Diagnostic tools for mixing models of stream water chemistry. Water Resources Research 39.

Hornberger, G.M., Scanlon, T.M. and Raffensperger, J.P. (2001) Modelling transport of dissolved silica in a forested headwater catchment: the effect of hydrological and chemical time scales on hysteresis in the concentration-discharge relationship. Hydrological Processes 15, 2029-2038.

Jepson, W.B. (1975) The Composition of Kaolinite—An Electron Microscope Microprobe Study. Clays and Clay Minerals 23, 310-317.

Iowa Environmental Mesonet (2016). "Boulder Wind Rose Plot (2012)". Retrieved 13 Jun 2016, from:http://mesonet.agron.iastate.edu/sites/windrose.phtml?station=BDU&network=CO_ASOS

Jones, L. and Handreck, K. (1965) Studies of silica in the oat plant. Plant and soil 23, 79-96.

Kennedy, V.C., Kendall, C., Zellweger, G.W., Wyerman, T.A. and Avanzino, R.J. (1986) Determination of the components of stormflow using water chemistry and environmental isotopes, Mattole River basin, California. Journal of Hydrology 84, 107-140.

Kirkwood, A.E., Shea, T., Jackson, L. and McCcauley, E. (2007) Didymosphenia geminata in two Alberta headwater rivers: an emerging invasive species that challenges conventional views on algal bloom development. Canadian Journal of Fisheries and Aquatic Sciences 64, 1703-1709.

Kurtz, A.C., Derry, L.A. and Chadwick, O.A. (2002) Germanium-silicon fractionation in the weathering environment. Geochimica Et Cosmochimica Acta 66, 1525-1537.

Kurtz, A.C., Lugolobi, F. and Salvucci, G. (2011) Germanium-silicon as a flow path tracer: Application to the Rio Icacos watershed. Water Resources Research 47.

Lovering, T.S.a.O.T. (1953) Geology and ore deposits of the Boulder County tungsten district, Colorado, in: Survey, U.S.G. (Ed.), Washington D.C., p. 199.

Lugolobi, F., Kurtz, A.C. and Derry, L.A. (2010) Germanium-silicon fractionation in a tropical, granitic weathering environment. Geochimica Et Cosmochimica Acta 74, 1294-1308.

Ma, J., Miyake, Y. and Takahashi, E. (2001) Silicon as a beneficial element for crop plants. Studies in plant Science 8, 17-39.

Ma, J.F., Tamai, K., Yamaji, N., Mitani, N., Konishi, S., Katsuhara, M., Ishiguro, M., Murata, Y. and Yano, M. (2006) A silicon transporter in rice. Nature 440, 688-691.

Markewitz, D. and Richter, D.D. (1998) The bio in aluminum and silicon geochemistry. Biogeochemistry 42, 235-252.

Martin, F., Ildefonse, P., Hazemann, J.L., Petit, S., Grauby, O. and Decarreau, A. (1996) Random distribution of Ge and Si in synthetic talc: An EXAFS and FTIR study. European Journal of Mineralogy 8, 289-299.

Mills, T.J., Anderson, S.P., Bern, C., Aguirre, A. and Derry, L.A. (2017) Colloid Mobilization and Seasonal Variability in a Semiarid Headwater Stream. J Environ Qual 46, 88-95.

Mortlock, R.A. and Froelich, P.N. (1996) Determination of germanium by isotope dilution hydride generation inductively coupled plasma mass spectrometry. Analytica Chimica Acta 332, 277-284.

Pokrovski, G.S. and Schott, J. (1998) Thermodynamic properties of aqueous Ge(IV) hydroxide complexes from 25 to 350 degrees C: Implications for the behavior of germanium and the Ge/Si ratio in hydrothermal fluids. Geochimica Et Cosmochimica Acta 62, 1631-1642.

Querol, X., Fernandezturiel, J.L. and Lopezsoler, A. (1995) Trace-Elements in Coal and Their Behavior during Combustion in a Large Power-Station. Fuel 74, 331-343.

Scanlon, T.M., Raffensperger, J.P. and Hornberger, G.M. (2001) Modeling transport of dissolved silica in a forested headwater catchment: Implications for defining the hydrochemical response of observed flow pathways. Water Resources Research 37, 1071-1082.

Sparks, J.P., Chandra, S., Derry, L.A., Parthasarathy, M.V., Daugherty, C.S. and Griffin, R. (2011) Subcellular localization of silicon and germanium in grass root and leaf tissues by SIMS: evidence for differential and active transport. Biogeochemistry 104, 237-249.

Stumm, W. and Morgan, J.J. (2012) Aquatic chemistry: chemical equilibria and rates in natural waters. John Wiley & Sons.

Trostle, K.D., Runyon, J.R., Pohlmann, M.A., Redfield, S.E., Pelletier, J., McIntosh, J. and Chorover, J. (2016) Colloids and organic matter complexation control trace metal concentration-discharge relationships in Marshall Gulch stream waters. Water Resources Research 52, 7931-7944.

U.S. Environmental Protection Agency Clean Air Markets Division, Clean Air Status and Trends Network (CASTNET), [Data tables accessed: Concentration – Weekly and Dry Deposition - Weekly], Available at www.epa.gov/castnet, Date accessed: [January 10, 2017].

U.S. Environmental Protection Agency (2013), 2011 National Emissions Inventory, U.S. EPA, Washington D.C.

CHAPTER THREE:

GERMANIUM-SILICON RATIOS AS A TRACER FOR METALLOID CONTAMINATION FROM A COAL FLY ASH SPILL IN THE DAN RIVER, NC

Abstract

The failure of a stormwater discharge pipe under the coal fly ash retention pond of the Dan River Steam Station released 39,000 tons of coal combustion residues (CCR) into the Dan River on February 2th, 2014. The release of heavily enriched metalloid CCR into this water body offered the opportunity to trace coal fly ash using Ge/Si ratios. Arsenic, Sb and Se become co-enriched with Ge in coal fly ash during the coal combustion process. However, Ge does not experience the strong adsorption behavior onto metal oxides that characterizes these other metalloids. Therefore, the conservative behavior of Ge in the aquatic environment facilitates the identification of CCR in receiving waters. During the spill, metalloid concentrations were well below the U.S. EPA maximum contaminant level (MCL). The only exception was Anglers Park where Sb reached 3.13 μg L^{-1} and Ge/Si spiked to 8.25 μmol mol^{-1}. This pattern was also observed in April where metalloid concentrations were low while Sb and Ge/Si increased sharply at Anglers Park. In subsequent sampling campaigns of May, July and October, anomalous Sb concentrations were observed for locations downstream form the Schoolfield Dam and as far as the Staunton River State Park. In May 13th, Sb concentrations for Anglers Park reached 36.4 μg L^{-1}. This is more than six times the MCL of Sb. There is not a Ge/Si spike for the samples with anomalous Sb but the ratio is well above the clean river average of 0.5 μmol mol^{-1}. This suggests that the increase in Sb may be due to processes in riverbed sediments post spill rather than new CCR

inputs because a Ge/Si spike is not observed. Mobilization of deposited fly ash along with bacterial reduction of Fe-oxides could be the dominant processes responsible for Sb anomalies in our dataset. These findings demonstrate the need for continued monitoring of CCR impacted streams long after spills are contained.

3.1 Introduction

The failure of a storm water pipe beneath a coal ash retention pond in the Dan River Steam Station caused the third largest spill of coal combustion residues (CCR) in the United Sates on February 2nd, 2014. The spill released approximately 39,000 tons of CCR and 27 million gallons of pond water into the Dan River of North Carolina and Virginia (EPA, 2017b; Lemly, 2015). CCR consists of fly ash, bottom ash, boiler slag and flue gas desulfurization products that are enriched in toxic metals like As, Sb, Se, Pb and Hg among others (Adriano et al., 1980). CCR is commonly stored in holding ponds near power plants or in landfills off-site (Ruhl et al., 2012). There is substantial chemical heterogeneity among coal sources that depends on plant constituents and paleoenvironmental conditions during coal formation (Vassilev and Vassileva, 1997). Additionally, power plants use blends of coals to power their boilers (Mastalerz et al., 2004). Consequently, this has posed challenges in identifying a chemical tracer of CCR that can be a reliable indicator of contamination. Boron isotopes have been used as tracers of CCR due to the consistently low $\delta^{11}B$ of coal materials (Davidson and Bassett, 1993; Ruhl et al., 2014; Williams and Hervig, 2004). However, the isotopic signature of coal ash leachate and contaminated stream water can overlap with $\delta^{11}B$ of clean groundwater and stream water (Davidson and Bassett, 1993; Ruhl et al., 2014).

Enrichment of ^{34}S in coal ash with respect to the parent coal can also be used as a tracer for coal ash contamination (Jiang et al., 2008). The degree of ^{34}S enrichment can vary from coal source and the burning process can influence the $\delta^{34}S$ of ash (Elswick et al., 2007). Stream water $\delta^{34}S$ is primarily controlled by dissolution of S bearing minerals in rocks during chemical weathering (Calmels et al., 2007). Therefore, the $\delta^{34}S$ range of regional lithology must be distinct from the coal fly ash released. Sulfur isotopes can be a promising tool to trace coal ash in streams, but this application is yet to be employed in these settings. Magnetic susceptibility assessments have been applied to trace fly ash deposition and sediment redistribution downstream from the Tennessee Valley Authority (TVA) and Dan River spill sites (Cowan et al., 2017; Cowan et al., 2015). The magnetic size fraction of ash can be as high as 17 wt. % and magnetic susceptibility (χ_{LF}) is strongly correlated with ash content in sediments (Cowan et al., 2017). Unfortunately, application of this technique can be challenging when ash has been buried and diluted by riverbed sediments. Lastly, the $\delta^{202}Hg$ signature in receiving waters was also measured during the TVA spill (Bartov et al., 2013). However, interpretation of this tracer can be challenging in some settings due to multiple sources of Hg from anthropogenic activity.

Considering some of the challenges posed by the tracers mentioned above, this study applies germanium-silicon ratios (Ge/Si) as a tracer of CCR to fingerprint contamination into the Dan River. Ge/Si ratios have been used before to understand the effects of CCR discharge into streams in Alabama and Georgia. Froelich and Lesley (2001) observed ratios downstream of coal-fired power plants to be orders of magnitude greater than upstream waters. Discharge of CCR into streams is permitted under the

National Pollution Discharge Elimination System established by the Clean Water Act (EPA, 2018). Therefore, locations downstream of these holding ponds are expected to exhibit an elevated Ge/Si fingerprint. Germanium is a trace element in the continental crust with an average concentration of 1.4 mg kg^{-1} (Bernstein, 1985; Rudnick and Gao, 2003). Ge forms an ideal solid solution with Si in the tetrahedral site of silicate minerals (Capobianco and Navrotsky, 1982). Substitution of Ge for Si is more extensive in silicates with few links between Si tetrahedra than with highly polymerized silicate structures (Bernstein, 1985). Therefore, Ge/Si ratios generally increase from quartz < feldspars < sheet silicates (Evans and Derry, 2002; Kurtz et al., 2002; Lugolobi et al., 2010). The average Ge/Si of continental silicates is approximately 1.4 μmol mol^{-1} (Froelich et al., 1992). Stream water is generally below the average continental silicate (ACS) ratio because Ge partitions into aluminosilicate clays during chemical weathering (Froelich et al., 1992). Therefore, stream water Ge/Si is generally < 1.4 μmol mol^{-1} and the average clean river Ge/Si is 0.5 μmol mol^{-1} (Baronas et al., 2016; Froelich et al., 1992). Coal fly ash contamination, hydrothermal activity and sulfide ore weathering are some of the few processes that can obscure this natural weathering signal (Anders et al., 2003; Evans and Derry, 2002; Froelich et al., 1985). These processes can result in significant increases in stream water Ge/Si. Germanium is enriched in coals with respect to the continental crust because of organo-metallic associations during coal formation (Bernstein, 1985). Typical concentrations for Ge in coals is 3-5 mg kg^{-1} compared to concentrations in the crust of 1.4 mg kg^{-1} (Bernstein, 1985; Rudnick and Gao, 2003). However, Ge concentrations in coal can vary widely as observed in hydrothermally altered coal with Ge concentrations exceeding 1000 mg kg^{-1} (Du et al.,

2009; Mastalerz et al., 2004). Coal fly ash is significantly more Ge enriched and concentrations can be up to six times higher than their source coals (Froelich and Lesley, 2001; Meij, 1994; Querol et al., 1995). The volatilization behavior during coal combustion for Ge and other metalloids (As, Sb and Se) are very similar. After volatilization, the metalloids condense onto the surfaces of coal fly ash particles (Meij, 1994). The smallest particles have the highest specific surface areas resulting in greater enrichment of metalloids in the smaller size fractions of ash (Meij, 1994; Querol et al., 1995). Despite the similar volatilization behavior of these metalloids, the geochemical behavior of Ge in the aquatic environment is drastically different from the others. Arsenic and antimony share similar electron configuration and form oxyanions of [III] to [V] oxidation states (Wilson et al., 2010). The oxyanions of [V] are most common across typical environmental pH ranges (4-9) for both metalloids. These species are less mobile in the aquatic environment due to charge associations with Fe oxyhydroxides and clays. In the case of Se, the dominant species have [IV] and [VI] oxidation states. In contrast to As and Sb, the more reduced species [IV] has greater charge associations with Fe oxyhydroxides (Plant et al., 2003). The advantage of the Ge/Si tracer is that Ge is less affected by co-precipitation with Fe oxyhydroxides (Chimenos et al., 2013, Scribner et al., 2006). The more conservative behavior of Ge in the aquatic environment presents this as a powerful tool to trace CCR during a spill. Therefore, the objectives of the study are to measure Ge/Si in the Dan River during and after the spill. Additionally, to compare the behavior of this tracer to dissolved concentrations of As, Sb and Se, which are co-enriched in CCR. Ge/Si and metalloid concentrations were monitored at various locations along the Dan River for 10 months after the spill to evaluate the

behavior of metalloids associated with ash deposited along the riverbed.

3.2 Site Description

3.2.1 Geology and climate

The Dan River originates in the eastern fringe of the Blue Ridge Mountains and flows east towards the coastal plain (Figure 3.1) (Weaver, 1996b). It is underlain by metamorphic and Triassic sedimentary rocks in the Eden, NC area. East of Eden and towards the plains, the river is underlain by meta-volcanic and granitic lithology (Rhodes and Conrad, 1985). Along the reach of the Dan River, there are no known sources of sulfide ore mineralization or hydrothermal activity. Therefore, Ge fluxes into streams should be dominated by weathering and CCR contamination. Climate is characterized by long, hot and humid summers with short mild winters. Most rainfall occurs during the warm summer months (Weaver, 1996a). Mean annual temperature is 14 ^{o}C and mean annual precipitation is 113 cm (NOAA, 2017). In 2014, precipitation was highest in the summer months with multiple precipitation events throughout the year (Figure 3.2a) (NOAA, 2017). Stream discharge at the USGS stream gauge near Wentworth, NC (USGS 02071000) showed peaks in discharge during the winter and spring. In the summer, discharge ranged between 20-30 m^3 sec^{-1} with minor peaks in discharge (Figure 3.2b).

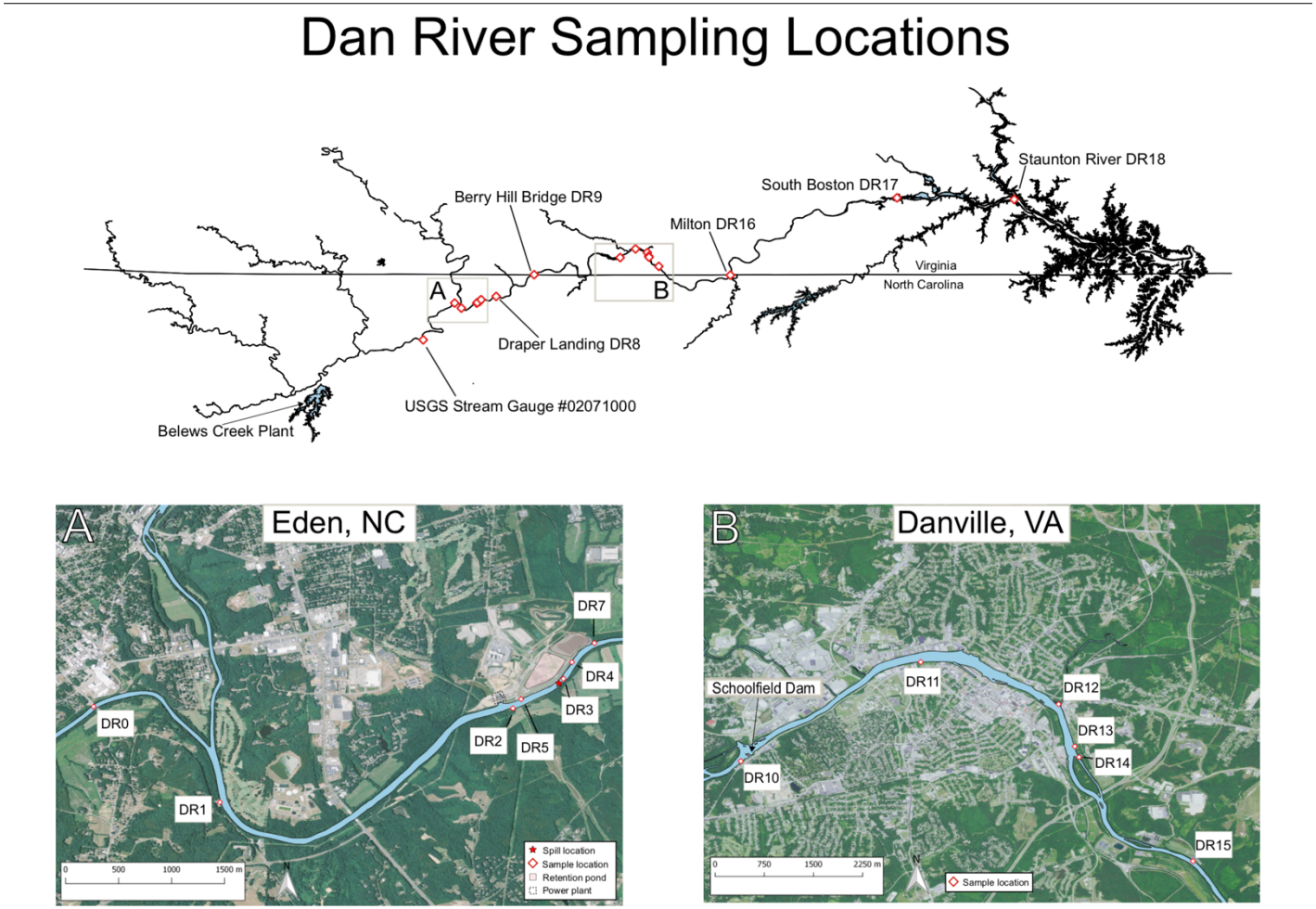

Figure 3.1: Map of the Dan River and sampling locations. Dan River sampling locations (red diamonds) along Eden, NC and Danville, VA.

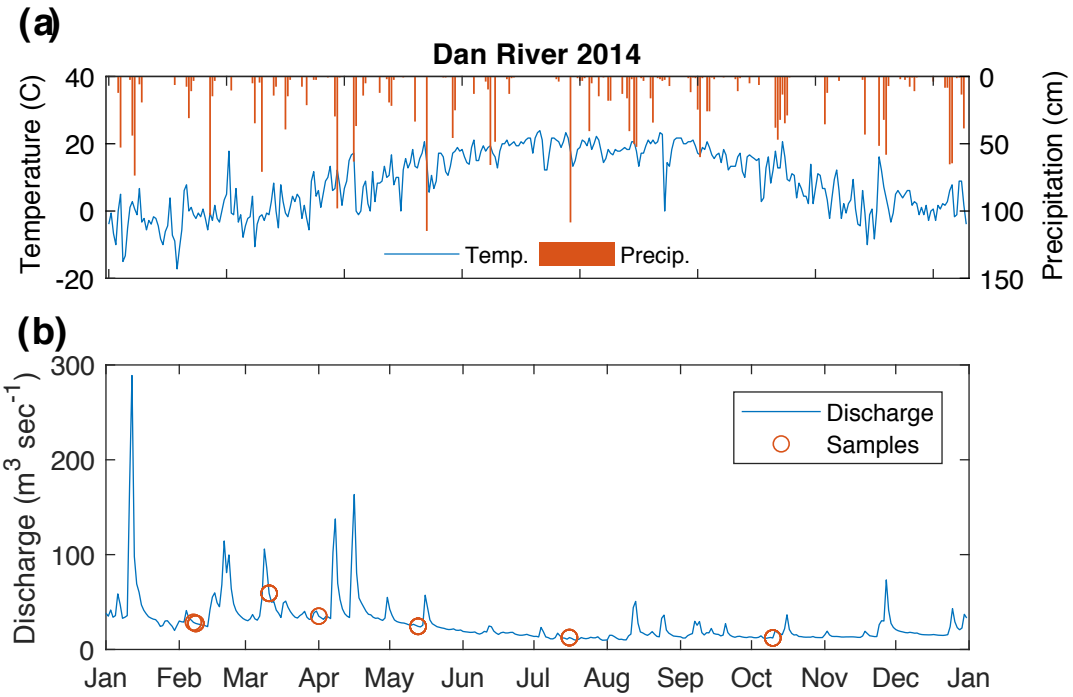

Figure 3.2: Weather conditions and discharge in the Dan River during 2014. **(a)** Temperature (blue) and precipitation (orange bar) for calendar year 2014 in Eden, NC. **(b)** Stream discharge for calendar year 2014 at the Dan River USGS stream gauge (#02071000) near Wentworth, NC. The orange circles represent the sample collection times.

3.2.2 Industrial discharge into the Dan River

There are multiple National Pollution Discharge Elimination System (NPDES) sites along the Dan River that have active or expired permits (NCDEQ, 2018a). Most sites permitted under NPDES are wastewater treatment plants (WWTP) that serve local municipalities. In addition to WWTP discharge, electric utilities like the Belews Creek and Dan River steam stations discharge retention pond effluent at rates of 0.39 and 0.04 m^3 sec^{-1} respectively (Ruhl et al., 2012). Therefore, background Ge/Si may account for both weathering fluxes of Ge and CCR inputs from upstream retention ponds like Belews Creek. In 2014, the Dan River, Smith River and Kerr Reservoir were included in the 2014 303(d) list of impaired waters (NCDEQ, 2014a; VDEQ, 2014). The Dan

River was impaired for fish consumption because of elevated water temperature, Hg and PCBs in fish tissue. In the Smith River, a tributary of the Dan River, water temperature and Cu concentrations impaired the river for fish consumption. The Dan River is in a setting of significant industrial activity. However, coal combustion and the discharge of CCR into the stream should be the primary activity that impacts Ge/Si dynamics.

3.3 Methods

3.3.1 Sample Collection

Following reports of the initial CCR release on February 2nd, 2014, stream water samples were collected during multiple sampling campaigns in 2014. In February, March and April, sampling included upstream sites (DR0, DR1) to obtain background element concentrations, near the location of the spill (DR3-7), downstream at Draper (DR8), Berry Hill (DR9) and several locations in Danville VA (DR11-15) (Figure 3.1). In the campaigns of May, July and October, samples were collected upstream (DR0, DR1), at Draper (DR8) and Berry Hill (DR9), several locations in Danville (DR10-DR15), and additional locations further downstream in Milton (DR16), South Boston (DR17), and Staunton River State Park (DR18). Samples were collected at boat ramps and other accessible points along the river; sampling locations near the coal ash retention ponds were accessed by canoe.

Stream samples were filtered with a 0.45 μm cellulose filter and stored in acid-washed low-density poly-ethylene bottles (LDPE). The < 0.45 μm filtered fraction is the focus of this study and will be considered the dissolved fraction henceforth. Prior to

sample collection, field parameters (pH, temperature, dissolved oxygen, specific conductance) were measured in situ in the river with a multi-meter (Hanna 9828) (Table 3.1). A coal ash sample was collected on the riverbank adjacent to the failed storm water pipe on February 9th, 2014. The ash sample was freeze dried and stored for further analysis.

3.3.2 Sample Analysis

Water samples were analyzed using inductively coupled plasma optical emission spectroscopy (ICP-OES; AMETEK SpectroBlue) at Cornell University to determine major cation concentrations (Table 3.1). Analysis of arsenic, antimony and germanium were conducted using hydride-generation ICP-mass spectrometry (Mortlock and Froelich, 1996) (Table 3.2). Arsenic concentrations were determined using an ion exchange column for As speciation (Elemental Scientific, CF-KIT-As35). After passing through the column, the separated fractions were introduced into the hydride system coupled online to a Thermo-Finnigan Element 2 ICP-MS. The chromatographic peak areas were integrated using the program *A Pragmatic Introduction to Signal Processing* available online (O'Haver, 2018). Total As is therefore the sum of all measured arsenic species. The inorganic As species with oxidation state of [V] was by far the dominant species measured. Antimony concentrations were determined by measuring both Sb[III] and Sb[V] in stream samples. Speciation is done by selective reduction of Sb species in controlled pH.

Table 3.1: Field parameters and major elements in Dan River.

ID_Month	Date	Distance From Spill km	pH	DO mg L^{-1}	SC uS cm^{-1}	T C°	Na mg L^{-1}	Mg mg L^{-1}	K mg L^{-1}	Ca mg L^{-1}	Al mg L^{-1}	Si mg L^{-1}	Cl^{-} mg L^{-1}	SO^{-4} mg L^{-1}	DOC mg L^{-1}
Dan River Gauge	2/8/2014	-25.3	7.5	nd	nd	nd	3.75	2.59	1.34	7.37	0.04	7.06	nd	nd	nd
DR0_2	2/7/2014	-7.1	7.7	nd	nd	nd	3.87	2.58	1.34	7.32	0.08	7.15	nd	nd	nd
DR1_2	2/7/2014	-4.7	nd	nd	nd	nd	3.84	2.48	1.39	7.20	0.06	7.11	nd	nd	nd
DR8_2	2/7/2014	4.1	7.6	nd	nd	nd	4.24	2.56	1.35	7.06	0.05	7.12	nd	nd	nd
DR11_2	2/8/2014	47.4	7.5	nd	nd	nd	5.29	2.67	1.53	7.08	0.19	7.33	nd	nd	nd
DR12_2	2/8/2014	50.2	7.7	nd	nd	nd	5.37	2.44	1.56	6.47	0.14	7.83	nd	nd	nd
DR13_2	2/8/2014	51.1	7.7	nd	nd	nd	5.70	2.57	1.59	6.71	0.08	7.88	nd	nd	nd
DR14_2	2/8/2014	51.3	7.6	nd	nd	nd	5.64	2.55	1.60	6.74	0.14	7.93	nd	nd	nd
DR15_2	2/8/2014	54.6	7.8	nd	nd	nd	14.88	2.69	2.01	7.96	0.13	7.60	nd	nd	nd
DR1_3	3/11/2014	-4.7	7.1	12.00	56.30	8.80	4.13	2.53	1.97	6.30	0.70	6.96	8.86	6.38	1.61
DR2_3	3/11/2014	-0.7	7.0	12.50	27.00	8.80	4.61	2.44	1.91	6.21	0.43	6.61	8.49	6.26	1.52
DR3_3	3/11/2014	0.1	7.4	12.50	57.70	9.30	4.92	2.51	1.81	6.04	0.48	6.92	7.33	5.92	1.33
DR4_3	3/11/2014	0.2	7.4	12.60	57.70	9.30	4.70	2.55	1.98	6.24	0.51	6.84	7.96	6.14	1.67
DR6_3	3/11/2014	0.3	7.4	12.20	57.90	9.40	4.79	2.46	1.90	6.11	0.41	6.74	7.52	6.03	1.83
DR8_3	3/11/2014	4.1	7.3	11.80	56.90	9.40	4.85	2.53	1.92	6.10	0.66	7.13	7.95	6.19	2.09
DR9_4	4/1/2014	15.9	nd	nd	nd	nd	5.09	2.43	1.71	6.33	0.15	6.07	7.40	6.26	1.86
DR10_4	4/1/2014	43.4	6.7	9.59	28.00	11.20	4.83	2.35	1.54	6.24	0.09	6.02	6.50	5.65	1.78
DR15_4	4/1/2014	54.6	7.5	nd	136.00	13.13	25.97	2.53	2.11	6.99	0.12	6.18	37.11	7.59	1.92
DR1_5	5/13/2014	-4.7	6.2	7.75	69.00	22.09	14.06	3.65	2.36	9.32	0.01	7.06	11.80	6.50	1.57
DR8_5	5/13/2014	4.1	7.4	8.51	63.00	21.14	14.71	3.38	2.36	8.55	0.02	6.73	8.50	6.00	1.72
DR9_5	5/13/2014	15.9	6.7	8.28	70.00	22.02	31.32	3.29	3.12	8.59	0.01	7.04	9.50	6.30	1.84
DR10_5	5/13/2014	43.4	6.8	8.56	69.00	23.45	6.03	3.31	1.98	8.07	0.02	6.94	9.90	6.50	2.35

continued on next page

Table 3.1 (*continued*)

ID_Month	Date	Distance From Spill km	pH	DO mg L^{-1}	SC uS cm^{-1}	T C^{o}	Na mg L^{-1}	Mg mg L^{-1}	K mg L^{-1}	Ca mg L^{-1}	Al mg L^{-1}	Si mg L^{-1}	Cl^{-} mg L^{-1}	SO^{-4} mg L^{-1}	DOC mg L^{-1}
DR11_5	5/13/2014	47.4	6.7	9.06	69.00	22.95	5.55	3.44	1.94	8.48	0.01	6.94	9.80	6.60	1.73
DR15_5	5/13/2014	54.6	7.7	10.59	176.00	24.41	4.95	3.16	1.79	7.85	0.01	6.72	52.00	8.50	2.15
DR16_5	5/13/2014	74.5	7.2	8.53	86.00	23.63	4.31	3.78	1.80	9.85	0.02	6.87	15.70	7.20	1.93
DR17_5	5/13/2014	126.4	7.0	7.84	76.00	24.54	4.71	3.78	2.21	10.01	0.24	7.51	11.30	6.60	1.99
DR18_5	5/13/2014	153.5	6.9	8.75	74.00	27.41	6.42	3.24	2.05	7.35	0.03	6.98	10.20	6.40	2.88
DR1_7	7/16/2014	-4.7	7.1	6.96	116.00	26.14	13.36	3.21	2.27	7.46	0.01	6.79	12.95	5.39	2.01
DR8_7	7/16/2014	4.1	7.0	7.69	101.00	26.07	14.84	3.32	2.33	8.02	0.02	6.80	8.20	5.04	1.94
DR10_7	7/16/2014	43.4	6.8	6.51	106.00	26.98	15.60	3.23	2.35	7.97	0.04	6.83	9.74	5.33	2.15
DR11_7	7/16/2014	47.4	7.0	6.95	109.00	27.13	5.75	3.27	1.96	8.07	0.05	6.66	9.79	5.34	2.13
DR15_7	7/16/2014	54.6	7.5	8.11	164.00	28.36	5.72	3.15	1.89	7.77	0.03	6.39	22.66	6.69	1.99
DR16_7	7/16/2014	74.5	7.4	7.03	168.00	28.11	5.75	2.96	1.88	7.16	0.37	6.82	21.50	6.47	1.96
DR17_7	7/16/2014	126.4	7.2	7.03	153.00	27.86	4.18	3.38	1.73	8.89	0.02	5.87	18.24	6.15	2.00
DR18_7	7/16/2014	153.5	7.8	8.54	122.00	30.54	7.76	2.91	2.00	7.31	0.39	7.22	9.06	6.00	2.97
DR0_10	10/10/2014	-7.1	6.4	9.60	155.00	17.27	8.83	3.23	1.96	7.90	0.54	7.64	14.09	6.95	1.80
DR1_10	10/10/2014	-4.7	7.2	8.14	156.00	17.54	10.24	3.19	1.91	8.44	0.25	7.00	14.50	6.59	1.60
DR8_10	10/10/2014	4.1	7.2	9.05	147.00	16.53	32.90	3.20	2.82	9.20	0.13	7.18	9.17	6.40	1.67
DR10_10	10/10/2014	43.4	7.4	7.27	157.00	18.81	5.48	3.14	1.57	8.38	0.15	6.53	10.80	6.75	1.77
DR11_10	10/10/2014	47.4	7.7	8.52	159.00	18.28	5.47	3.07	1.60	8.13	0.10	6.68	10.41	6.92	1.79
DR15_10	10/10/2014	54.6	7.6	9.24	262.00	18.83	5.61	3.06	1.67	8.16	0.13	6.91	49.10	10.76	2.34
DR16_10	10/10/2014	74.5	7.5	7.63	193.00	19.59	5.39	2.96	1.74	7.55	0.14	6.86	22.57	9.34	1.85
DR17_10	10/10/2014	126.4	7.4	9.72	191.00	19.92	4.88	3.12	1.55	8.67	0.13	6.88	23.67	8.77	1.70
DR18_10	10/10/2014	153.5	7.5	7.70	179.00	20.15	11.12	3.55	2.35	8.41	0.14	7.33	17.09	8.33	2.05

nd = not determined

Table 3.2: Metalloid concentrations in the Dan River.

Sample ID_Month	Date	Distance from Spill km	pH	As µg L^{-1}	Sb µg L^{-1}	Se µg L^{-1}	Ge µg L^{-1}	Ge/Si µmol mol^{-1}	Sb/As wt. wt^{-1}
USGS Gauge (#02071000)	2/8/2014	-25.32	7.5	0.06	0.03	0.07	0.05	2.53	0.53
DR0_2	2/7/2014	-7.06	7.7	0.06	0.02	0.06	0.04	2.37	0.36
DR1_2	2/7/2014	-4.74	nd	0.06	0.03	0.06	0.04	2.16	0.45
DR8_2	2/7/2014	4.05	7.6	0.14	0.05	0.06	0.04	1.96	0.35
DR11_2	2/8/2014	47.4	7.5	0.46	0.09	0.06	0.04	2.22	0.18
DR12_2	2/8/2014	50.24	7.7	0.33	0.07	0.05	0.03	1.41	0.21
DR13_2	2/8/2014	51.06	7.7	0.32	0.07	0.05	0.03	1.27	0.21
DR14_2	2/8/2014	51.32	7.6	0.35	0.07	0.05	0.03	1.41	0.19
DR15_2	2/8/2014	54.6	7.8	0.43	3.13	0.33	0.16	8.25	7.36
DR1_3	3/11/2014	-4.74	7.1	0.08	0.08	0.04	0.05	2.61	1.00
DR2_3	3/11/2014	-0.65	7.0	0.09	0.08	0.04	0.04	2.32	0.88
DR3_3	3/11/2014	0.05	7.4	0.04	0.10	0.03	0.03	1.79	2.64
DR4_3	3/11/2014	0.22	7.4	0.06	0.11	0.04	0.04	2.14	1.73
DR6_3	3/11/2014	0.25	7.4	0.08	0.12	0.04	0.03	1.73	1.40
DR8_3	3/11/2014	4.05	7.3	nd	0.08	0.04	0.04	2.22	nd
DR9_4	4/1/2014	15.9	nd	nd	0.16	0.03	0.02	1.39	nd
DR10_4	4/1/2014	43.36	6.7	nd	0.11	0.04	0.02	1.54	nd
DR15_4	4/1/2014	54.6	7.5	nd	3.00	0.26	0.13	8.09	nd
DR1_5	5/13/2014	-4.74	6.2	0.20	0.03	0.07	0.06	3.06	0.16
DR8_5	5/13/2014	4.05	7.4	0.19	0.12	0.05	0.04	2.06	0.66
DR9_5	5/13/2014	15.9	6.7	0.30	0.12	0.08	0.05	2.59	0.39
DR10_5	5/13/2014	43.36	6.8	0.25	0.07	0.07	0.04	2.43	0.26

continued on next page

Table 3.2 (*continued*)

Sample ID_Month	Date	Distance from Spill km	pH	As µg L^{-1}	Sb µg L^{-1}	Se µg L^{-1}	Ge µg L^{-1}	Ge/Si µmol mol^{-1}	Sb/As wt. wt^{-1}
DR11_5	5/13/2014	47.4	6.7	0.33	0.06	0.07	0.04	2.45	0.19
DR15_5	5/13/2014	54.6	7.7	0.32	36.4	1.43	0.04	2.06	112
DR16_5	5/13/2014	74.51	7.2	0.27	6.03	0.16	0.04	2.04	22.2
DR17_5	5/13/2014	126.44	7.0	0.22	1.35	0.17	0.03	1.53	6.20
DR18_5	5/13/2014	153.52	6.9	0.42	0.12	0.06	0.03	1.48	0.28
DR1_7	7/16/2014	-4.74	7.1	0.29	0.03	0.05	0.06	3.28	0.12
DR8_7	7/16/2014	4.05	7.0	0.40	0.14	0.05	0.03	1.51	0.36
DR10_7	7/16/2014	43.36	6.8	0.40	0.12	0.06	0.04	2.31	0.31
DR11_7	7/16/2014	47.4	7.0	0.43	0.14	0.06	0.04	2.44	0.31
DR15_7	7/16/2014	54.6	7.5	0.49	4.58	0.56	0.04	2.26	9.27
DR16_7	7/16/2014	74.51	7.4	0.27	6.16	0.25	0.03	1.98	22.9
DR17_7	7/16/2014	126.44	7.2	0.45	3.59	0.12	0.03	1.72	7.98
DR18_7	7/16/2014	153.52	7.8	0.45	2.93	0.06	0.03	1.54	6.44
DR0_10	10/10/2014	-7.06	6.4	0.24	0.12	0.09	0.09	4.38	0.49
DR1_10	10/10/2014	-4.74	7.2	0.44	0.03	0.08	0.09	4.78	0.07
DR8_10	10/10/2014	4.05	7.2	0.36	0.09	0.05	0.04	2.31	0.24
DR10_10	10/10/2014	43.36	7.4	0.14	0.08	0.06	0.05	2.73	0.57
DR11_10	10/10/2014	47.4	7.7	0.17	0.11	0.06	0.04	2.44	0.65
DR15_10	10/10/2014	54.6	7.6	0.64	2.33	0.09	0.03	1.93	3.63
DR16_10	10/10/2014	74.51	7.5	0.17	0.94	0.07	0.04	2.29	5.68
DR17_10	10/10/2014	126.44	7.4	0.16	1.99	0.10	0.04	1.99	12.5
DR18_10	10/10/2014	153.52	7.5	0.20	0.91	0.11	0.03	1.35	4.64

nd = not determined

At near neutral pH, Sb[III] species are selectively reduced by 4% $NaBH_4$ to form a volatile hydride that is transported by argon gas into the ICP-MS. At pH ≈1 with the addition of iodide, Sb[III] and Sb[V] species are reduced and Sb[V] is calculated by difference (Andreae et al., 1981). Sb[III] was below detection (0.005 $\mu g\ L^{-1}$) for all samples. Therefore, total Sb represents only Sb[V] species. Total selenium was measured using hydride generation without speciation. An enriched ^{70}Ge tracer solution (spike) was added to the water samples and equilibrated for at least 24 hours at 60 °C. Germanium was quantified both by a standard curve method and isotope dilution using the $^{70}Ge/^{74}Ge$ ratio. Corrections for mass bias and signal drift were done using sample-standard bracketing. At the same time, response curves were established by analysis of Ge standards at 0.005, 0.02, 0.05, 0.10, 0.20 and 0.50 $\mu g\ L^{-1}$. Results from isotope dilution calculations were cross-checked against the standard response curves measured at m/z =74. With ($^{70}Ge/^{74}Ge$) spike = 162 the spike contribution to m/z 74 is negligible.

The coal fly ash sample was prepared for wet chemical analysis using the fusion method. First, the ash was ignited in a muffle furnace at 900 °C and then weighed to determine loss on ignition (LOI). The LOI mass was used to calculate oxide and metalloid concentrations. A flux with a 1:1 ratio of lithium tetraborate and lithium metaborate was mixed with the sample in a ratio of 8:1. This flux and sample mixture was heated in the furnace at 1050 °C to form a glass bead. The bead was poured into 50 ml of 10% HNO_3 and shaken overnight until the glass completely dissolved. The solutions were diluted to 2% HNO_3 and analyzed for major elements and trace elements using ICP-OES and ICP-MS.

3.4 Results

3.4.1 Retention pond effluent and ash slurry

Five weeks after the spill, two samples (DR5_3 and DR7_3) were collected from drainage of the Dan River Steam Station coal ash retention ponds (Figure 3.1). CCR effluent are discharged into tributaries to the Dan River. Therefore, these samples most closely resemble the CCR discharged into the river during the February spill. These samples had concentrations of As and Sb that surpassed or approached the EPA maximum contaminant level (MCL) of 10 and 6 μg L^{-1} respectively (Table 3.3). Sample DR5_3 is 500 meters upstream from the location of the February spill at a storm water discharge outflow (Figure 3.1). Arsenic and Sb reached 47.9 and 3.18 μg L^{-1} respectively while Se was lower at 0.78 μg L^{-1}. This sample had the largest measured Ge/Si ratio of the study with 709 μmol mol^{-1}. At 0.85 km downstream from the storm water discharge outflow, sample DR7_3 had As and Sb concentrations of 1.26 and 2.29 μg L^{-1} respectively. DR7_3 was sampled at a tributary to the Dan River that drains the second retention pond. In comparison to DR5_3, selenium decreased to 0.63 μg L^{-1} and Ge/Si was 187 μmol mol^{-1}. The pond effluents fall in the range of coal ash effluents as described by Froelich and Lesley (2001) (Figure 3.3). At about 600-750 meters from DR5_3, the Dan River stream samples of DR3_3 and DR4_3 had metalloid concentrations significantly lower than the CCR effluent (Table 3.2).

Table 3.3: Retention pond effluent

Sample ID_Month	Date Collected	pH	Na mg L^{-1}	Mg mg L^{-1}	K mg L^{-1}	Ca mg L^{-1}	Al mg L^{-1}	Si mg L^{-1}	Fe mg L^{-1}	Ge µg L^{-1}	As µg L^{-1}	Sb µg L^{-1}	Se µg L^{-1}	Ge/Si µmol mol^{-1}	Sb/As wt wt^{-1}
DR5	3/11/2014	6.9	19.3	13.9	8.02	70.7	0.07	7.70	5.9	14.1	47.9	3.18	0.78	709	0.07
DR7	3/11/2014	7.1	7.16	2.74	1.72	7.94	0.21	6.31	0.19	3.05	1.26	2.29	0.63	187	1.82

Table 3.4: Coal ash slurry

Sample	Date Collected	Na_2O wt. %	MgO wt. %	K_2O wt. %	CaO wt. %	Al_2O_3 wt. %	SiO_2 wt. %	Fe_2O_3 wt. %	Total wt. %	Ge mg kg^{-1}	As mg kg^{-1}	Sb mg kg^{-1}	Se mg kg^{-1}	Ge/Si µmol mol^{-1}	Sb/As wt wt^{-1}
Ash Slurry	2/9/2014	0.94	1.03	3.02	1.13	18.42	68.73	5.19	98.45	4.43	23.24	2.95	-	5.34	0.13

However, Ge/Si was above the clean river Ge/Si with 1.79 and 2.14 μmol mol^{-1} respectively. Despite the proximity of DR3_3 and DR4_3 to the retention pond drainage, metalloid concentrations are below the MCL. This indicates that lateral mixing in the Dan River is quite limited near the retention ponds and at locations downstream. This observation agrees with CCR transport modelling during the spill that suggests that CCR travelled along the riverbank until fully mixing at the Schoolfield reservoir (Figure 3.1) (Jia et al., 2016).

A coal ash slurry collected adjacent to the failed storm water pipe was analyzed for bulk chemistry and metalloid concentration (Table 3.4). Additionally, scanning electron microscopy (SEM) was used to image coal ash particles in the slurry (Figure 3.4a). The ash cenospheres contain crystallites on the surface of the particle. Using electron dispersive spectroscopy (EDS), these crystallites were found to be enriched in Fe and Ti (Figure 3.4b). The Fe oxyhydroxides on the surface of the ash particles are ideal mineral surfaces for metalloid adsorption. The Ge/Si ratio of the ash sample was 5.34 μmol mol^{-1} with a Ge, As and Sb concentration of 4.43, 23.2 and 2.95 mg kg^{-1} respectively. The Ge/Si ratio of the coal ash slurry is much lower than the pond effluent. Germanium is effectively leached from coal ash in oxidizing environments (Chimenos et al., 2013). Therefore, it is not surprising that retention pond effluent has higher Ge/Si ratios than the ash slurry discharged from the ponds.

The Sb/As per weight ratios for the ash slurry, DR5_3 and DR7_3 are 0.13, 0.07 and 1.82 respectively. Metalloid concentrations in retention pond outflow from facilities in North Carolina have an average Sb/As of 0.23 (std. ± 0.09) (Ruhl et al., 2012). In previous studies, the Dan River outflow had an Sb/As ratio of 0.15 (Ruhl et al., 2014),

similar to the ratio of the ash slurry and DR5_3. The coal ash effluents and the slurry provide a characterization of the CCR spilled into the Dan River. U.S. EPA and NC-

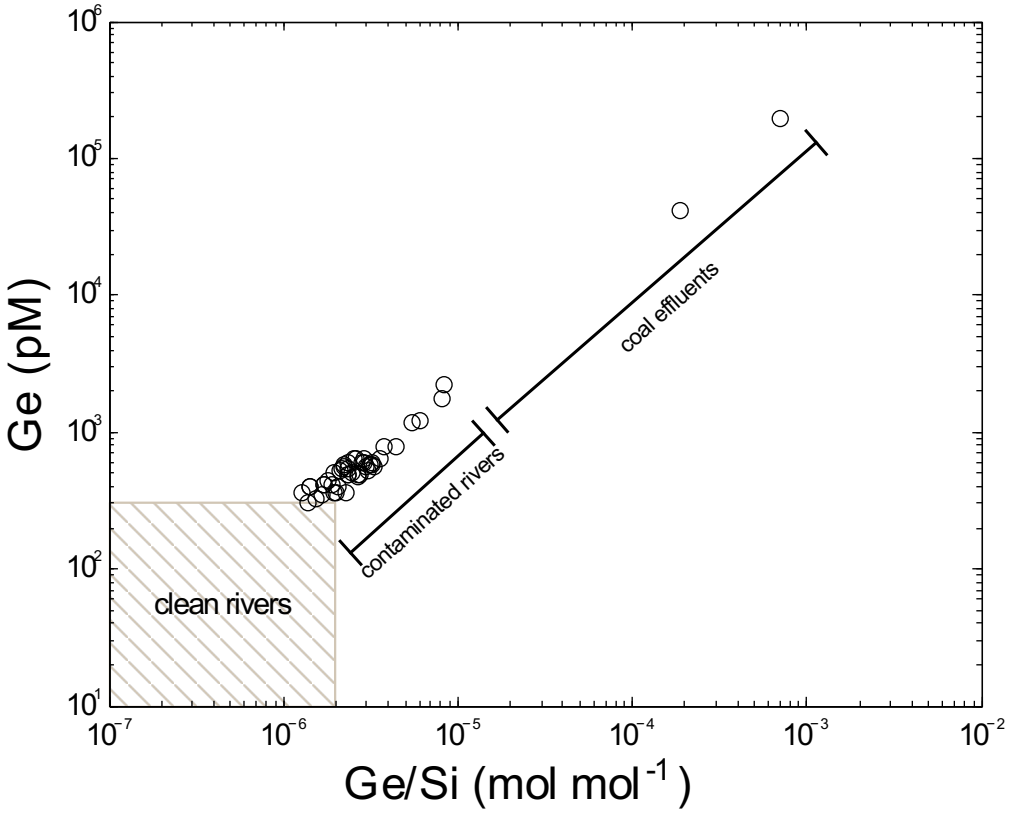

Figure 3.3: Ge to Ge/Si plot of Dan River stream samples and CCR effluents. Log-Log plot of Ge and Ge/Si of the Dan River stream water samples and retention pond effluents. Dan River stream water data form an array between 200-2,000 pM Ge. This range is characteristic of CCR contaminated receiving waters as described by Froelich and Lesley (2001). The two more concentrated samples of DR7_3 and DR5_3 have Ge concentrations in the range of CCR effluents.

DEQ data demonstrate significant variability in chemistry of CCR (EPA, 2017a; NCDEQ, 2014c). However, the results from our ash slurry and coal ash effluent are of the same magnitude as reported by these government agencies. Most importantly, the Ge/Si fingerprint of the source material have been characterized and are consistent with elevated ratios higher than the clean river Ge/Si.

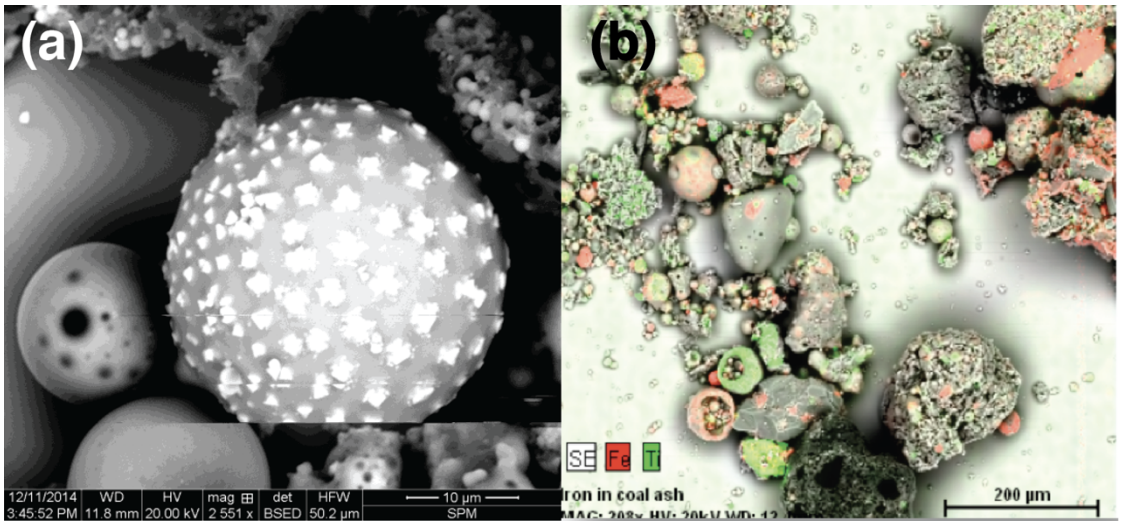

Figure 3.4: Coal ash slurry SEM and EDS results. (a) SEM image of a coal ash cenosphere covered by Fe crystallites. (b) EDS image of Fe (red) and Ti (green) enrichment in the coal ash slurry. Analysis performed by R. Serra-Maia.

3.4.2 Dan River metalloid concentrations

Dissolved metalloid concentrations of As, Sb and Se in stream water during the spill were below the U.S. EPA MCL of 10, 6 and 50 μg L^{-1} respectively (Figure 3.5a, b & c, Table 3.2). This is consistent with concentrations reported by the U.S. EPA and NC-DEQ for samples collected during the spill (EPA, 2014; NCDEQ, 2014b). Arsenic concentrations increased from 0.06 to 0.43 μg L^{-1} between the Dan River stream gauge (USGS #02071000) and DR15_2. This is approximately 55 km downstream from the spill. Arsenic concentrations were well below the EPA MCL but increase with distance from the spill. Antimony was less than 0.10 μg L^{-1} for most samples but sharply increased to 3.13 μg L^{-1} at DR15_2. Selenium was also less than 0.10 μg L^{-1} but increased less abruptly to 0.33 μg L^{-1} at DR15_2. Overall, the samples collected during the spill had As and Se concentrations below 1.0 μg L^{-1}. Samples had Sb concentrations less than 0.10 μg L^{-1} except for the spike at Anglers Park (DR15_2) of 3.13 μg L^{-1}.

The second sampling campaign on March focused upstream (DR1_3 & DR2_3) and downstream (DR3_3-DR8_3) of the coal ash retention ponds of the Dan River Steam Station. The samples upstream from the spill (DR1_3 & DR2_3) had As, Sb and Se concentrations below 0.10 μg L^{-1} (Figure 3.5e, f and g). Downstream from the spill (DR3_3, DR4_3, DR6_3 and DR8_3), metalloid concentrations did not differ drastically from upstream samples (DR2_3 and DR3_3) and ranged between 0.03 to 0.12 μg L^{-1}.

In April, sample collection began at the Berry Hill bridge (DR9_4) on the North Carolina-Virginia state line (Figure 3.1). Two additional samples were collected at Abreu Grogan Park (DR10_4) and Anglers Parks (DR15_4) in Danville, VA. Arsenic in these samples was below the limit of detection (0.005 μg L^{-1}) while Se was less than 0.30 μg L^{-1}. Antimony from DR9_4 to DR10_4 was less than 0.20 μg L^{-1} except for Anglers Park (DR15_4) at 3.0 μg L^{-1}. Similar to February, samples from March and April are generally below the MCL. However, DR15 continued to have significantly higher Sb concentrations than samples upstream.

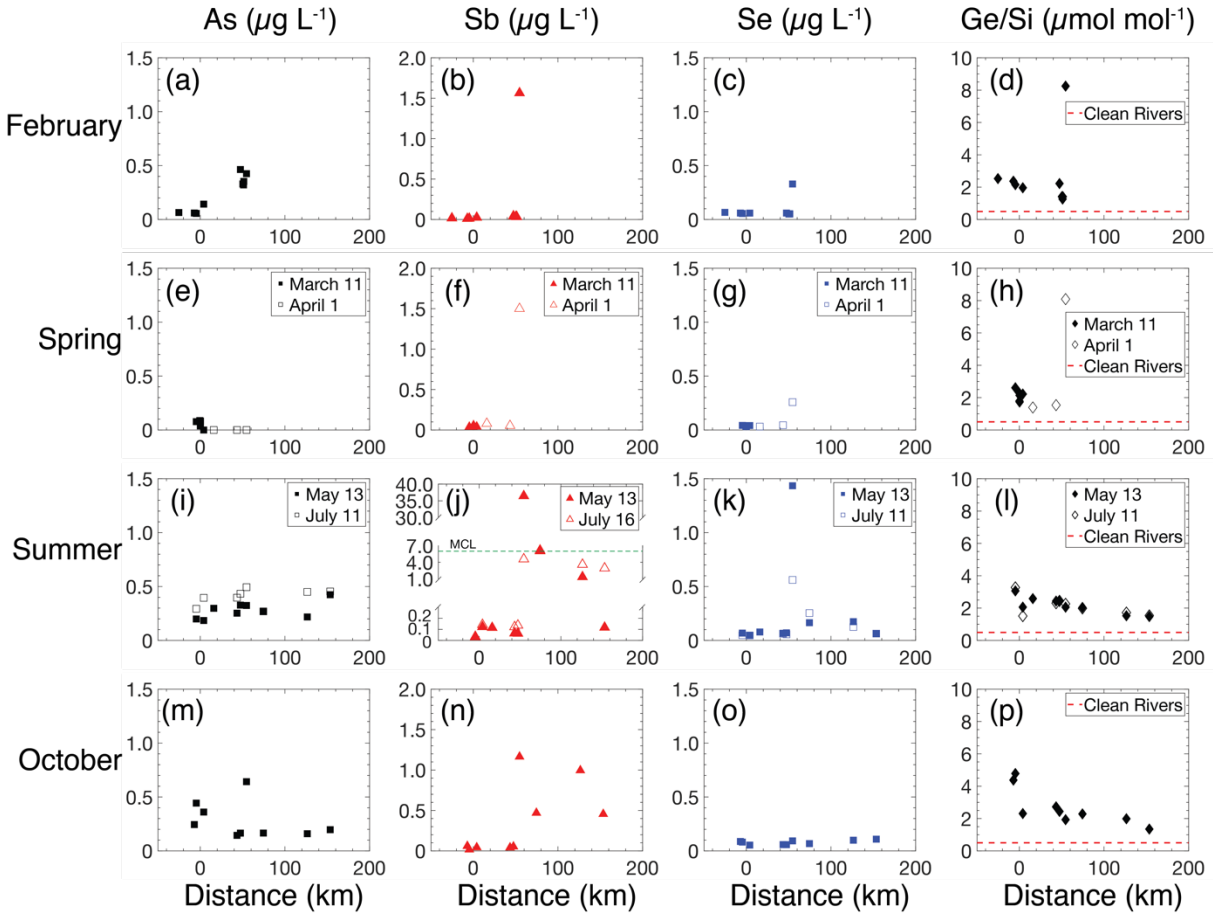

Figure 3.5: Dan River metalloid concentrations and Ge/Si ratios. Concentration of As, Sb, Se and Ge/Si ratios over distance from the failed stormwater pipe. Zero kilometers on the figures represents the location of the spill. Samples with a negative distance are upstream from the failed pipe. For the Ge/Si to distance plots, the red dashed line represents the average clean river Ge/Si of 0.5 μmol mol^{-1} (Froelich et al.,1992; Baronas et al., 2016)

In the summer months of May and July, samples were taken at the same locations and further downstream at Milton (DR16), South Boston (DR17), and Staunton River State Park boat ramp (DR18) (Figure 3.1). In May, arsenic concentrations slightly increase from DR1_5 (0.20 μg L^{-1}) to DR18_5 (0.42 μg L^{-1}) (Figure 3.5i). In July, arsenic concentrations along the river show a similar pattern and are less than 0.50 μg L^{-1}. Antimony had multiple peak concentrations at DR15, DR16 and DR17 for both sampling dates (Figure 3.5j). DR15_5 in May reached the highest level at 36.4 μg L^{-1} above the EPA MCL by a factor of six. Selenium was also anomalously high at DR15_5 with a concentration of 1.43 μg L^{-1}. This is the highest Se concentration measured in this study. In May, samples collected further downstream at DR16_5 and DR17_5 had Sb concentrations of 6.03 and 1.35 μg L^{-1} respectively. In July, DR15_7 decreased to 4.58 μg L^{-1} while samples downstream ranged between 6.16 and 2.93 μg L^{-1}. In this summer period, arsenic and selenium continued to be below toxic levels in the river with concentrations below 0.50 μg L^{-1}. In the other hand, antimony surpassed the MCL by a factor of six and samples downstream maintained concentrations in the μg L^{-1} range. Antimony concentrations from DR16 through DR18 do not exceed the MCL but remain above 1.0 μg L^{-1} standing in sharp contrast to the samples near the retention ponds.

During October, sampling collection was focused on the same locations of May and July. Arsenic concentrations show more scatter without an increase in concentration from DR0_10 to DR18_10 (Figure 3.5m). Once again, the sharpest contrast is observed in Sb at the sites more than 50 km downstream from the retention ponds. From DR0_10

to DR11_10, Sb concentrations range between 0.03-0.12 μg L^{-1} before increasing to 2.33 μg L^{-1} at Anglers Park (DR15_10). Sb remains above 0.90 μg L^{-1} from DR16_10 to DR18_10 (Figure 3.5n). Selenium concentration are below 0.12 μg L^{-1} and do not show an increasing trend from DR0_10 to DR18_10. The MCL for Sb was not exceeded, however concentrations between DR15_10 and DR18_10 sharply increase from 0.03 to 2.33 μg L^{-1}.

3.4.3 Dan River Ge/Si patterns

The Ge/Si ratio in February is near constant from the USGS stream gauge (2.53 μmol mol^{-1}) to DR11_2 (2.22 μmol mol^{-1}) (Figure 3.5d). Ge/Si is above the clean river ratio of 0.5 μmol mol^{-1} for a river distance of 75 km (USGS gauge to DR11). In Dan Daniel Memorial Park (DR12_2-DR14_2), the ratio decreases to a range of 1.27-1.41 μmol mol^{-1}. At 3.3 km downstream from DR14_2, Ge/Si increases to 8.25 μmol mol^{-1} at the Anglers Park boat ramp (DR15_2). Ge/Si has a decreasing trend from DR0_2 to DR14_2 (2.37 to 1.41 μmol mol^{-1}). However, Ge/Si ratio spikes in Anglers Park (DR15_2) where Sb and Se dramatically increase.

The following campaign of March shows similar Ge/Si ratios for locations in Eden, NC (DR1_3-DR8_3) (Figure 3.5h). The samples cluster between 1.73-2.22 μmol mol^{-1} and are well above the clean river ratio. Metalloid concentrations during March are some of the lowest measured (<0.15 μg L^{-1}) but Ge/Si is still elevated. In April, sampling focused only at three locations in Virginia. The Berry Hill Bridge (DR9_4) and Abrew Grogan Park (DR10_4) have Ge/Si ratios of 1.39 and 1.54 μmol mol^{-1} respectively (Figure 3.5h). Similar to results in February, Anglers Park (DR15_4) had a

significantly higher ratio of 8.09 μmol mol^{-1}. The elevated Ge/Si at DR15_4 matches elevated Sb concentrations of 3.0 μg L^{-1} observed in February (Figure 3.5f).

The Ge/Si pattern in May, July and October are characterized by higher ratios upstream from the Dan River Steam station (DR0-DR1) and a gradual decrease towards DR18 near Kerr Lake (Figure 3.1). May and July have near identical patterns with elevated Ge/Si at DR1 (3.06-3.28 μmol mol^{-1}) (Figure 3.5l). At Draper Landing (DR8), ratios decrease on May and July (2.06-1.51 μmol mol^{-1} respectively) then increase to a range of 2.45-2.44 μmol mol^{-1} at Camilla Williams Park (DR11). Downstream from DR11 (DR15-DR18), ratios continue to drop but are well above the clean river Ge/Si. During May and July, the Anglers Park (DR15) Ge/Si peak observed in February and April was not present (Figure 3.5d and h). This lower ratio contrasts elevated Sb concentrations (36.4 μg L^{-1}) reported during May (Ge/Si = 2.06 μmol mol^{-1}) at Anglers Park (DR15_5). Likewise, Ge/Si of DR16-18 are lower than upstream samples but Sb concentrations range between 0.12-6.03 μg L^{-1} (Figure 3.5j and l).

The Ge/Si trend in October is very similar to that of May and July. However, Ge/Si ratios of the two upstream sites at DR0_10 and DR1_10 are higher than in May and July (4.38 and 4.78 μmol mol^{-1} respectively). Beginning in DR10_10 (2.73 μmol mol^{-1}), Ge/Si decreases to 1.35 μmol mol^{-1} at DR18_10. The decreasing trend in Ge/Si ratios corresponds with the sudden increase in Sb concentrations from DR15_10 to DR18_10 (Figure 3.5n).

3.5 Discussion

Metalloid concentrations during the study were well below the EPA MCL except

for Sb at DR15 and locations downstream. Some of the lowest concentrations observed for these metalloids were in Februray. Antimony was less than 0.10 μg L^{-1} for most samples, except for Anglers Park (DR15_2) with Sb of 3.13 μg L^{-1}. This sample is still below the MCL but it is in sharp contrast to the samples upstream. The low metalloid concentrations for samples collected during the spill is an unexpected result but is consistent with reports (EPA, 2014; NCDEQ, 2014b). Arsenic concentrations near the spill are approximately 0.10 μg L^{-1} then increase to 0.43 μg L^{-1} for samples downstream in the state of Virginia (> 45 km from spill). Given the very dilute As concentrations for these samples, it is difficult to conclude if the increase downstream is due to the spill or simply background concentrations. However, Ge/Si ratios during February are greater than clean rivers suggesting a CCR influence. During the spill, there was limited access to the area near the failed storm water pipe. The only sample collected in Eden, NC downstream from the spill was at the Draper Landing boat ramp (DR8_2). This site had a Ge/Si ratio = 1.96 μmol mol^{-1} and metalloid concentrations less than 0.15 μg L^{-1}. The Ge/Si ratio for DR8 is greater than 0.5 μmol mol^{-1} but has a surprisingly low metalloid concentrations even with its proximity to the retention ponds (Figure 3.1). Incomplete mixing of CCR in the stream and zoning of contaminants along the riverbank was observed during the spill (Jia et al., 2016). CCR travelled along the riverbank on the side of the retention ponds (Figure 3.1). Complete mixing may have occurred until the Schoolfield dam reservoir at about 44 km from the location of the spill (Figure 3.1). Therefore, it is likely that water along the boat ramp of Draper Landing (DR8_2) had not significantly mixed with the CCR from the spill. In Eden, NC the samples with highest Ge/Si ratios were located upstream from the spill (Figure 3.1). Wildlife Access

(DR1_2), Leaksville (DR0_2) and the USGS stream gauge had ratios ranging between 2.16 and 2.53 μmol mol^{-1}. Backflow and dispersion of CCR from the spill would be impeded by a dam upstream from the retention ponds (Figure 3.1). Therefore, elevated ratios may not be caused by the failed storm water pipe. Rather, the elevated Ge/Si could be background metalloid concentrations resulting from CCR inputs or deposition of coal fly ash from coal burning power plants upstream like the Belews Creek facility (Figure 3.1). Additionally, seepage from the retention ponds into the shallow groundwater has been observed in 2014 and 2015 (Harkness et al., 2016; NCDEQ, 2018b). For some monitoring wells in the perimeter of the steam station, arsenic concentrations were above the MCL of 10 μg L^{-1} (NCDEQ, 2018b). The oxidized arsenic species is dominant in coal fly ash due to the oxidizing conditions in the furnace (USGS, 2015). Arsenate adsorption on Fe-oxyhydroxides is highly dependent on pH with maximum adsorption between pH 3.0-8.0 (Plant et al., 2003). Stream pH in February had the narrow range of 7.5 and 7.8 (Table 3.1). Arsenic from retention pond seepage entering the shallow groundwater must rapidly adsorb onto metal oxides for stream water concentrations to remain low. Germanium is less affected by co-precipitation with Fe-oxyhydroxides and should remain in solution (Chimenos et al., 2013; Scribner et al., 2006). Therefore, Ge/Si in stream water can be more readily impacted by contaminated groundwater inputs (Figure 3.5d). The samples collected downstream from the spill in Camilla Williams (DR11_2) and Dan Daniels (DR12-14) parks have ratios that slightly decrease. This decreasing pattern is interrupted by the sharp increase to 8.25 μmol mol^{-1} at Anglers Park (DR15_2) just 3 km downstream from Dan Daniels park locations (DR12-14). Ge/Si at this location is higher than the coal ash slurry but significantly

lower than the ash pond effluents (Table 3.3 & 3.4). At Anglers Park (DR15_2), both Sb and Ge/Si are significantly higher than upstream sites (Figure 3.5b and 3.5d). A very similar pattern is observed in April for the same location. The samples collected near the retention ponds have metalloid concentrations less than or equal to the limit of detection (0.005 μg L^{-1}). However, Anglers Park (DR15_4) displayed elevated Sb concentrations of 3.0 μg L^{-1} and a Ge/Si of 8.09 μmol mol^{-1} (Figure 3.5f and 3.5h). Higher concentrations of antimony at more sites are observed in the sampling campaigns of summer (May-July) and fall (October). For these dates, samples collected further downstream had Sb concentrations that approached the MCL. A distinct feature of the data is the presence of anomalously high antimony concentrations downstream, particularly near the Anglers Park sampling site. While this anomaly was present within a week of the spill, antimony levels notably increased in May and June, long after they had relaxed near the original spill site. Modeling of the transport of CCR in the Dan River predicts downstream deposition, particularly along reaches where either the river gradient drops or along bends that create a velocity gradient (Jia et al., 2016). Cowan et al. (2017) observed this pattern of deposition at sites upstream from the Schoolfield Reservoir where layers of ash deposited in the riverbed (Figure 3.6). CCR transport modelling did not study deposition downstream from the Schoolfield dam and ash deposition was not significant where we observe anomalously high antimony concentrations (Cowan et al., 2017; Jiang et al., 2008). We suggest that Angers Park (DR15), South Boston (DR16), Milton (DR17) and Stauton River State Park (DR18) are close to CCR depositional sites where stream dynamics may remobilize coal fly ash.

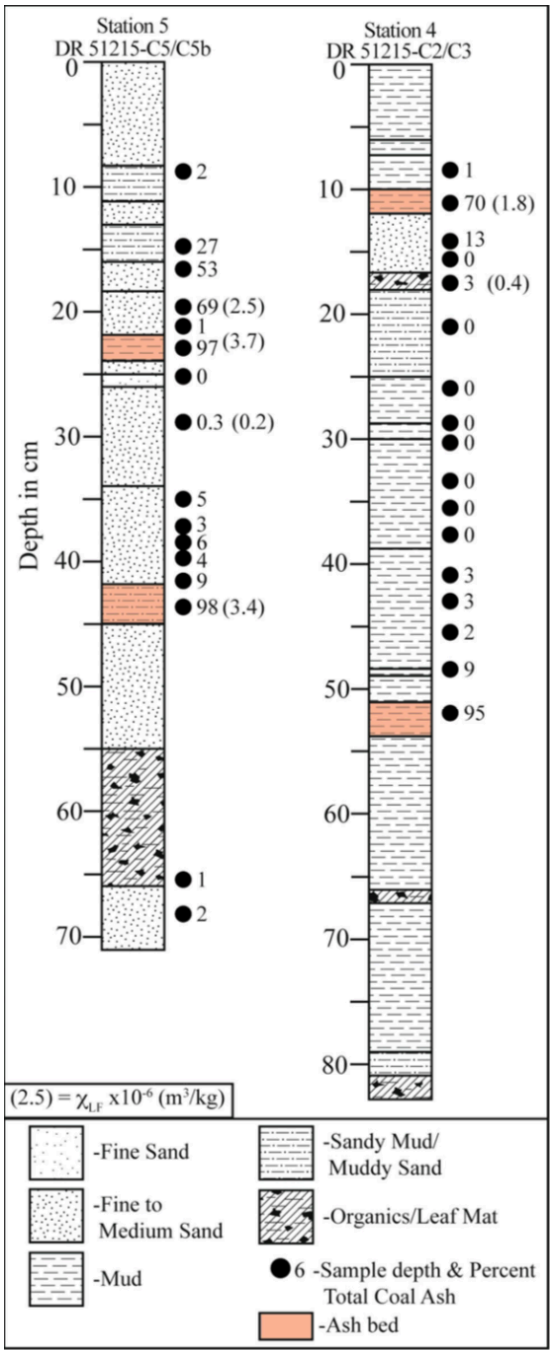

Figure 3.6: Core logs and percent total ash from locations near the Schoolfield reservoir. The black dots are percent total ash determined by point counting. Orange layers represent CCR depositional events. The figure is modified from Cowan et al. (2017).

The generation of larger anomalies in the summer and fall for the particle-reactive metalloids relative to the less reactive germanium are consistent with remobilization

from a sorbed or co-precipitated source such as Fe-oxyhydroxides. The potential of Fe-oxyhydroxide control on these metalloids is consistent with their apparently rapid removal in the vicinity of the spill site. Stream water temperatures during the study increased by 21 °C from March to July (Figure 3.7). Warming water temperatures, which would have been near the annual minimum at the time of the spill, may have promoted bacterial reduction of Fe-oxides on the surface of the ash particles (Figure 3.4). The generation of large anomalies of Sb in May and June, and smaller anomalies in Ge, demonstrate the fractionation of Sb by post-depositional processes. These anomalies persist through the October sampling period, although at lower levels.

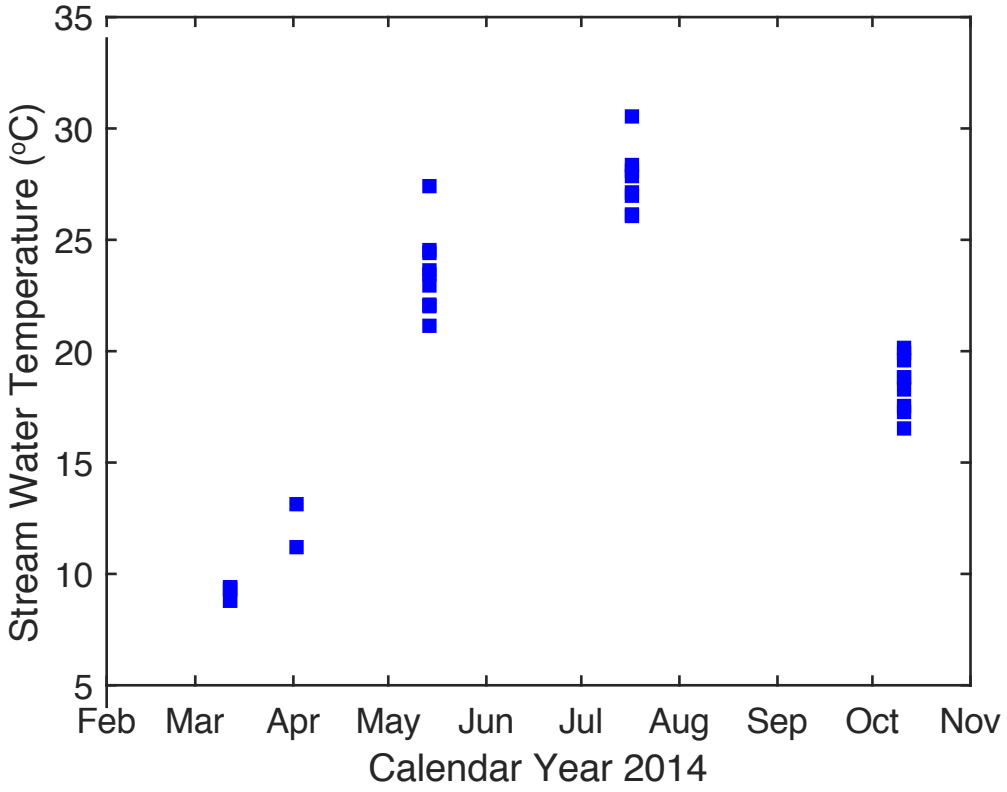

Figure 3.7: Dan River temperatures during sampling period. Stream water temperature for the samples collected from March to October 2014.

The stream pH throughout the study ranges between 6.2 to 7.8. This range is within the adsorption maxima of both reduced and oxidized arsenic species on Fe-oxyhydroxides (Plant et al., 2003). This is not the case for the oxidized antimonate and selenate species which favor adsorption onto protonated surface groups at lower pH (<6). The dominant adsorption mechanism for Sb[V] is inner sphere complexation by means of ligand exchange with a protonated hydroxyl group (Leuz et al., 2006; Essington and Stewart, 2018). As mentioned in the methods section, Sb speciation analysis indicated that Sb[V] was the dominant species throughout the sampling period. Another aspect of the dataset is the increase in specific conductivity for the samples with anomalous Sb (Table 3.1). Concentrations of Cl^- and SO_4^{2-} have strong influence on stream conductivity. These anions also experience a spike at the same location of the Sb anomalies (Table 3.1 and 3.2). Sulfur is a major soluble element in fly ash and SO_4^{2-} can be readily leached from CCR under a wide range of environmental conditions (Izquierdo and Querol, 2012). Additionally, Harkness et al. (2016) found that chloride is positively correlated to As and Se in CCR effluents. Therefore, the increase in Cl^- and SO_4^{2-}, can also be used as proxies for CCR contamination. However, there is still an incomplete understanding of how ionic strength affects Sb[V] adsorption onto metal oxides. Leuz et al. (2006) found that higher ionic strength shifted the adsorption maxima of Sb[V] by goethite to lower pH. Essington and Stewart (2018) did not find an effect from ionic strength on the adsorption of Sb[V] but demonstrated that ligand competition (PO4) can reduce adsorption for both ligands. Therefore, bacterial reduction of Fe-oxyhydroxides may not be the only process that can cause Sb anomalies because redox changes would affect both As and Se desorption as well. Selenium sharply increased

along with Sb in May. However, the magnitude was much lower than Sb possibly due to the lower concentration of Se in the source material (Table 3.3 & 3.4). The data demonstrate that high levels of toxic metalloids, exceeding EPA MCLs, can be introduced into the Dan River months after and tens of kilometers downstream from the spill site. Redox state, pH and ionic strength are some of the many aquatic variables that can affect metalloid mobilization. Variations in some of these parameters may be repeated in subsequent years and possibly other downstream sites with significant deposition of CCR-related materials. We suggest that the best approach to understand the Sb anomalies in our dataset is to sample sediment and pore waters from the riverbed of the Dan River. Consequently, it would seem appropriate to 1) continue monitoring metalloid levels in stream and pore waters in the downstream reaches of the Dan River, and 2) investigate the mechanisms of delayed release of metalloids in considerably more detail.

3.6 Conclusion

The Dan River spill of February 2014 was an opportunity to explore the relationship of Ge/Si ratios of receiving waters with concentrations of toxic metalloids for a major coal ash spill. During the spill, metalloids were significantly below the EPA maximum contaminant limit. Ge/Si ratios were well above the clean river Ge/Si ratio of 0.5 μmol mol^{-1} for all locations showing a clear coal ash fingerprint. In March 2014, two retention pond effluent samples had the highest Ge/Si ratios measured in the study. Additionally, As and Sb were highly enriched. This effluent provided an insight into the chemical composition of the CCR. Interestingly, the effect of this material was very

localized and mixing was poor downstream such that other samples nearby did not reflect the enriched metalloid composition. The samples collected in the summer and fall show a dichotomy between Sb patterns and Ge/Si ratios. Antimony was selectively released and concentrations increased drastically in multiple locations in state of Virginia. Ge/Si ratios mostly showed dilution behavior downstream from the ash pond in the summer and fall. The tracer employed in this study was effective in signaling contamination of CCR into the Dan River during the spill. However, poor lateral mixing in the stream may have minimized the effect of elevated Ge/Si in CCR for samples near the retention pond. The plume of coal ash near the pond was modelled and reported as being localized along the riverbank of the stream for at least 45 km before fully mixing in Danville, VA (Jia et al., 2016). Lastly, given the strong adsorption behavior of the metalloids of interest (As, Sb and Se), the Ge/Si fingerprint of CCR was out of phase temporally with the metalloids in the stream. Metalloids released during the spill or in subsequent discharge from the pond likely co-precipitated with Fe-oxyhydroxides or remained adsorbed to fly ash particles. Changes in environmental conditions or remobilization of ash months after the spill may have led to the release of metalloids to the water column. Our observations indicate this effect can be large and present a clear public health threat, with metalloids well above EPA MCLs. Germanium is largely unaffected by adsorption and the Ge/Si fingerprint experiences dilution as it mixes downstream. As observed by Froelich and Lesley (2001), Ge/Si ratios of receiving waters were much higher than the clean river ratio. Our results also demonstrate the complexity in interpretation of this tracer in a system with chronic CCR contamination. This is showcased by the more elevated Ge/Si ratios upstream from the retention ponds

and the anomalous Sb at locations without Ge/Si spikes. The variation in CCR composition has posed challenges to the detection of contaminants that enter these streams every day. Ge/Si ratios can be a useful tool for detection of CCR contamination due to the narrow range in values in natural systems and the limited sources of Ge into the environment. In this study it is emphasized the importance of continued monitoring of toxic metals in streams impacted by CCR. Ge/Si can serve as a tool for detection and rapid response for environmental management and mitigation.

References

Adriano, D.C., Page, A.L., Elseewi, A.A., Chang, A.C. and Straughan, I. (1980) Utilization and Disposal of Fly-Ash and Other Coal Residues in Terrestrial Ecosystems - a Review. J Environ Qual 9, 333-344.

Anders, A.M., Sletten, R.S., Derry, L.A. and Hallet, B. (2003) Germanium/silicon ratios in the Copper River Basin, Alaska: Weathering and partitioning in periglacial versus glacial environments. Journal of Geophysical Research-Earth Surface 108.

Andreae, M.O., Asmode, J.F., Foster, P. and Vantdack, L. (1981) Determination of Antimony(Iii), Antimony(V), and Methylantimony Species in Natural-Waters by Atomic-Absorption Spectrometry with Hydride Generation. Anal Chem 53, 1766-1771.

Baronas, J.J., Hammond, D.E., Berelson, W.M., McManus, J. and Severmann, S. (2016) Germanium-silicon fractionation in a river-influenced continental margin: The Northern

Gulf of Mexico. Geochimica Et Cosmochimica Acta 178, 124-142.

Bernstein, L.R. (1985) Germanium Geochemistry and Mineralogy. Geochimica Et Cosmochimica Acta 49, 2409-2422.

Calmels, D., Gaillardet, J., Brenot, A. and France-Lanord, C. (2007) Sustained sulfide oxidation by physical erosion processes in the Mackenzie River basin: Climatic perspectives. Geology 35, 1003-1006.

Capobianco, C. and Navrotsky, A. (1982) Calorimetric Evidence for Ideal Mixing of Silicon and Germanium in Glasses and Crystals of Sodium-Feldspar Composition. Am Mineral 67, 718-724.

Chimenos, J.M., Fernandez, A.I., del Valle-Zermeno, R., Font, O., Querol, X. and Coca, P. (2013) Arsenic and antimony removal by oxidative aqueous leaching of IGCC fly ash during germanium extraction. Fuel 112, 450-458.

Cowan, E.A., Epperson, E.E., Seramur, K.C., Brachfeld, S.A. and Hageman, S.J. (2017) Magnetic susceptibility as a proxy for coal ash pollution within riverbed sediments in a watershed with complex geology (southeastern USA). Environmental Earth Sciences 76.

Cowan, E.A., Gaspari, D.P., Brachfeld, S.A. and Seramur, K.C. (2015)

Characterization of coal ash released in the TVA Kingston spill to facilitate detection of ash in river systems using magnetic methods. Fuel 159, 308-314.

Davidson, G.R. and Bassett, R.L. (1993) Application of Boron Isotopes for Identifying Contaminants Such as Fly-Ash Leachate in Groundwater. Environmental Science & Technology 27, 172-176.

Du, G., Zhuang, X.G., Querol, X., Izquierdo, M., Alastuey, A., Moreno, T. and Font, O. (2009) Ge distribution in the Wulantuga high-germanium coal deposit in the Shengli coalfield, Inner Mongolia, northeastern China. International Journal of Coal Geology 78, 16-26.

Elswick, E.R., Hower, J.C., Carmo, A.M., Sun, T. and Mardon, S.M. (2007) Sulfur and carbon isotope geochemistry of coal and derived coal-combustion by-products: An example from an Eastern Kentucky mine and power plant. Applied Geochemistry 22, 2065-2077.

EPA (2014) Duke Energy Coal Ash Spill in Eden, NC, Washington D.C., pp. Surface Water Data - EPA Team 1 - February 2014.

EPA (2017a) Duke Energy Coal Ash Spill in Eden, NC - Sampling Results Ash Pond Data, Washington D.C.

EPA (2017b) History and Response Timeline. United States Environmental

Protection Agency, Washington D.C.

EPA (2018) Steam Electric Power Generating Effluent Guidelines - 2015 Final Rule. United States Environmental Protection Agency, Washington D.C.

Essington, M.E. and Stewart, M.A. (2018) Adsorption of Antimonate, Sulfate, and Phosphate by Goethite: Reversibility and Competitive Effects. Soil Science Society of America Journal 82, 803-814.

Evans, M.J. and Derry, L.A. (2002) Quartz control of high germanium/silicon ratios in geothermal waters. Geology 30, 1019-1022.

Froelich, P.N., Blanc, V., Mortlock, R.A., Chillrud, S.N., Dunstan, W., Udomkit, A. and Peng, T.H. (1992) River fluxes of dissolved silica to the ocean were higher during glacials: Ge/Si in diatoms, rivers, and oceans. Paleoceanography 7, 739-767.

Froelich, P.N., Hambrick, G.A., Andreae, M.O., Mortlock, R.A. and Edmond, J.M. (1985) The Geochemistry of Inorganic Germanium in Natural-Waters. J Geophys Res-Oceans 90, 1133-1141.

Froelich, P.N. and Lesley, P. (2001) Tracing germanium contamination from coal-fired power plants down the Chattahoochee–Apalachicola River: implications for the toxic

metalloids Arsenic and Selenium, Proceedings of the 2001 Georgia Water Resources Conference, University of Georgia, Athens, pp. 488-491.

Harkness, J.S., Sulkin, B. and Vengosh, A. (2016) Evidence for Coal Ash Ponds Leaking in the Southeastern United States. Environmental Science & Technology 50, 6583-6592.

Izquierdo, M. and Querol, X. (2012) Leaching behaviour of elements from coal combustion fly ash: An overview. International Journal of Coal Geology 94, 54-66.

Jia, Y.F., Altinakar, M., Chao, X.B. and Zhang, Y.X. (2016) Numerical Simulations of Spilled Coal Ash in the Dan River and the Environmental Impact of the Incident. World Environmental and Water Resources Congress 2016: Environmental, Sustainability, Groundwater, Hydraulic Fracturing, and Water Distribution Systems Analysis, 114-125.

Jiang, Y.F., Elswick, E.R. and Mastalerz, M. (2008) Progression in sulfur isotopic compositions from coal to fly ash: Examples from single-source combustion in Indiana. International Journal of Coal Geology 73, 273-284.

Kurtz, A.C., Derry, L.A. and Chadwick, O.A. (2002) Germanium-silicon fractionation in the weathering environment. Geochimica Et Cosmochimica Acta 66, 1525-1537.

Lemly, A.D. (2015) Damage cost of the Dan River coal ash spill. Environmental

Pollution 197, 55-61.

Leuz, A.K., Monch, H. and Johnson, C.A. (2006) Sorption of Sb(III) and Sb(V) to goethite: Influence on Sb(III) oxidation and mobilization. Environmental Science & Technology 40, 7277-7282.

Lugolobi, F., Kurtz, A.C. and Derry, L.A. (2010) Germanium-silicon fractionation in a tropical, granitic weathering environment. Geochimica Et Cosmochimica Acta 74, 1294-1308.

Mastalerz, M., Hower, J.C., Drobniak, A., Mardon, S.M. and Lis, G. (2004) From in-situ coal to fly ash: a study of coal mines and power plants from Indiana. International Journal of Coal Geology 59, 171-192.

Meij, R. (1994) Trace-Element Behavior in Coal-Fired Power-Plants. Fuel Process Technol 39, 199-217.

Mortlock, R.A. and Froelich, P.N. (1996) Determination of germanium by isotope dilution hydride generation inductively coupled plasma mass spectrometry. Analytica Chimica Acta 332, 277-284.

NCDEQ (2014a) 2014 Category 5 Water Quality Assessments-303(d) List, Raleigh, NC.

NCDEQ (2014b) Data from ash release at Duke Energy Dan River Station, Raleigh, NC.

NCDEQ (2014c) DWR Data from Ash Release at Duke Energy Dan River Station, Dan River Coal Ash Spill, Raleigh, NC.

NCDEQ (2018a) Environmental Application Tracker, Raleigh, NC.

NCDEQ (2018b) Groundwater Monitoring Data for Duke Energy Coal Ash Facilities, Raleigh, NC, p. Dan River Steam Station.

NOAA (2017) Climate Data Online Station USC00312631, Washington D.C.

O'Haver, T. (2018) A Pragmatic Introduction to Signal Processing.

Plant, J.A., Kinniburgh, D.G., Smedley, P.L., Fordyce, F.M. and Klinck, B.A. (2003) Arsenic and Selenium. Treatise on geochemistry 9, 17-66.

Querol, X., Fernandezturiel, J.L. and Lopezsoler, A. (1995) Trace-Elements in Coal and Their Behavior during Combustion in a Large Power-Station. Fuel 74, 331-343.

Rhodes, T.S. and Conrad, S.G. (1985) Geologic Map of North Carolina. Department of

Natural Resources and Community Development, Division of Land Resources, and the NC Geological Survey.

Rudnick, R. and Gao, S. (2003) Composition of the continental crust. Treatise on geochemistry 3, 659.

Ruhl, L., Vengosh, A., Dwyer, G.S., Hsu-Kim, H., Schwartz, G., Romanski, A. and Smith, S.D. (2012) The Impact of Coal Combustion Residue Effluent on Water Resources: A North Carolina Example. Environmental Science & Technology 46, 12226-12233.

Ruhl, L.S., Dwyer, G.S., Hsu-Kim, H., Hower, J.C. and Vengosh, A. (2014) Boron and Strontium Isotopic Characterization of Coal Combustion Residuals: Validation of New Environmental Tracers. Environmental Science & Technology 48, 14790-14798.

Scribner, A.M., Kurtz, A.C. and Chadwick, O.A. (2006) Germanium sequestration by soil: Targeting the roles of secondary clays and Fe-oxyhydroxides. Earth and Planetary Science Letters 243, 760-770.

USGS (2015) Trace Elements in Coal Ash, in: Interior, U.S.D.o.t. (Ed.), Washington D.C.

Vassilev, S.V. and Vassileva, C.G. (1997) Geochemistry of coals, coal ashes and

combustion wastes from coal-fired power stations. Fuel Process Technol 51, 19-45.

VDEQ (2014) 2014 Impaired Waters - 303(d) List, Richmond, VA.

Weaver, J.C. (1996a) Low flow characteristics and profiles for selected streams in the Roanoke River Basin, North Carolina, in: Survey, U.S.G. (Ed.), Raleigh, North Carolina.

Weaver, J.C. (1996b) Low-flow characteristics and profiles for selected streams in the Roanoke River Basin, North Carolina. 56.

Williams, L.B. and Hervig, R.L. (2004) Boron isotope composition of coals: a potential tracer of organic contaminated fluids. Applied Geochemistry 19, 1625-1636.

CHAPTER FOUR:

GERMANIUM-SILICON AS A TRACER FOR HYDROLOGIC PATHWAYS IN A PAIRED CATCHMENT OF THE LUQUILLO CRITICAL ZONE OBSERVATORY

Abstract

Catchment lithology is a significant factor influencing the generation and transport of solutes in the critical zone. In the Luquillo Mountains of Puerto Rico, the Quebrada Guaba and Bisley catchments are compared to understand how lithology affects concentration-discharge (C-Q) relationships. Ge/Si ratios in porewater and stream samples are used to identify sources of Si to streams in the Bisley 1 watershed. Quebrada Guaba is underlain by quartz diorite and is characterized by strong Si dilution behavior (power law slope = -0.47). During baseflow, Ge/Si = 0.27-0.47 μmol mol^{-1} due to weathering of plagioclase and precipitation of Ge enriched kaolinite in the bedrock-saprolite interface. During storms, hydrologic pathways shift to shallower flow paths with lower Si concentrations and higher Ge/Si (1.0-4.0 μmol mol^{-1}). The shift to saprolite-dominated flow paths carrying dilute Si end-members drives the Si-Q pattern in this catchment. The volcaniclastic sub-catchment of Bisley 1 has a more chemostatic Si-Q relationship (power law slope of = -0.30). We would like to understand how solute generation and water transport differs in Bisley that leads to less Si dilution. In this study, we analyzed stream water samples collected during a storm event that resulted in a two pulsed hydrograph on June 6th, 2011. For the first pulse, the Si-Q pattern displays a clockwise hysteresis loop suggesting the activation of a subsurface pathway with lower Si concentrations than groundwater fed baseflow. By the onset of the second pulse, the direction of the hysteresis loop switched to counter-clockwise indicating

solute contributions from a source not previously observed on the first hydrograph. This suggests that the new source must have a longer fluid residence time allowing equilibrium to be reached with the clay rich mineral matrix. We used Ge/Si as a tracer for Si sources to the stream during this storm event. Additionally, porewater samples collected from shallow (0.15 m) and deep (9.3 m) lysimeters were analyzed in order to characterize subsurface end-members. This analysis will help us understand the geochemical processes responsible for the distinct signatures of the various end-members. Additionally, the Ge/Si to discharge relationship during this event will demonstrate the hydrologic processes responsible for the hysteresis patterns.

4.1 Introduction

Solute transport along hydrologic pathways in the critical zone (CZ) can define the shape of concentration-discharge (C-Q) patterns. These C-Q relationships are an integration of multiple geochemical reactions and hydrologic processes that provide insights into the structure of the CZ. Ge/Si ratios have been widely used to understand the weathering regimes of river systems across the world (Froelich et al., 1992; Murnane and Stallard, 1990; Torres et al., 2017). Landscapes of the weathering limited regime have high dissolved silica loads with Ge/Si ratios below the average continental silicate value of 0.5 μmol mol^{-1} (Froelich et al., 1992; Murnane and Stallard, 1990). In these landscapes, runoff and erosion exceed the rate of weathering reactions. Weathering is incongruent leading to the fractionation of Ge/Si ratios resulting in the precipitation of Ge enriched secondary minerals and a Ge depleted solute (Froelich et al., 1992; Kurtz et al., 2002; Murnane and Stallard, 1990). In the transport limited regimes, rates of

chemical weathering exceed the physical removal processes that export solutes from the landscape. These landscapes are characterized by thick weathered regolith with low dissolved silica loads. Streams have higher Ge/Si ratios that exceed bedrock proportions because of the dissolution of Ge enriched secondary minerals (Froelich et al., 1992). In large river systems, Ge/Si ratios have been applied to understand the mixing between sub-catchments of different weathering regimes (Torres et al., 2017). However, applying this tracer at a large scale limits your ability to interpret hydrologic pathways in a catchment. Therefore, using Ge/Si ratios as a hydrologic tracer in small headwater catchments has been more useful in elucidating how a combination of hydrologic pathways give streams their characteristic chemistry (Kurtz et al., 2011). In this study, we use stream water Si and Ge/Si data from an event sampling campaign on June 6th, 2011 in the Bisley 1 sub-catchment of the Luquillo Critical Zone Observatory of Puerto Rico. Our objectives are 1) to use Ge/Si ratios to understand the sources of Si at different points of the hydrograph, 2) to combine understanding of geochemical signals to make inferences on hydrologic pathways and 3) compare results in the volcaniclastic Bisley catchment to the neighboring granitic Quebrada Guaba catchment.

4.2 Site Description

Bisley 1 is a 0.1 km^2 headwater catchment that is part of a sequence of watersheds (numbered 1-5) that drain into Rio Mameyes in northeastern Puerto Rico (Figure 4.1). The U.S. Geological Survey Water Energy and Biogeochemical Budgets (WEBB) and the NSF Long Term Ecological Research (LTER) program have been collecting environmental data here for over twenty years. Currently, Bisley 1 is one of

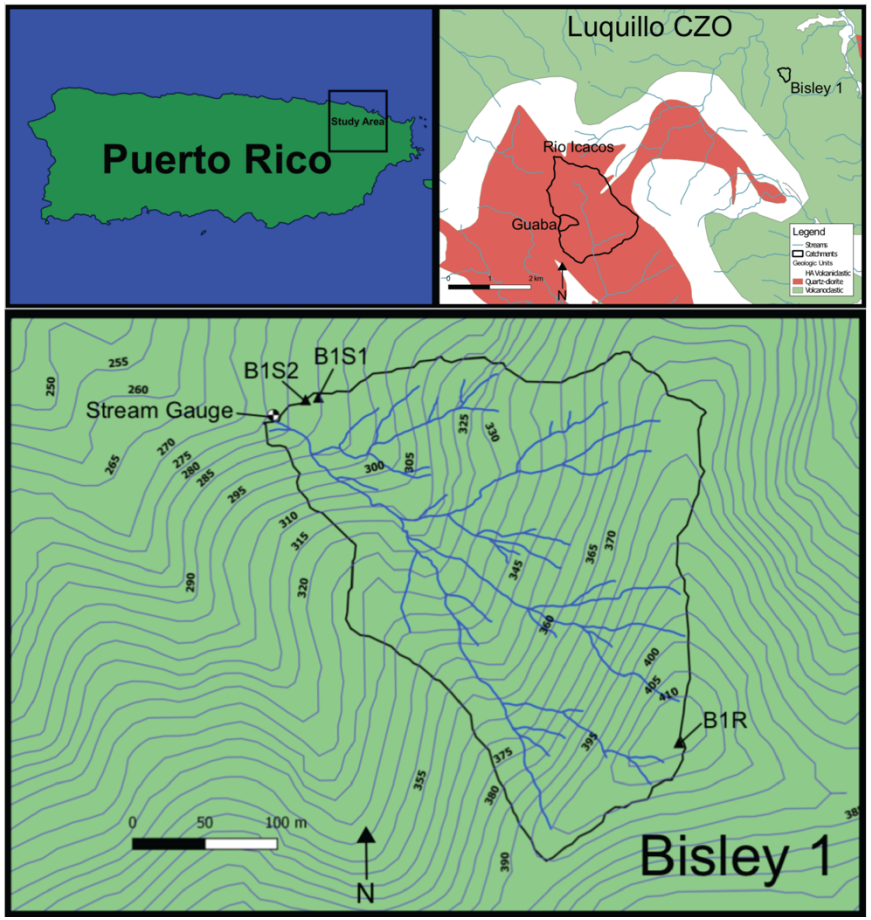

Figure 4.1: Luquillo CZO sub-catchments and Bisley 1 sampling locations. (left) Northeastern Puerto Rico. (center) The Luquillo CZO sub-catchments of Quebrada Guaba and Bisley 1 with geologic units. (right) Bisley 1 sub-catchments with lysimeter locations, stream gauge and elevation contours.

the research sites of the Luquillo Critical Zone Observatory (LCZO). At Bisley 1, elevation ranges between 260 to 400 m with a slope of 21.9° (Buss et al., 2017; Wymore et al., 2017). Annual precipitation in the Bisley ranges between 3000-4000 mm yr^{-1} while temperatures range between 24° in December-February to 27 °C in July-August (Scatena, 1989; Schellekens et al., 2004). The Bisley watersheds are underlain by the Fajardo formation. This geologic unit is a basaltic to andesitic, marine bedded meta-volcaniclastic formation (Jolly et al., 1998).

Table 4.1: Bedrock chemistry of the Bisley catchments

SiO2	Al2O3	MgO	CaO	Na2O	K2O
		wt. %			
53.1	16.8	5.5	7.9	2.8	0.8

Buss et al. (2017)

Table 4.2: Bedrock mineralogy of the Bisley catchments

Quartz	K-spar	Plagioclase	Kaolinite	Chlorite	Pyroxene	Amphibole
			wt. %			
10	5.8	36	0.4	24	9.4	36

Buss et al. (2017)

Soils are clayey and significantly leached Ultisols with a thickness between 0.8-1.0 m (Scatena, 1989). Hydraulic conductivity (K_{sat}) is highest within the top 0.2 meters with values of around 6.3 m day^{-1} (Schellekens et al., 2004). Vegetation at Bisley 1 is composed of a mature Tabonuco forest (*Dacryodes excelsa*) consisting of 45.7% of the above ground biomass (Scatena et al., 1993). Sierra palm trees (*Prestoea acuminata*) and ferns are also common species.

4.3 Methods

In June 6th, 2011 during a 55 mm precipitation event, Dr. Andrew Kurtz and Dr. Steve Goldsmith collected stream water samples over a 2.5-hour period (Figure 4.2). Precipitation fell in two events resulting in a two pulsed hydrograph. Stream discharge is not available for this dataset due to problems with the rating curve for this stream gauge. Instead, stage height will be used as a proxy for stream flow. Using stage height, we can still observe variations in stream chemistry in response to changes in hydrologic conditions.

Samples were filtered using 0.45 μm cellulose nitrate filters (GE Whatman™), collected in HNO_3 washed low density poly-ethylene bottles (LDPE) and acidified to a pH of less than 2 using trace metal grade 70% HNO_3. The stream samples were analyzed for major cations using the Jobin Yvon Ultrace JY-138 ICP-ES. Additionally, germanium was analyzed using hydride generation ICP-MS using a VG Plasmaquad 2+ ICP-MS at Boston University (Lugolobi et al., 2010).

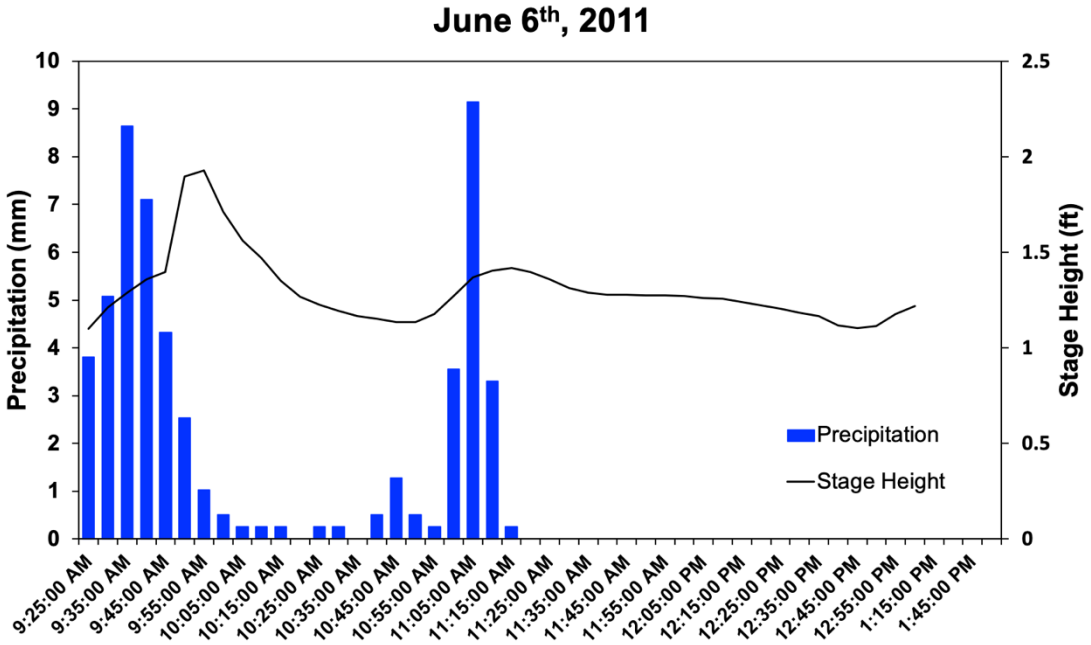

Figure 4.2: Bisley 1 precipitation and stage height. Precipitation (mm) and stage height (ft) in the Bisley 1 catchment.

The tension lysimeters were pressurized on February 27th, 2017 then sampled the following day using the same filtering and preservation techniques for stream water. A baseflow sample was collected during this sampling campaign and preserved using the fore mentioned techniques. We will make the assumption in our analysis that groundwater chemistry is represented by this baseflow sample. Major cations for soil pore water and baseflow were analyzed using ICP-OES at Cornell University (AMETEK SpectroBlue). Germanium was analyzed using isotope dilution hydride generation ICP-MS (Mortlock and Froelich, 1996). An enriched ^{70}Ge tracer solution (spike) was added to the water samples and equilibrated for at least 24 hours at 60 ^{o}C. The target $^{70}Ge/^{74}Ge$ in the sample was 10, corresponding to the geometric mean between the natural (0.56) and the spike (162) $^{70}Ge/^{74}Ge$ ratios. The target ratio

corresponds to the lowest analytical uncertainty for IDA (Heumann, 1988; Mortlock and Froelich, 1996). The samples were introduced into the hydride system along with a 4% $NaBH_4$ solution that promoted the reduction of germanic acid ($GeOH_4$) to a volatile hydride (GeH_4) that was then transported by argon gas into the ICP-MS (Thermo-Finnigan Element 2). Germanium was quantified by standard curve method and isotope dilution using the $^{70}Ge/^{74}Ge$ ratio. Corrections for mass bias and signal drift were done using sample-standard bracketing. At the same time, response curves were established by analysis of Ge standards at 5, 20, 50, 100, 200 and 500 ng L^{-1}. Additionally, the results from isotope dilution calculations were cross-checked against the standard response curves measured at m/z =74. With ($^{70}Ge/^{74}Ge$) spike = 162, the spike contribution to m/z 74 is negligible.

4.4 Results

4.4.1 Silicon and Ge/Si to stage height patterns during the storm

Silicon concentrations before the first hydrograph pulse were 217 μM then decreased to 72 μM during peak stage height (Table 4.3 and Figure 4.3). This is the lowest concentrations measured during the storm event of June 6th, 2011. As the hydrograph relaxes, concentrations gradually increase to 207 μM as baseflow conditions are restored. There is a second dilution event at the onset of another

Table 4.3: Bisley 1 stream chemistry for June 6th, 2011.

Time	Stage Height	Si	Ca	Mg	Na	K	Ge	Ge/Si
hr:mm:ss	(ft)	(µM)	(µM)	(µM)	(µM)	(µM)	(pM)	(µmol mol^{-1})
Hydrograph 1								
Rising Limb								
9:45:00 AM	1.40	217	45.2	45.6	107	16.1	194	0.90
9:50:00 AM	1.90	85.3	21.7	22.8	67.5	18.0	165	1.93
10:00:00 AM	1.93	72.0	18.7	19.3	55.1	14.8	121	1.68
Falling Limb								
10:10:00 AM	1.71	133	32.0	29.8	66.8	14.4	647	4.85
10:15:00 AM	1.56	127	34.5	33.5	83.8	16.7	192	1.51
10:20:00 AM	1.47	143	37.2	33.3	83.3	15.4	399	2.80
10:25:00 AM	1.35	146	39.2	36.1	91.0	15.6	269	1.85
10:30:00 AM	1.27	169	42.4	38.6	102	17.0	372	2.20
10:35:00 AM	1.23	175	43.6	39.9	102	17.3	364	2.08
10:40:00 AM	1.20	182	44.6	40.4	115	18.0	373	2.05
10:45:00 AM	1.17	207	48.7	43.8	110	18.1	495	2.39
10:50:00 AM	1.15	199	47.6	42.3	112	17.6	445	2.23
10:55:00 AM	1.13	182	45.2	41.7	105	16.8	214	1.18
11:00:00 AM	1.13	159	41.1	38.0	102	17.5	174	1.10
Hydrograph 2								
Rising Limb								
11:05:00 AM	1.18	134	32.7	31.7	87.5	17.2	216	1.61
11:10:00 AM	1.27	93.1	24.2	25.3	76.6	17.1	147	1.58
11:15:00 AM	1.37	100	30.9	27.5	80.0	16.3	180	1.81
11:20:00 AM	1.40	105	29.1	28.7	77.9	16.4	173	1.65
11:25:00 AM	1.42	134	30.1	30.1	87.6	16.1	436	3.26
Falling Limb								
11:30:00 AM	1.40	129	32.5	31.3	80.4	14.3	315	2.44
11:35:00 AM	1.36	151	34.4	33.4	79.9	15.6	594	3.94
11:40:00 AM	1.31	136	37.1	35.3	94.7	16.6	201	1.48
11:45:00 AM	1.29	161	33.9	33.8	86.1	16.7	608	3.77
11:50:00 AM	1.28	135	32.2	32.5	87.1	15.8	294	2.18
11:55:00 AM	1.28	162	33.8	32.7	100	17.4	589	3.64
12:00:00 PM	1.28	144	33.0	33.4	86.9	15.8	399	2.77
12:05:00 PM	1.28	128	31.8	31.2	82.1	15.4	235	1.83

continued on next page

Table 4.3 (*continued*)

Time	Stage Height	Si	Ca	Mg	Na	K	Ge	Ge/Si
hr:mm:ss	(ft)	(μM)	(μM)	(μM)	(μM)	(μM)	(pM)	(μmol mol^{-1})
12:10:00 PM	1.27	173	36.0	35.6	89.1	17.1	653	3.78
12:15:00 PM	1.26	179	37.5	37.0	93.8	16.3	633	3.54
12:20:00 PM	1.26	163	39.1	38.1	96.2	16.6	321	1.97
12:25:00 PM	1.24	185	42.3	40.1	101	17.0	508	2.74
12:30:00 PM	1.22	202	45.1	43.0	108	17.4	548	2.71
12:35:00 PM	1.21	189	44.7	42.6	103	15.3	290	1.53
12:40:00 PM	1.18	208	48.2	45.1	107	16.3	473	2.27
12:45:00 PM	1.17	180	42.0	39.8	98.6	14.8	321	1.78
1:00:00 PM	1.12	221	47.3	44.7	107	16.8	624	2.83
1:15:00 PM	1.10	235	47.7	45.2	110	16.0	689	2.93
1:30:00 PM	1.11	204	42.3	41.1	102	16.9	565	2.77
1:45:00 PM	1.18	153	37.1	36.0	97.6	15.6	185	1.21
2:00:00 PM	1.22	236	50.3	47.1	116	16.4	640	2.71

hydrograph pulse beginning at 11:10 AM when Si concentrations decrease to 93 μM. Interestingly, concentrations begin to recover to baseflow levels (~200 μM) before peak stage height. During peak stage height, Si concentrations were around 130 μM and continue to increase to 235 μM during hydrograph recession.

The silicon to stage height pattern observed in Bisley 1 has a clockwise turning hysteresis loop. During the rising limb of hydrograph 1 (H1), Si concentrations experience dilution as baseflow levels at 217 μM decrease to 72 μM. During the falling limb, concentrations gradually recover to near baseflow levels of around 200 μM. The loop is open-ended even though Si concentrations in baseflow are nearly identical to concentrations after hydrograph recession. The difference is in stage height levels between both collection times. At time 9:45 AM, the stage height was already on the rise (rising limb). Therefore, if a sample was collected at around 1.2 ft, the hysteresis loop may have closed.

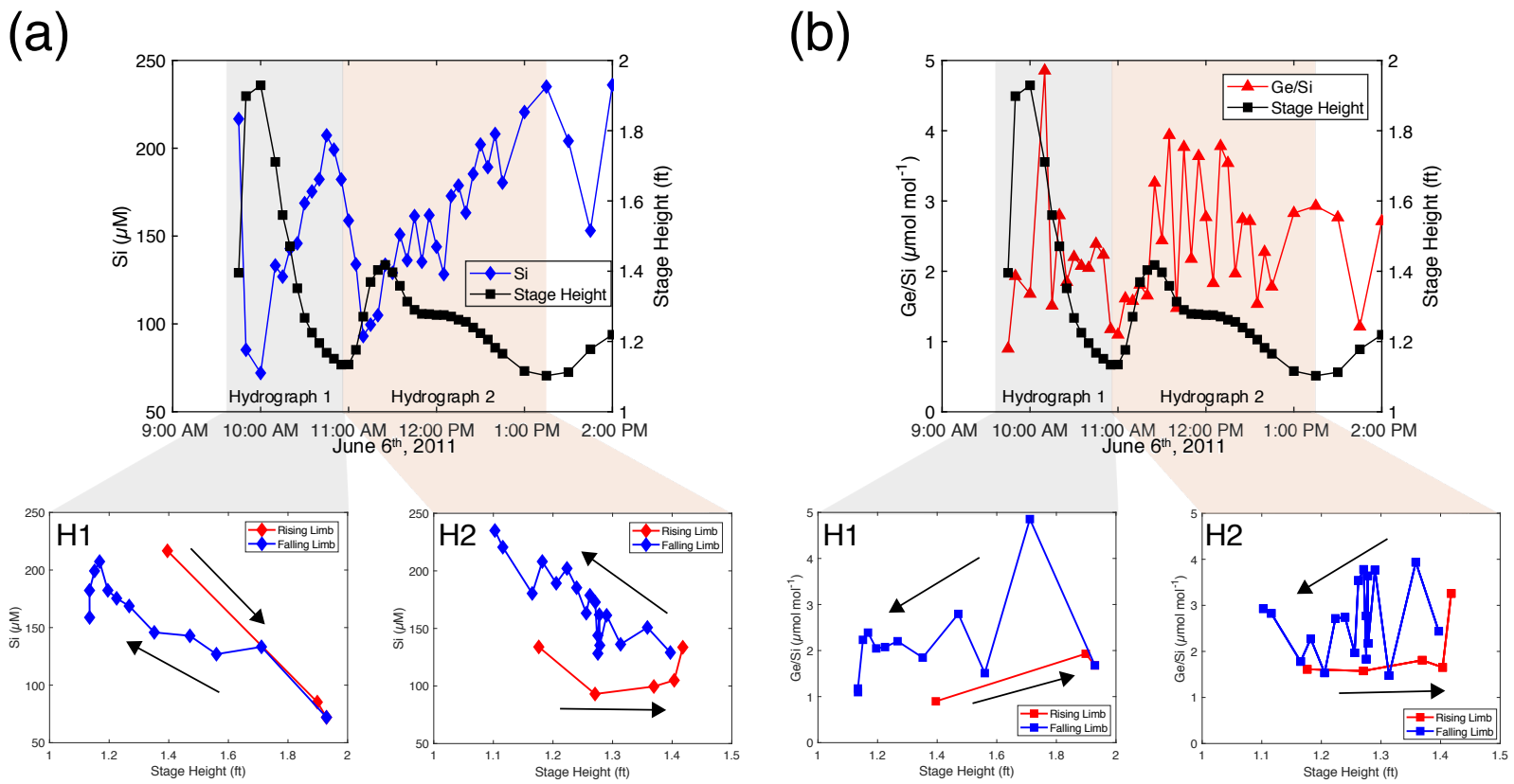

Figure 4.3: Silicon and Ge/Si to stage height relationships. (a) Bisley 1 silicon concentrations (µM) to stage height (ft) during a two pulsed hydrograph event on June 6th, 2011. Hydrograph 1 (H1) shows a clockwise hysteresis loop while hydrograph 2 (H2) switches looping direction to counter-clockwise. (b) Ge/Si ratio (µmol mol^{-1}) to stage height (ft) for the same storm event. Both hydrographs for Ge/Si-stage height have counter-clockwise turning patterns.

Open-ended loops indicate changes in chemistry of the groundwater with infiltration of dilute event water (Evans and Davies, 1998).The infiltration of event water leads to dilution in the groundwater causing lower baseflow concentrations when baseflow is restored.

The Si to stage height pattern of the second hydrograph pulse (H2) turns in the counter-clockwise direction. Initial Si concentrations were 134 μM then decrease to 93 μM as the stage height increases. Subsequently, concentrations plateau around 100 μM before increasing to 150 μM. In the falling limb, Si concentrations gradually increase to 230 μM. The switching of direction of the hysteresis loop represents a change in the component ranking of end-members to the system (Evans and Davies, 1998).

For Ge/Si ratios, both hydrographs display counter-clockwise turning hysteresis loops (Table 4.3 and Figure 4.3). In H1, the Ge/Si ratio increases from 0.90 to 1.68 μmol mol^{-1} as stage height increases. In contrast to the Si pattern, Ge/Si ratios increase with discharge as saprolite hydrologic pathways are activated in the subsurface (Kurtz et al., 2011). This transport mechanism mobilizes soil water that has interacted with secondary minerals with higher Ge/Si. The falling limb of H1 has Ge/Si ratios at 4.85 μmol mol^{-1} then decreases to 1.51 μmol mol^{-1} only 15 minutes later. Subsequently, the ratio ranges between 2.8 and 1.18 μmol mol^{-1} as H1 relaxes to baseflow levels. The spikes in Ge/Si ratios in the falling limb may be caused by macropore flow that quickly transports high Ge/Si carrying soil water to the stream (Kurtz et al., 2011; Schellekens et al., 2004). For H2, the rising limb has nearly uniform Ge/Si ratios around 1.6 μmol mol^{-1} then increases to 4.0 μmol mol^{-1} as the hydrograph recedes. Once again, we observe the dramatic shifts

in Ge/Si ratios during the falling limb of the stage hydrograph. In H2, macropore flow may be more dominant than in H1 resulting in more spikes in the Ge/Si ratios during recession. More importantly, ratios are higher in H2 than in H1. Most samples in the falling limb of H1 have Ge/Si that ranges between 2.0 and 2.5 μmol mol^{-1} while H2 has a wider range between 2.5 and 4.0 μmol mol^{-1}.

4.4.2 Bisley 1 soil pore water chemistry

Silicon concentrations in soil water ranged between 82 and 236 μM over a 9.0-meter depth. The B1S1 nodes have the greatest variation among sites sampled, with concentrations as low as 82 μM (Table 4.4 and Figure 4.4). Silicon concentrations at 9.3 meters are 170 μM then decrease to 90 μM at 4.3-meter depth. Concentrations remain around 80-90 μM before increasing to 236 μM at 0.3 meters from the surface. This Si "elbow" has been observed in soils from the neighboring Quebrada Guaba

Table 4.4: Bisley 1 lysimeter chemistry

ID	Depth (m)	Si (µM)	Ca (µM)	Mg (µM)	Na (µM)	Al (µM)	Ge (pM)	Ge/Si (µmol mol^{-1})
B1S1								
B1_0.5	0.2	87		7	109.8		135	1.55
B1_1	0.3	236	4	9	126.4	6	204	0.86
B1_2	0.6		28		221.1			
B1_3	0.9	163		19	134.4	12	226	1.38
B1_4	1.2	166		20	134.7	21	305	1.84
B1_5	1.5	82	6	15	114.0	8	142	1.73
B1_6	1.8	105	4	17	101.7	15	301	2.87
B1_14	4.3	90	29	40	112.6	6	155	1.72
B1_30.5	9.3	170	42	46	150.5		172	1.02
B1S2								
B2_0.5	0.2	204	9	21	208		195	0.95
B2_4	1.2	151	5	16	240	6	243	1.61

continued on next page

Table 4.4 (*continued*)

ID	Depth (m)	Si (µM)	Ca (µM)	Mg (µM)	Na (µM)	Al (µM)	Ge (pM)	Ge/Si (µmol mol^{-1})
B2_6	1.8	134		13	197		274	2.04
B2_9	2.7	141	6	12	209		208	1.48
B1R								
BR_4	1.2	183	16	28	257	11	182	1.00
BR_5	1.5	118	22	22	171	9	103	0.87
BR_6	1.8	150	9	20	243	10	171	1.14
BR_8	2.4	212	9	31	209	12	279	1.32
BR_11	3.4	149	11	19	195	4	139	0.93

catchment (Lugolobi et al., 2010). The increase in Si concentrations at 0.3 meters may be caused by quartz weathering or dissolution of biogenic opal that has accumulated from litterfall (Bartoli, 1983; White et al., 1998; Ziegler et al., 2005). The Ge/Si ratios at this depth are lower at 0.86 μmol mol^{-1} as would be expected from weathering from a depleted Ge mineral phase. Phytoliths secreted on plant leaves have low Ge/Si due to

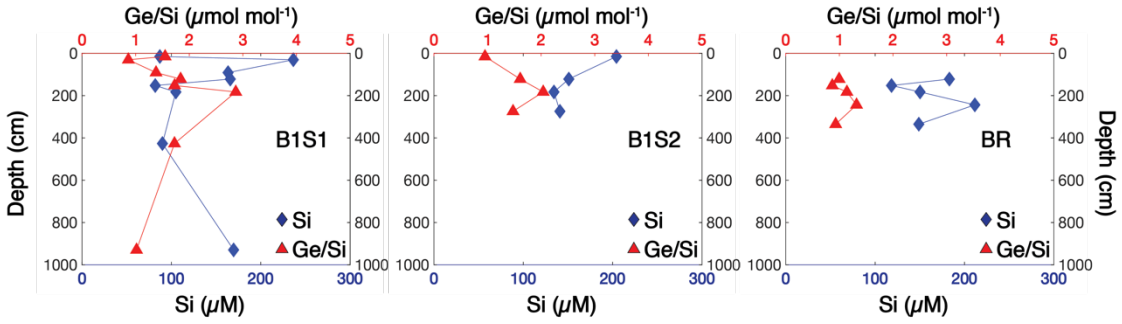

Figure 4.4: Soil pore water Si and Ge/Si ratios for Bisley 1. Soil pore water Si (µM) concentrations and Ge/Si (µmol mol^{-1}) ratios for the B1S1, B1S2 and BR lysimeters.

discriminant transport of Ge across the Casparian strip in roots (Ma et al., 2006; Sparks et al., 2011). Over 99% of vegetative cover in the greater Mameyes watershed is tropical forests and shrub with leaf phytolith Ge/Si ratios ranging between 0.03-0.12 μmol mol^{-}

[1] (Lugolobi et al., 2010; Murphy and Stallard, 2012). The Ge/Si ratios for quartz measured in Hawai'ian basalts is also low at 0.5 μmol mol^{-1} (Kurtz et al., 2002). Using a Ge/Si mass balance approach, Lugolobi et al. (2010) determined that phytolith dissolution was contributing to low Ge/Si ratios in the shallow soil but quartz dissolution was likely dominating this process. Quartz abundance is highest (21 to 30 wt. %) within 0.6-1.5 meter depth in the B1S1 regolith (Buss et al., 2017). Therefore, at 0.3 m depth we may be seeing weathering of these two low Ge/Si mineral phases. Soil pore water Ge/Si peaks at 1.8 m depth with a value of 2.87 μmol mol^{-1}. The higher Ge/Si ratio indicates weathering of kaolinite. In fact, kaolinite mineral abundance peaks at 67 wt. % at the same depth (Buss et al., 2017). Below 1.8 meters, kaolinite is still the dominant mineral phase until 9.0 m where there is some 2.4-4.2 wt. % k-spar remaining (Buss et al., 2017). Ge/Si at B1S1 reflects this changing mineralogy with depth as ratios decrease from 2.87 μmol mol^{-1} at 1.8 m to 1.02 μmol mol^{-1} at 9.3 m.

In the adjacent B1S2 lysemeters located downslope, soil water was only collected down to 2.7 m depth. At this site, we observe very similar Si and Ge/Si patterns as B1S1. From 2.7 to 1.2 m, silicon concentrations were 141 and 134 μM respectively. At 0.2 m depth, Si concentrations increase to 204 μM. Ge/Si ratios were also lowest at 0.95 μmol mol^{-1} suggesting quartz and phytolith dissolution. The highest ratio was also observed at 1.8 m with 2.04 μmol mol^{-1}. This reflects very similar mineralogy as that described in B1S1. In the upper ridge lysimeters of B1R, silicon concentrations are highest at 2.4 m with 212 μM. Surprisingly, silicon follows a similar trend as Ge/Si. In B1S1 and B1S2, Si and Ge/Si are inversely proportional reflecting Ge/Si fractionation as primary minerals weather to secondary clays. At B1R, Si are not inversely

proportional to Ge/Si and concentrations range between 118 and 212 μM, while Ge/Si ratios were 0.87 and 1.32 μmol mol^{-1}.

The regolith at Bisley is highly weathered and depth to fresh bedrock can be greater than 15 m deep (Buss et al., 2017). Elements like Ca, Mg and Na are almost completely depleted in regolith core samples extracted near the lysimeter sites (Buss et al., 2017). Calcium and Na have been depleted from soils by weathering of plagioclase while Mg is sourced from alteration of chlorite (Lara et al., 2017). Our soil pore water results are not corrected for precipitation and evapotranspiration because we did not have Cl^- data. Therefore, we have elevated concentrations of Na, Ca and Mg that we cannot attribute to mineral weathering (Table 4.4). Sodium and Mg are derived from marine aerosols and deposited on the catchment surface by easterly trade winds (Mcdowell et al., 1990; Murphy and Stallard, 2012). Calcium is less concentrated than Na and Mg but also sourced from deposition on the catchment surface. The source of Ca to the Bisley soil has been previously identified as Saharan dust containing about 5 wt. % calcite (Pett-Ridge et al., 2009; Prospero et al., 1981; Stallard, 2001). Silicon inputs from precipitation are two orders of magnitude lower than pore water (Buss et al., 2017). Therefore, we did not feel necessary to correct for Si inputs form precipitation in our pore water and stream data.

4.5 Discussion

The convex hysteresis loops formed during the two hydrograph pulses can be generated from two to three component mixing as described by Evans and Davies (1998). The convex, clockwise turning loop of H1 implies a three end-member

component ranking of $C_{GW} > C_{SE} > C_{SO}$. Where the subscripts of GW, SE and SO represent groundwater, surface event and soil water respectively. For the counter-clockwise hysteresis loop, the component ranking is $C_{GW} > C_{SO} > C_{SE}$. However, a two-component mixing can also generate the hysteresis loop of H1 with the following ranking; $C_{pre\text{-}event} > C_{event}$. This condition can be met only if pre-event water lags event water. However, in 1/Si to Ge/Si mixing space, stream samples do not form a straight-line indicative of two component mixing (Figure 4.5). Instead, a triangle is formed representing three end-member mixing. This mixing behavior was observed in the granitic Quebrada Guaba catchment of the LCZO (Kurtz et al., 2011). In Guaba, the three-component mixing was between groundwater, soil paste extractions and tension lysimeter. Groundwater represented the high Si and low Ge/Si end-member. The composition of this end-member is derived from water flowing along the bedrock-saprolite interface zone where incongruent weathering of primary minerals generates dissolved Si (Kurtz et al., 2011; Lugolobi et al., 2010). In Guaba, stream samples form a mixing line between groundwater and soil paste extractions. Soil paste extractions were characterized as event water travelling along the high K_{sat} shallow soil with limited interaction with the soil minerals. This end-member called quick water, had lower Si than groundwater but higher Ge/Si ratios due to interactions with secondary minerals in the soil. Tension lysimeter samples were the third end-member having higher Si and Ge/Si ratios than quick water. However, lysimeters were a minor contributor to stormflow making up only about 10 to 20% of volumetric flow. Therefore, stream water at Guaba was dominated by mixing between groundwater and quickwater. This finding explains the strong dilution behavior for weathering solutes in this catchment (Shanley

et al., 2011; Wymore et al., 2017). The mixing of these three components resulted in clockwise hysteresis for Si and counter clockwise loops for Ge/Si.

In the Bisley 1 catchment, we can observe two mixing relationships between samples from rising and falling hydrograph limbs (Figure 4.5). For the first mixing relationship, groundwater (GW) forms a straight line with the B1S1, B1S2 and BR lysimeters (SE). In the second, groundwater is mixing with an un-identified third component with higher Ge/Si ratios (SO). Stream samples from the rising limbs fall along the first mixing line (GW-SE), while samples in the falling limb are closer to the second (GW-SO). Recall in the rising limb of the stage hydrograph, there is dilution of Si concentrations (Figure 4.3). This indicates contribution from event water with low Si. However, Ge/Si ratios increase during the rising limb suggesting the activations of a saprolite hydrologic pathway. This mechanism closely resembles quick water as described in the Quebrada Guaba catchment (Kurtz et al., 2011). Interestingly, our lysimeter samples (0.3-9.3 m deep) resemble this quick water component. The stream samples in the falling limb of H1 are close to the first mixing line but begin to deviate towards the second mixing relationship (Figure 4.5). This shifting suggests the contribution from the third end-member (SO). This third component is likely a deeper soil water reservoir that has had a longer interaction time with the mineral matrix because of higher Si and Ge/Si ratios. This interpretation would be consistent with a component ranking of $C_{GW} > C_{SE} > C_{SO}$ that produces a clockwise turning hysteresis loop like H1.

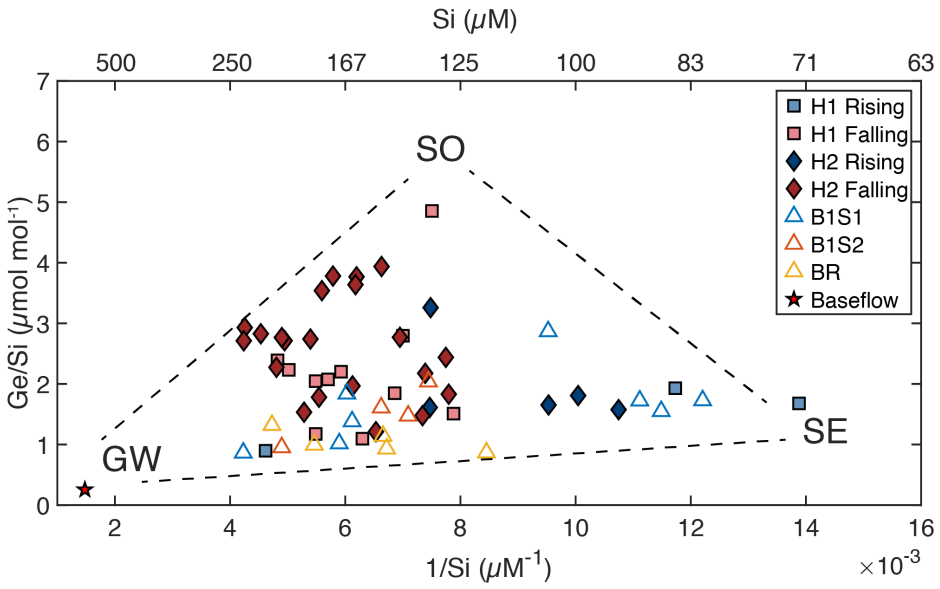

Figure 4.5: Bisley 1 1/Si and Ge/Si mixing space. Bisley 1 stream samples from rising limb (blue) and falling limb (red). Lysimeter samples for B1S1, B1S2 and BR are shown in triangles. The dashed lines are qualitative mixing relationships. The end-members of groundwater (GW), quick water (SE) and deep soil water (SO) form the vertices of the mixing relationship.

In the second hydrograph (H2), the rising limb samples plot along the first mixing relationship. This would be consistent with some initial dilution as the quick water end-member is activated and silicon concentrations decrease with the rising limb. However, the H2 falling limb samples plot farther away from the first mixing relationship and Ge/Si ratios are higher. Indicating a more significant contribution from deep soil water with higher Ge/Si ratios. Therefore, the component ranking for H2 changes to $C_{GW} > C_{SO} > C_{SE}$ suggesting deep soil water is now the second most important component to stream flow. The second precipitation event was smaller leading to less quick water generation. Additionally, the soil water component is likely deeper in the regolith at a lower K_{sat} were transit times are significantly longer than quick water transit times. In the neighboring Bisley 2 catchments, the K_{sat} in the upper 0.2 m is orders of magnitudes greater than K_{sat} below 0.4 m (Schellekens et al., 2004). The two hydrograph

pulses are only an hour apart. There is a possibility that deeper soil water displaced by infiltrating event water during H1 entered the stream channel soon after the second hydrograph pulse. The lower magnitude precipitation event coupled with significant soil water to the stream may have led to the switching of the hysteresis loop in H2.

Due to the highly weathered regolith at Bisley, we believe that our lysimeter samples did not capture the chemical composition of the third end-member in our mixing diagram. This soil water component is probably located deeper in the regolith profile beyond our deepest lysimeter sample of 9.3 m. Additionally, the higher Ge/Si composition of soil water reflects longer (>7 days) interaction time with secondary minerals in the soil (Kurtz et al., 2011). Our sampling may have been biased towards event water that had infiltrated from a previous precipitation event.

Our results demonstrate that hydrologic flow paths are very similar between the granitic Guaba and the volcaniclastic Bisley catchment despite lithologic differences. This result is in agreement with observations from other sub-catchments in eastern Puerto Rico (Stallard and Murphy, 2014). However, Ge/Si ratios in Bisley are higher than those observed in the Gauba catchment. During the falling limb of H1, we observed ratios as high as 4.85 μmol mol^{-1}. In Guaba, the highest ratio during hydrograph recession was 1.6 μmol mol^{-1} (Kurtz et al., 2011). This may be in relation with the hypothesis that basaltic catchments weather faster than granitic ones (Ibarra et al., 2016 and references therein). Even though contemporary weathering fluxes are almost identical between the Guaba and Bisley catchments, the calculated Si maximum thermodynamic concentration (C_{max}) is twice as high in Bisley than in Guaba (Buss et al., 2017; Wymore et al., 2017). Additionally, Si-Q power law slopes for Bisley 1 show

less dilution than Qubrada Guaba (b = -0.30 to -0.47) (Wymore et al., 2017). Besides differences in weatherability of parent material, geomorphic variables like catchment slope can also account for differences in Si concentrations. Bisley 1 has a steeper slope of 21.9^{o} compared to 17.5^{o} for Guaba (Wymore et al., 2017). This can have important consequences on fluid transit times that lead to highly unsaturated conditions for Si (Maher, 2011). In turn, this may result in higher weathering of secondary clays in the shallow soil where dilute event water is actively transported.

4.6 Conclusion

The activation of hydrologic pathways was explored during a 55 mm storm event in the Bisley 1 catchment of the Luquillo Critical Zone Observatory. Since precipitation fell in two separate events one hour apart, we were able to observe changes in hydrologic components from one stage hydrograph to the next. For the first event, the silicon to stage height pattern developed a clockwise turning hysteresis loop. This pattern suggests a component ranking were groundwater is the dominant end-member to stream flow followed by event water and soil pore water. The Ge/Si to stage height pattern corroborated this interpretation by displaying a counter-clockwise hysteresis loop that indicates the activation of saprolite hydrologic pathway with increasing stream flow. During the second hydrograph pulse, the Si to stage height pattern changed from clockwise to counter-clockwise hysteresis. The ranking for this new pattern suggests continued dominance of groundwater flow but a greater contribution from soil water than event water. The Ge/Si pattern for the second event still had a counter-clockwise hysteresis loop but with higher ratios than the first hydrograph. In 1/Si to Ge/Si mixing

space, we observed that stream water samples can be enclosed by a three end-member system consisting of groundwater, lysimeter samples and a third un-characterized end-member. Stream samples from the first pulse mixed predominantly between groundwater and the lysimeter samples. However, samples from the second pulse mixed between groundwater and a higher Ge/Si pore water end-member. We propose that during the second hydrograph pulse, deeper soil water not sampled in this study was the second most dominant component to stream flow. This pore water most closely resembles the end-member identified as matrix soil water in the Quebrada Guaba catchment of the Rio Icacos (Kurtz et al., 2011). The Bisley 1 catchment experiences less dilution for Si-Q relationships than Quebrada Guaba. We propose that less dilution in Bisley is caused by differences in mineral assemblage and critical zone evolution of volcaniclastic landscapes instead of hydrologic response to precipitation. Further research must focus on characterizing this deeper soil water end-member that has been difficult to sample due to the deep regolith at Bisley. By using soil paste experiments using regolith core, we could also constrain the residence time of infiltrating water to this reservoir. This information will help in understanding interaction time of water with this mineral matrix.

References

Bartoli, F. (1983) The Biogeochemical Cycle of Silicon in 2 Temperate Forest Ecosystems. Ecol Bull, 469-476.

Buss, H.L., Lara, M.C., Moore, O.W., Kurtz, A.C., Schulz, M.S. and White, A.F. (2017)

Lithological influences on contemporary and long-term regolith weathering at the Luquillo Critical Zone Observatory. Geochimica Et Cosmochimica Acta 196, 224-251.

Evans, C. and Davies, T.D. (1998) Causes of concentration/discharge hysteresis and its potential as a tool for analysis of episode hydrochemistry. Water Resources Research 34, 129-137.

Froelich, P.N., Blanc, V., Mortlock, R.A., Chillrud, S.N., Dunstan, W., Udomkit, A. and Peng, T.H. (1992) River fluxes of dissolved silica to the ocean were higher during glacials: Ge/Si in diatoms, rivers, and oceans. Paleoceanography 7, 739-767.

Heumann, K.G. (1988) Isotope Dilution Mass Spectrometry, in: F. Adams, R.G.a.R.V.G. (Ed.), Inorganic Mass Spectrometry. John Wiley & Sons, New York, NY.

Ibarra, D.E., Caves, J.K., Moon, S., Thomas, D.L., Hartmann, J., Chamberlain, C.P. and Maher, K. (2016) Differential weathering of basaltic and granitic catchments from concentration-discharge relationships. Geochimica Et Cosmochimica Acta 190, 265-293.

Kurtz, A.C., Derry, L.A. and Chadwick, O.A. (2002) Germanium-silicon fractionation in the weathering environment. Geochimica Et Cosmochimica Acta 66, 1525-1537.

Kurtz, A.C., Lugolobi, F. and Salvucci, G. (2011) Germanium-silicon as a flow path

tracer: Application to the Rio Icacos watershed. Water Resources Research 47.

Lara, M.C., Buss, H.L., von Strandmann, P., Schuessler, J.A. and Moore, O.W. (2017) The influence of critical zone processes on the Mg isotope budget in a tropical, highly weathered andesitic catchment. Geochimica Et Cosmochimica Acta 202, 77-100.

Lugolobi, F., Kurtz, A.C. and Derry, L.A. (2010) Germanium-silicon fractionation in a tropical, granitic weathering environment. Geochimica Et Cosmochimica Acta 74, 1294-1308.

Ma, J.F., Tamai, K., Yamaji, N., Mitani, N., Konishi, S., Katsuhara, M., Ishiguro, M., Murata, Y. and Yano, M. (2006) A silicon transporter in rice. Nature 440, 688-691.

Maher, K. (2011) The role of fluid residence time and topographic scales in determining chemical fluxes from landscapes. Earth and Planetary Science Letters 312, 48-58.

Mcdowell, W.H., Sanchez, C.G., Asbury, C.E. and Perez, C.R.R. (1990) Influence of Sea Salt Aerosols and Long-Range Transport on Precipitation Chemistry at El-Verde, Puerto-Rico. Atmospheric Environment Part a-General Topics 24, 2813-2821.

Mortlock, R.A. and Froelich, P.N. (1996) Determination of germanium by isotope dilution hydride generation inductively coupled plasma mass spectrometry. Analytica Chimica Acta 332, 277-284.

Murnane, R.J. and Stallard, R.F. (1990) Germanium and Silicon in Rivers of the Orinoco Drainage-Basin. Nature 344, 749-752.

Murphy, S.F. and Stallard, R.F. (2012) Water quality and landscape processes of four watersheds in eatern Puerto Rico.

Pett-Ridge, J.C., Derry, L.A. and Kurtz, A.C. (2009) Sr isotopes as a tracer of weathering processes and dust inputs in a tropical granitoid watershed, Luquillo Mountains, Puerto Rico. Geochimica Et Cosmochimica Acta 73, 25-43.

Prospero, J.M., Glaccum, R.A. and Nees, R.T. (1981) Atmospheric Transport of Soil Dust from Africa to South-America. Nature 289, 570-572.

Scatena, F.N. (1989) An introduction to the physiography and history of the Bisley Experimental Watersheds in the Luquillo Mountains of Puerto Rico. Gen. Tech. Rep. SO-72. New Orleans, LA: US Dept of Agriculture, Forest Service, Southern Forest Experiment Station. 22 p. 72.

Scatena, F.N., Silver, W., Siccama, T., Johnson, A. and Sanchez, M.J. (1993) Biomass and Nutrient Content of the Bisley Experimental Watersheds, Luquillo-Experimental-Forest, Puerto-Rico, before and after Hurricane-Hugo, 1989. Biotropica 25, 15-27.

Schellekens, J., Scatena, F.N., Bruijnzeel, L.A., van Dijk, A., Groen, M.M.A. and van Hogezand, R.J.P. (2004) Stormflow generation in a small rainforest catchment in the luquillo experimental forest, Puerto Rico. Hydrological Processes 18, 505-530.

Shanley, J.B., McDowell, W.H. and Stallard, R.F. (2011) Long-term patterns and short-term dynamics of stream solutes and suspended sediment in a rapidly weathering tropical watershed. Water Resources Research 47.

Sparks, J.P., Chandra, S., Derry, L.A., Parthasarathy, M.V., Daugherty, C.S. and Griffin, R. (2011) Subcellular localization of silicon and germanium in grass root and leaf tissues by SIMS: evidence for differential and active transport. Biogeochemistry 104, 237-249.

Stallard, R.F. (2001) Possible environmental factors underlying amphibian decline in eastern Puerto Rico: Analysis of US government data archives. Conservation Biology 15, 943-953.

Stallard, R.F. and Murphy, S.F. (2014) A Unified Assessment of Hydrologic and Biogeochemical Responses in Research Watersheds in Eastern Puerto Rico Using Runoff-Concentration Relations. Aquatic Geochemistry 20, 115-139.

Torres, M.A., Baronas, J.J., Clark, K.E., Feakins, S.J. and West, A.J. (2017) Mixing as a driver of temporal variations in river hydrochemistry: 1. Insights from conservative

tracers in the Andes-Amazon transition. Water Resources Research 53, 3102-3119.

White, A.F., Blum, A.E., Schulz, M.S., Vivit, D.V., Stonestrom, D.A., Larsen, M., Murphy, S.F. and Eberl, D. (1998) Chemical weathering in a tropical watershed, Luquillo mountains, Puerto Rico: I. Long-term versus short-term weathering fluxes. Geochimica Et Cosmochimica Acta 62, 209-226.

Wymore, A.S., Brereton, R.L., Ibarra, D.E., Maher, K. and McDowell, W.H. (2017) Critical zone structure controls concentration-discharge relationships and solute generation in forested tropical montane watersheds. Water Resources Research 53, 6279-6295.

Ziegler, K., Chadwick, O.A., White, A.F. and Brzezinski, M.A. (2005) (DSi)-Si-30 systematics in a granitic saprolite, Puerto Rico. Geology 33, 817-820.

APPENDIX

Appendix 1: Providence Creek snowmelt chemistry

Snowmelt chemistry from samples collected at lysimeter sites in Providence Creek.

Date	Na (µM)	Mg (µM)	Ca (µM)	K (µM)	Si (µM)	Al (µM)	Sr (µM)	Fe (µM)
2/4/2009	48.4	3.28	11.3	45.0	3.32	1.23	0.03	0.10
4/22/2009	68.2	9.35	22.7	40.2	2.59	1.52	0.06	0.11
5/5/2009	75.6	11.93	26.9	45.5	2.27	1.69	0.00	1.25
12/30/2008	112	9.57	19.0	740	3.64	1.89	0.00	0.39
1/22/2009	21.8	2.44	4.82	18.0	2.27	0.27	0.00	0.18
4/22/2009	52.3	7.13	21.5	41.1	1.12	1.38	0.08	0.10
5/6/2009	45.3	4.91	16.9	80.5	1.88	1.84	0.04	0.17
12/30/2008	80.0	7.28	14.7	49.3	0.71	0.86	0.04	0.16

Appendix 2: KREW silicon flux

Silicon flux for the Kings Experimental Watershed during WY2009.

	Snowmelt ($\mu mol\ m^{-2}$)	**Total ($\mu mol\ m^{-2}$)**	**Snowmelt Flux (%)**
Sub-catchment			
P301	37,406	81,017	46.2
P303	24,923	41,779	59.7
P304	32,280	99,463	32.5
D102	37,919	79,814	47.5
B201	11,145	37,196	30.0
B203	11,148	32,149	34.7
B204	15,483	47,295	32.7
T003	37,919	190,546	21.2

Appendix 3: Providence Creek stream mineral saturation indices

Date	catchment	Albite log Q/K	Amrph^silica log Q/K	Anorthite log Q/K	Gibbsite log Q/K	Illite log Q/K	K-feldspar log Q/K	Kaolinite log Q/K	Muscovite log Q/K	Quartz log Q/K
11/4/2008	P301	-1.4	-0.7	-6.3	0.9	2.2	0.8	3.4	4.0	0.6
11/26/2008	P301	-1.5	-0.7	-6.6	0.7	1.9	0.6	3.1	3.5	0.6
1/27/2009	P301	-1.5	-0.8	-6.4	0.9	2.1	0.6	3.4	3.9	0.5
2/23/2009	P301	-1.7	-0.8	-6.5	1.0	1.9	0.4	3.3	3.7	0.4
3/30/2009	P301	-1.9	-0.8	-6.8	0.8	1.5	0.3	2.9	3.3	0.5
4/28/2009	P301	-1.6	-0.8	-6.4	1.0	2.1	0.5	3.5	3.9	0.5
5/12/2009	P301	-1.7	-0.8	-6.6	0.9	1.8	0.4	3.2	3.6	0.5
6/29/2009	P301	-1.0	-0.7	-5.8	1.0	2.8	1.1	3.8	4.6	0.6
7/28/2009	P301	-1.1	-0.6	-6.2	0.8	2.4	0.9	3.4	4.0	0.6
8/25/2009	P301	-1.4	-0.7	-6.7	0.6	1.8	0.7	2.9	3.3	0.6
11/4/2008	P303	-1.5	-0.6	-7.0	0.3	1.4	0.6	2.4	2.6	0.7
11/26/2008	P303	-1.4	-0.6	-6.9	0.4	1.6	0.7	2.6	2.9	0.7
1/27/2009	P303	-1.4	-0.7	-6.8	0.6	1.8	0.6	2.9	3.3	0.6
2/24/2009	P303	-1.5	-0.8	-6.4	0.9	2.1	0.6	3.3	3.8	0.5
3/30/2009	P303	-1.8	-0.8	-6.9	0.7	1.5	0.3	2.8	3.0	0.5
6/29/2009	P303	-1.9	-0.7	-7.5	0.2	0.8	0.2	2.0	2.0	0.6
7/28/2009	P303	-1.1	-0.5	-6.6	0.4	2.0	1.1	2.9	3.4	0.7
8/25/2009	P303	-1.6	-0.6	-7.1	0.2	1.3	0.6	2.3	2.5	0.7
11/4/2008	P304	-1.0	-0.6	-5.7	0.9	2.8	1.3	3.6	4.6	0.6
11/26/2008	P304	-1.4	-0.7	-6.5	0.6	2.0	0.8	3.0	3.5	0.6
12/10/2008	P304	-1.1	-0.6	-6.1	0.7	2.3	1.0	3.2	3.9	0.7
1/27/2009	P304	-1.4	-0.7	-6.5	0.7	1.9	0.7	3.0	3.5	0.6
2/24/2009	P304	-1.4	-0.7	-6.4	0.7	2.0	0.7	3.1	3.6	0.6
3/30/2009	P304	-1.6	-0.7	-6.8	0.5	1.6	0.5	2.7	3.0	0.6
5/12/2009	P304	-1.2	-0.6	-6.4	0.6	2.2	1.0	3.1	3.6	0.7
6/29/2009	P304	-0.4	-0.7	-4.7	1.5	3.9	1.5	4.7	5.9	0.6
7/28/2009	P304	-1.1	-0.6	-6.1	0.8	2.3	0.9	3.3	3.9	0.6
8/25/2009	P304	-1.1	-0.6	-6.3	0.7	2.3	1.1	3.2	3.9	0.7
11/4/2008	D102	-0.7	-0.6	-5.6	1.0	3.1	1.5	3.9	4.9	0.7
11/26/2008	D102	-1.4	-0.6	-6.8	0.4	1.7	0.9	2.7	3.2	0.7
12/10/2008	D102	-1.5	-0.6	-7.2	0.2	1.3	0.6	2.3	2.5	0.7
1/27/2009	D102	0.0	-0.4	-4.9	1.3	4.2	2.0	4.8	6.1	0.8
2/24/2009	D102	-1.4	-0.8	-6.3	1.0	2.2	0.7	3.4	4.1	0.5
3/28/2009	D102	-1.3	-0.7	-6.5	0.7	2.1	0.8	3.2	3.7	0.6
4/28/2009	D102	-1.2	-0.6	-6.2	0.8	2.4	1.0	3.4	4.0	0.6
5/12/2009	D102	-1.2	-0.7	-6.4	0.7	2.1	0.9	3.2	3.7	0.6
6/29/2009	D102	-1.6	-0.6	-7.4	0.2	1.0	0.4	2.2	2.3	0.6
7/28/2009	D102	-0.9	-0.6	-6.3	0.7	2.3	1.1	3.2	3.9	0.7
8/25/2009	D102	-1.1	-0.6	-6.5	0.5	2.1	1.0	3.0	3.5	0.7

Appendix 4: **Bull Creek stream mineral saturation indices.**

Date	Catchment	Albite log Q/K	Amrph^silica log Q/K	Anorthite log Q/K	Gibbsite log Q/K	Illite log Q/K	K-feldspar log Q/K	Kaolinite log Q/K	Muscovite log Q/K	Quartz log Q/K
11/4/08	B201	-2.2	-1.0	-6.9	1.0	1.6	0.2	3.1	3.7	0.3
11/26/08	B201	-2.7	-1.1	-7.6	0.8	0.6	-0.4	2.4	2.5	0.2
12/9/08	B201	-2.8	-1.0	-7.9	0.5	0.1	-0.7	2.0	1.7	0.3
3/31/09	B201	-3.8	-1.3	-8.7	0.5	-1.1	-1.8	1.4	0.7	0.0
4/28/09	B201	-3.8	-1.5	-8.3	0.9	-0.7	-1.9	1.9	1.4	-0.2
7/28/09	B201	-2.7	-0.9	-7.6	0.5	0.3	-0.8	2.2	1.7	0.4
8/25/09	B201	-1.8	-0.8	-6.7	0.8	1.6	0.1	3.1	3.2	0.5
11/5/08	B203	-3.8	-1.3	-8.8	0.5	-0.9	-1.5	1.4	0.9	0.0
11/26/08	B203	-3.4	-1.2	-8.6	0.5	-0.5	-1.3	1.7	1.2	0.1
12/9/08	B203	-3.4	-1.1	-9.0	0.2	-1.0	-1.5	1.3	0.4	0.2
2/25/09	B203	-4.5	-1.5	-9.4	0.4	-1.7	-2.3	1.0	0.1	-0.2
3/31/09	B203	-4.6	-1.5	-9.4	0.5	-1.8	-2.5	1.1	0.0	-0.2
6/29/09	B203	-3.6	-1.2	-8.5	0.6	-0.7	-1.6	1.8	1.0	0.1
8/25/09	B203	-3.8	-1.2	-9.3	0.1	-1.6	-1.9	0.9	-0.3	0.1
8/25/09	B204	-2.9	-1.0	-7.9	0.6	0.2	-0.7	2.2	1.8	0.3
11/5/08	B204	-2.7	-1.0	-7.6	0.7	0.6	-0.4	2.4	2.4	0.2
11/26/08	B204	-3.0	-1.0	-8.4	0.4	-0.4	-1.0	1.7	1.2	0.2
2/25/09	B204	-3.4	-1.1	-8.8	0.2	-0.9	-1.4	1.3	0.5	0.2
3/31/09	B204	-3.8	-1.3	-8.9	0.3	-1.3	-1.8	1.2	0.3	0.0
6/29/09	B204	-3.1	-1.1	-8.0	0.6	0.0	-1.1	2.2	1.6	0.2
1/28/09	T003	-2.2	-1.0	-6.9	0.9	1.2	-0.1	2.9	3.1	0.3
11/5/08	T003	-2.0	-0.9	-6.7	0.9	1.6	0.3	3.0	3.5	0.4
11/26/08	T003	-2.2	-0.9	-7.2	0.7	1.0	-0.1	2.6	2.7	0.4
12/9/08	T003	-2.3	-0.8	-7.4	0.4	0.8	-0.1	2.3	2.3	0.5
2/24/09	T003	-2.8	-1.1	-7.4	0.8	0.7	-0.5	2.5	2.6	0.2
3/30/09	T003	-2.6	-1.0	-7.5	0.6	0.5	-0.5	2.3	2.2	0.3
5/7/09	T003	-2.7	-1.1	-7.4	0.9	0.6	-0.7	2.6	2.5	0.2
8/25/09	T003	-2.2	-0.9	-7.2	0.7	1.0	-0.2	2.6	2.6	0.4

Appendix 5: KREW soil pore water mineral saturation indices.

Date mm/dd/yyyy	Sub-catchment	Albite log Q/K	Amrph^silica log Q/K	Anorthite log Q/K	Gibbsite log Q/K	Illite log Q/K	K-feldspar log Q/K	Kaolinite log Q/K	Muscovite log Q/K	Quartz log Q/K
3/24/2009	P303	-3.8	-1.6	-6.5	1.7	1.3	-0.4	3.2	4.4	-0.3
3/24/2009	P303	-4.1	-1.8	-6.2	1.9	1.6	-0.3	3.3	5	-0.5
3/25/2009	P301	-	-	-	-	-	-	-	-	-
4/21/2009	P301	-	-	-	-	-	-	-	-	-
5/5/2009	P303	-3.3	-1.5	-5.7	2	2.5	0.2	4	5.6	-0.2
2/3/2009	P301	-	-	-	-	-	-	-	-	-
3/25/2018	P301	-3.4	-1.5	-5.6	1.9	2.6	0.6	3.9	6	-0.2
3/24/2009	P304	-	-	-	-	-	-	-	-	-
4/21/2009	P301	-	-	-	-	-	-	-	-	-
3/24/2009	D102	-3.8	-1.5	-6.9	1.4	0.9	-0.5	2.7	3.7	-0.3
5/5/2009	D102	-3.4	-1.4	-6.5	1.5	1.6	0	3.2	4.4	-0.1
4/22/2009	P304	-3.6	-1.6	-6.5	1.8	1.5	-0.6	3.5	4.5	-0.3
4/22/2009	D102	-3.6	-1.5	-6.6	1.5	1.4	-0.2	3.1	4.2	-0.2
2/3/2009	P303	-4	-1.5	-7.3	1.2	0.4	-0.9	2.4	2.9	-0.2
2/3/2009	P304	-4.3	-1.7	-7.6	1.3	-0.2	-1.6	2.3	2.5	-0.4
2/4/2009	D102	-4	-1.7	-6.4	1.7	1.2	-0.6	3.1	4.3	-0.4
5/5/2009	D102	-3.8	-1.8	-6.1	2.1	1.6	-0.7	3.7	5	-0.5
2/3/2009	P303	-3.9	-1.4	-6.8	1.4	1.2	-0.3	3	3.9	-0.1
5/5/2009	P304	-4.1	-1.5	-8.1	0.9	-0.5	-1.5	1.9	1.7	-0.2
1/21/2009	P301	-3.1	-1.4	-6.1	1.5	2.3	0.7	3.5	5.3	-0.1
1/21/2009	D102	-3.8	-1.6	-6.6	1.5	1.1	-0.5	3	4	-0.3
1/21/2009	P303	-3.5	-1.4	-6.7	1.4	1.4	-0.2	3.1	4.1	-0.2
4/22/2009	P303	-4.1	-1.6	-7.2	1.3	0.5	-0.9	2.6	3.1	-0.3
5/5/2009	P303	-4.2	-1.5	-7.6	1.1	0.1	-1	2.2	2.6	-0.2
1/21/2009	P303	-4	-1.5	-7.5	1	0.2	-0.9	2.2	2.6	-0.2
1/21/2009	P304	-3.4	-1.5	-6.7	1.6	1.4	-0.5	3.2	4.1	-0.2

Appendix 6: Gordon Gulch mineral separates XRD patterns

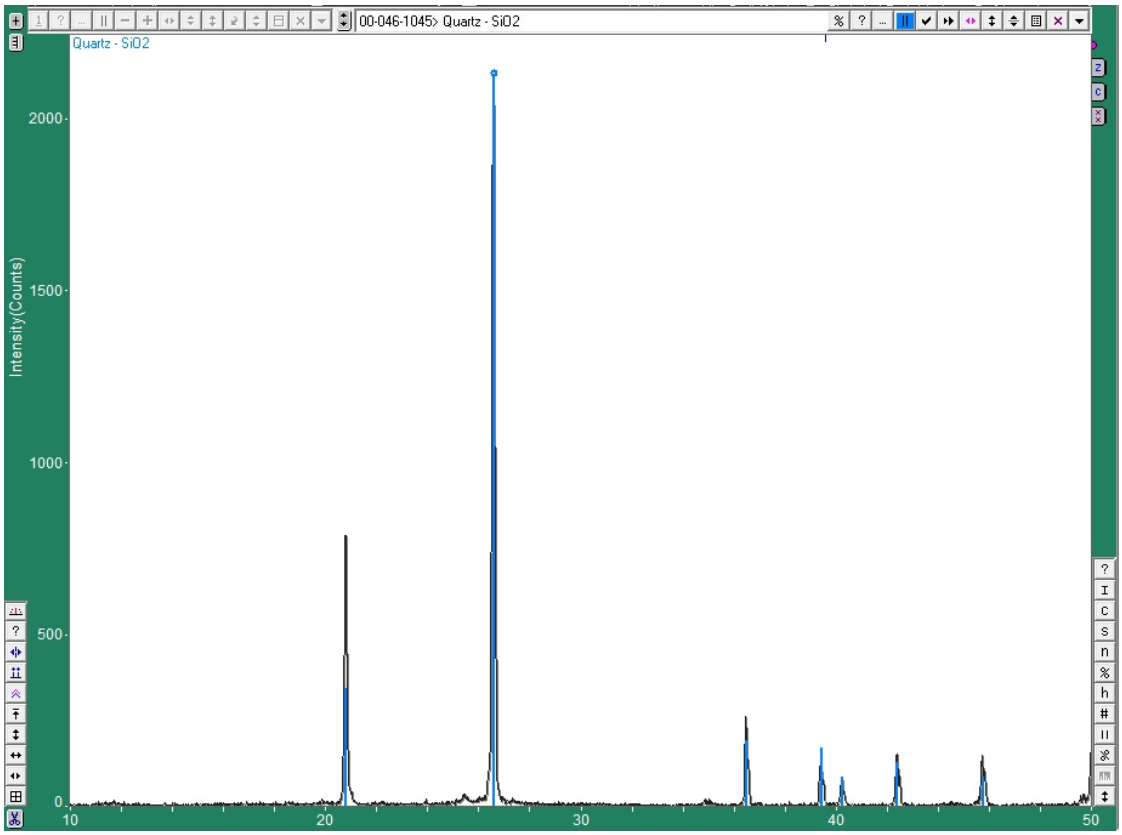

A5.1: Powder diffraction scan of quartz from upper Gordon Gulch. The pattern demonstrates almost pure quartz without inclusions from other minerals. Intensity of signal is in the y-axis and 2Θ angle is in the x-axis.

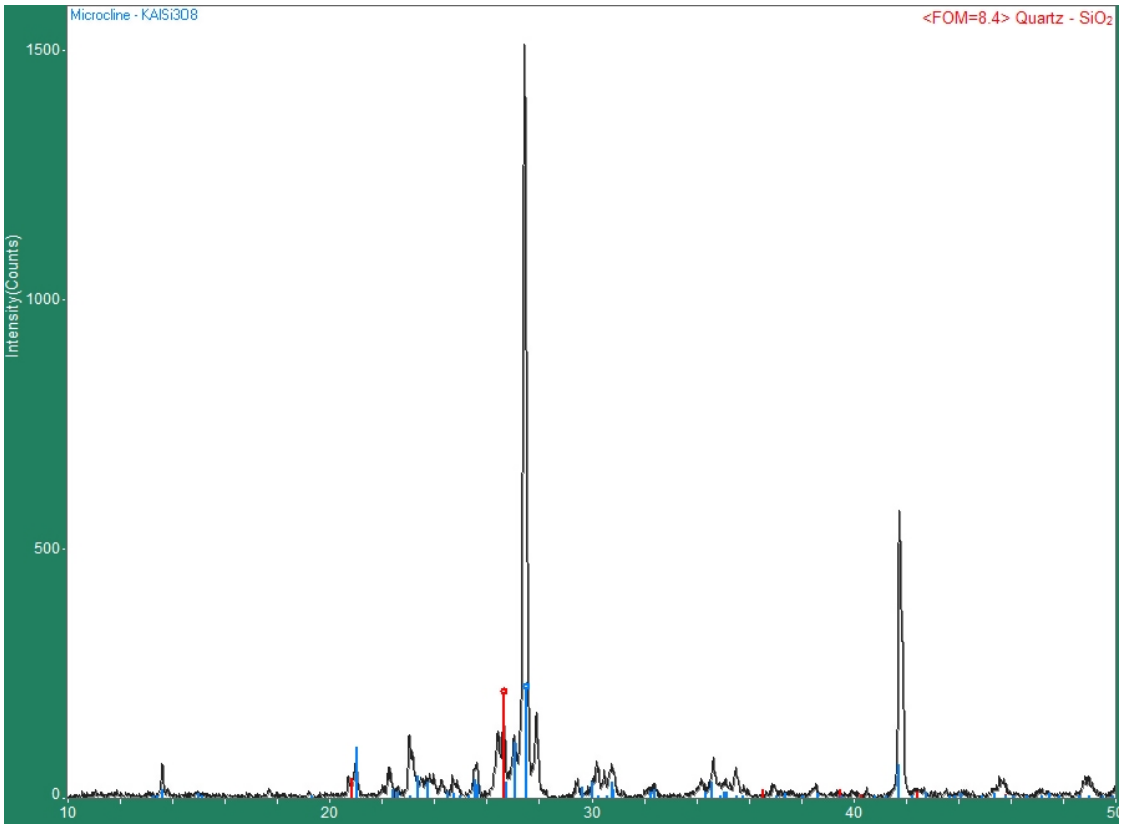

A 5.2: XRD pattern of feldspar in upper Gordon Gulch. The crystal structure of the sample was identified as microcline. Bulk chemistry demonstrated elevated concentrations of K_2O, reinforcing the identification of an alkali feldspar. The pattern has an unresolved peak at 28º that may correspond to an inclusion of plagioclase. The quartz inclusions in this sample are evident with the presence of the 26º peak. Intensity of signal is in the y-axis and 2Θ angle is in the x-axis.

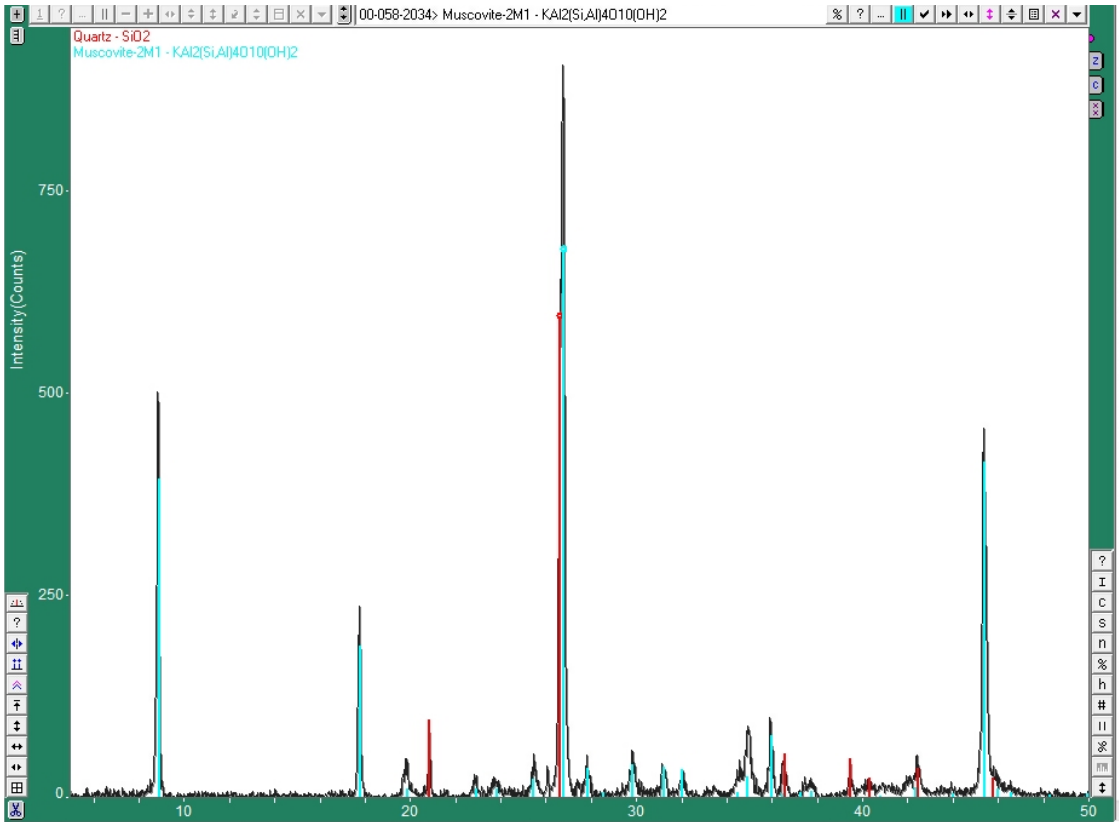

A 5.3: XRD pattern of muscovite with some quartz inclusions. Intensity of signal is in the y-axis and 2Θ angle is in the x-axis.

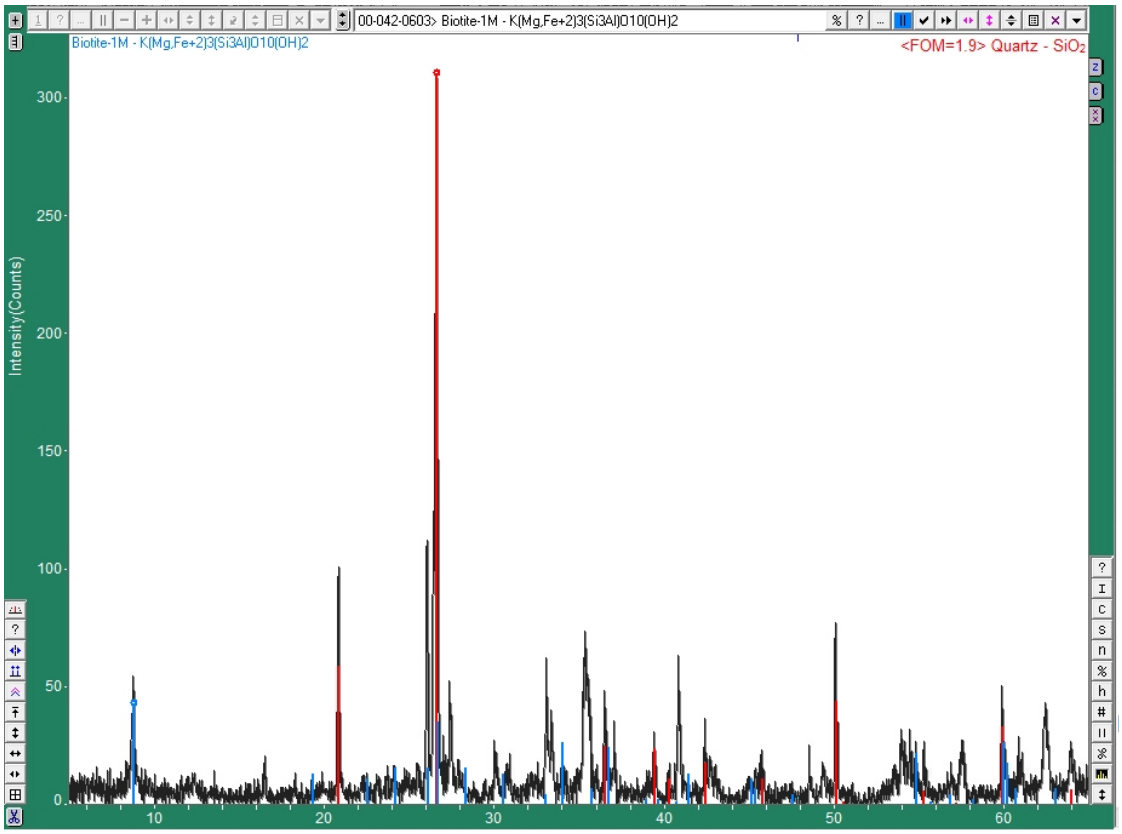

A 5.4: The powder diffraction scan of the sample matches with the major peaks of biotite and quartz. There are some unresolved minor peaks that may be a result of inclusions from other minerals. Intensity of signal is in the y-axis and 2Θ angle is in the x-axis.

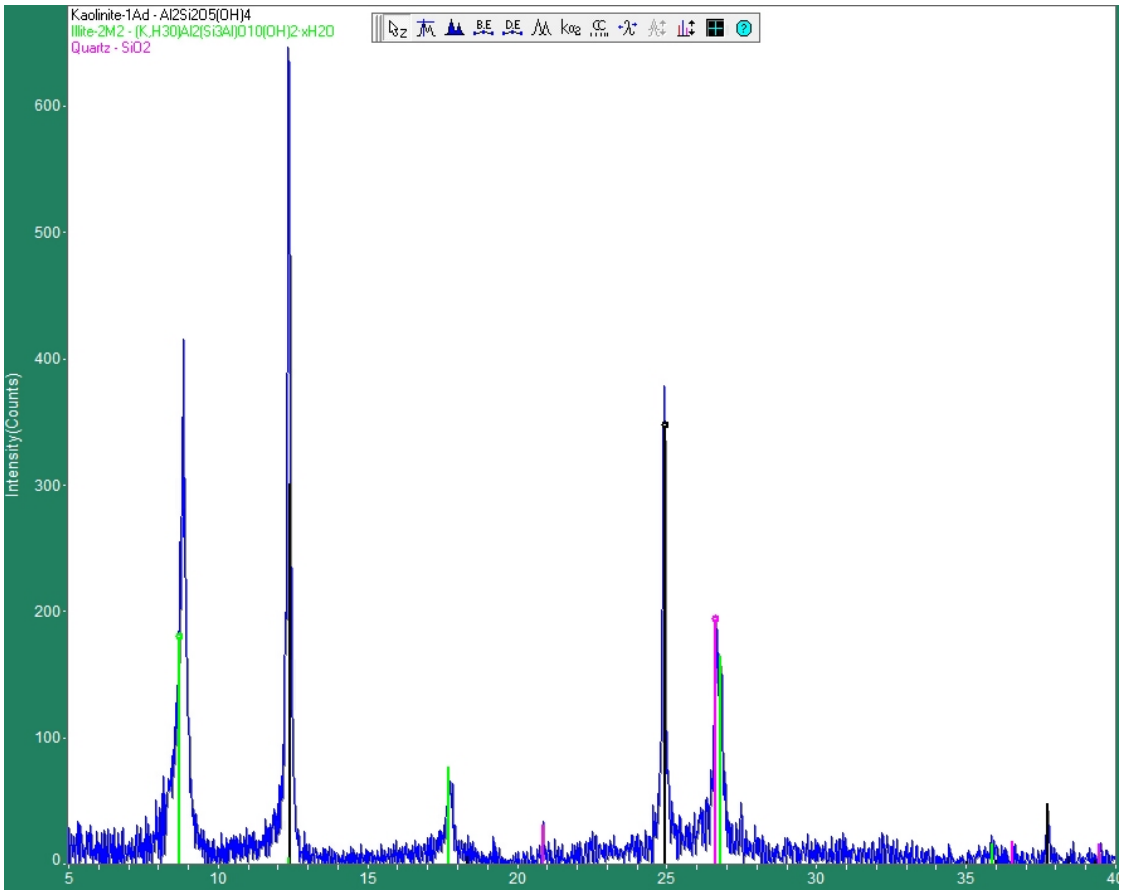

A 5.5: XRD pattern of clay from 0.6-0.9 m in upper Gordon Gulch. The major peaks of kaolinite and illite are prominent in the scan. In between the angle 26º and 27º, a split in the peaks can be observed. This may correspond to overlap of illite and quartz peaks. Ethylene glycol solvation demonstrated the absence of expandable clays. Intensity of signal is in the y-axis and 2Θ angle is in the x-axis.

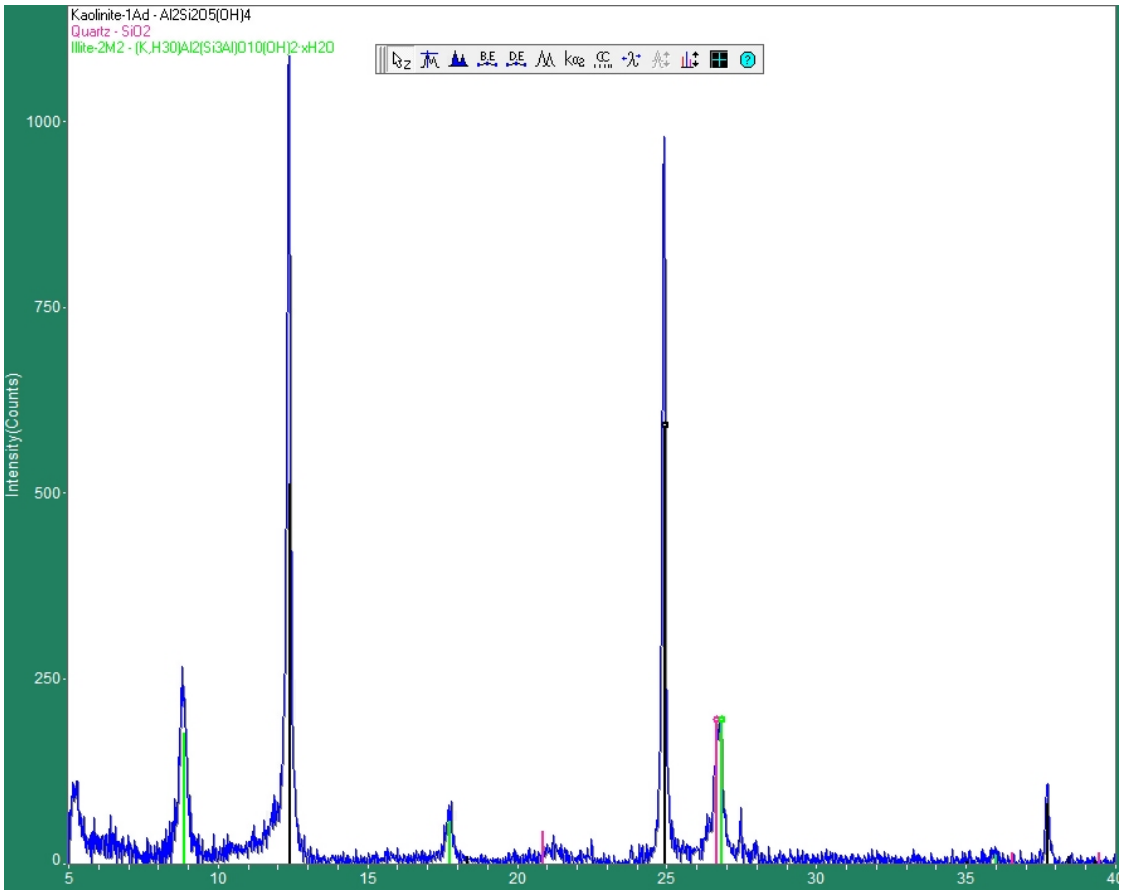

A 5.6: XRD pattern of clay from 1.8-2.1 m in upper Gordon Gulch. The major peaks of kaolinite and illite are very sharp in the scan and there is low noise in the pattern. In between the angle 26º and 27º, a split in the peaks can be observed. This may correspond to overlap of illite and quartz peaks. Ethylene glycol solvation demonstrated the absence of expandable clays. Peaks between 27o and 28º may correspond to inclusions of plagioclase. Intensity of signal is in the y-axis and 2Θ angle is in the x-axis.

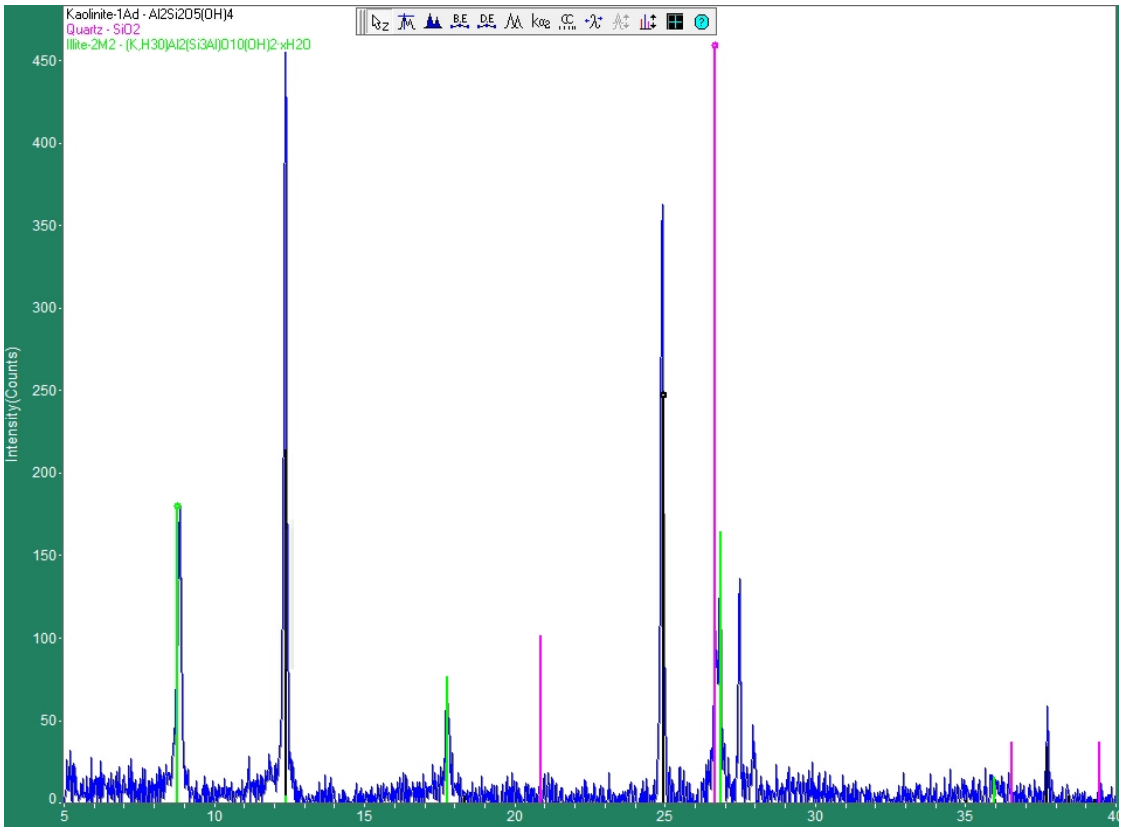

A 5.7: XRD pattern of clay from 2.4-2.7 m in upper Gordon Gulch. The major mineral phases identified are kaolinite, illite and quartz. The split in signal corresponding to illite and quartz peaks between the angle 26º and 27º can be observed. Ethylene glycol solvation demonstrated the absence of expandable clays. The peaks between 27º and 28º corresponding to plagioclase are more pronounced in this scan. Intensity of signal is in the y-axis and 2Θ angle is in the x-axis.

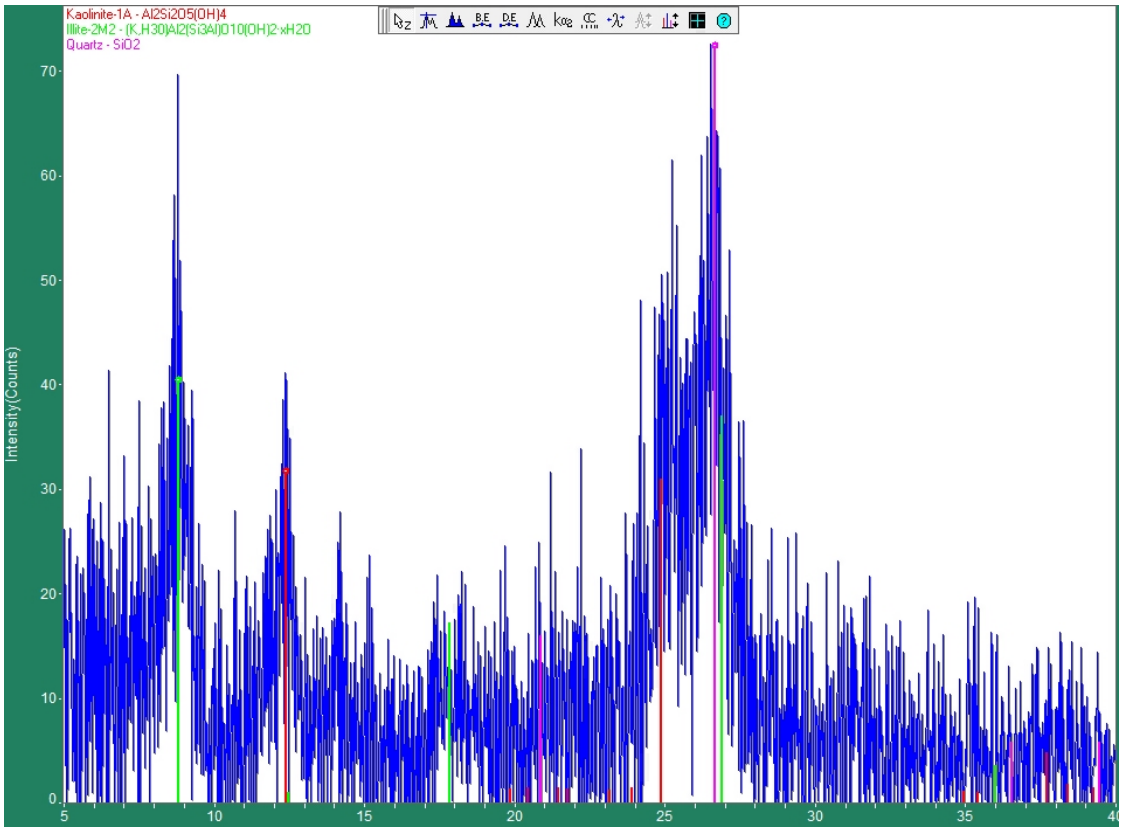

5.8: XRD scan of soil colloids. Prominent kaolinite and illite peaks can be observed at 12.5º and 9º respectively. The quartz peak at 26.6º overlaps the illite peak that follows it. The pattern is noisier than in the clay separations due to limited sample mass. A few drops of the soil colloid suspension were air dried on a petrographic glass slide. Ethylene glycol solvation did not show the presence of expandable clays. Intensity of signal is in the y-axis and 2Θ angle is in the x-axis.

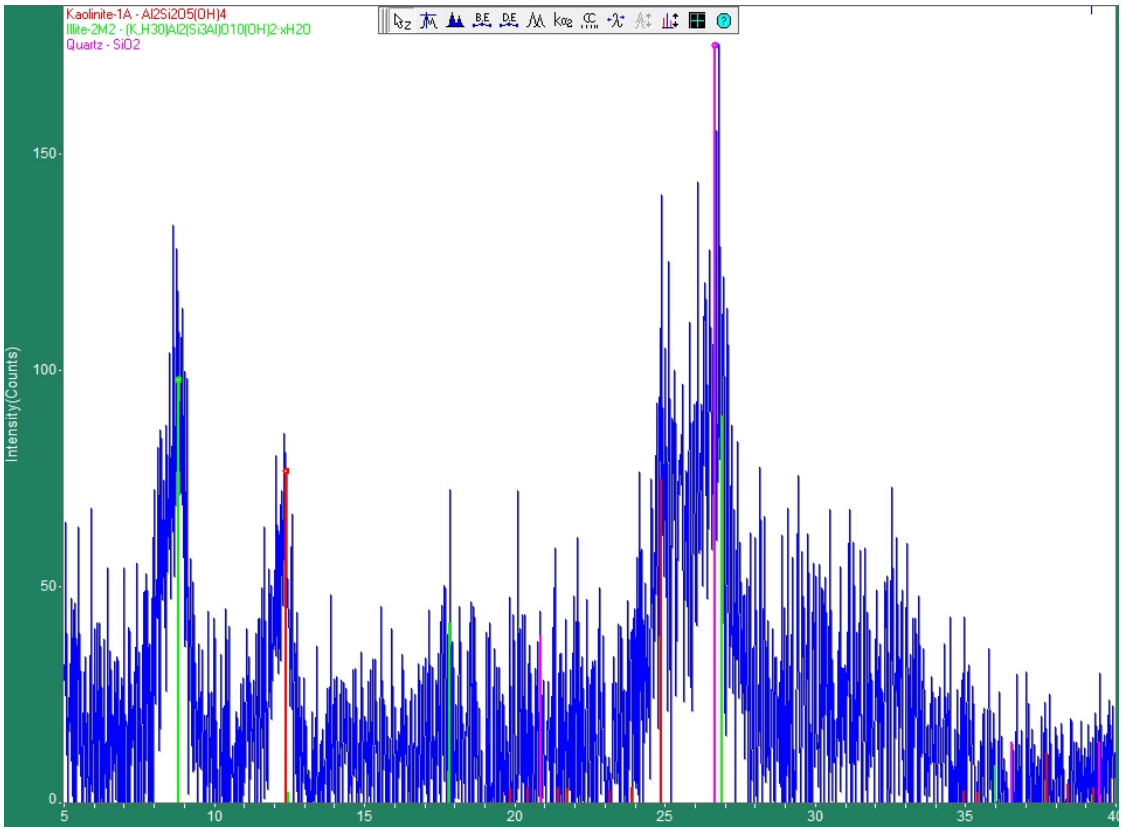

A 5.9: XRD scan of stream colloids. Prominent kaolinite and illite peaks can be observed at 12.5º and 9º respectively. The quartz peak at 26.6º overlaps the illite peak that follows it. Sample preparation for stream colloids is the same as the clays and soil colloids. Ethylene glycol solvation did not show the presence of expandable clays. Intensity of signal is in the y-axis and 2Θ angle is in the x-axis.

Appendix 7: Gordon Gulch groundwater saturation indices.

Table S1

Saturation indices[1] (Ω) of groundwater samples in Gordon Gulch

	Groundwater		
	North facing	*South facing*	*Riparian*
kaolinite	1.02	2.18	1.67
k-feldspar	-0.80	-0.07	-0.30
albite	-3.22	-2.23	-2.33
anorthite	-8.35	-6.75	-7.39

[1]the LLNL thermodynamic database was sued to compute Ω

Filename: AAguirre_Dissertation_Revised_Jul_19.docx
Directory: /Users/arnulfoaguirre/Library/Containers/com.microsoft.Word/Data/Documents
Template: /Users/arnulfoaguirre/Library/Group Containers/UBF8T346G9.Office/User Content.localized/Templates.localized/Normal.dotm
Title: REPLACE THIS WITH THE ACTUAL TITLE USING ALL CAPS
Subject:
Author: jst35
Keywords:
Comments:
Creation Date: 7/19/19 3:25:00 PM
Change Number: 2
Last Saved On: 7/19/19 3:25:00 PM
Last Saved By: Arnulfo Andres Aguirre
Total Editing Time: 0 Minutes
Last Printed On: 7/19/19 3:25:00 PM
As of Last Complete Printing
Number of Pages: 209
Number of Words: 44,229 (approx.)
Number of Characters: 230,435 (approx.)